[American Journal of Science, Vol. 318, June, 2018, P. 640–683, DOI 10.2475/06.2018.02]

PETROGENESIS OF THE RAMBLER RHYOLITE FORMATION: CONTROLS ON THE MING VMS DEPOSIT AND GEODYNAMIC IMPLICATIONS FOR THE TACONIC SEAWAY, NEWFOUNDLAND APPALACHIANS, CANADA

JEAN-LUC PILOTE*,**,† and STEPHEN J. PIERCEY*

ABSTRACT. **The Ming Cu-Zn-Ag-Au volcanogenic massive sulfide (VMS) deposit is hosted by the Upper Cambrian-Lower Ordovician Rambler Rhyolite formation, which consists of a folded northeast plunging felsic dome complex, developed in the uppermost segment of the obducted supra-subduction Baie Verte oceanic tract, in the north central Newfoundland Appalachians. The deposit is overlain by interstratified mafic volcanic flows and volcaniclastic rocks of the Snooks Arm Group. The upper 1 km of the Rambler Rhyolite formation consists of a coherent felsic lithofacies at its base, overlain by a quartz-bearing volcaniclastic-dominated lithofacies (units 1.2 and 1.3). Geochemically, these rocks are light rare earth element (LREE)- and large ion lithophile element (LILE)-enriched ($[La/Yb]_{pn}$ = 4–20; Th = 2.58–4.05 ppm), and high field strength element (HFSE)-depleted (Y = 5.64–6.59 ppm) rhyodacite with calk-alkalic affinities (Th/Yb > 2; Zr/Y > 7). The last pulse of felsic volcanism (unit 1.3) is intimately associated with the massive sulfide lenses and has FI- and FII-type rhyolite signatures (high La/Yb ratios), commonly attributed to deep (≥ 30 km) crustal melting. The $\varepsilon Nd_{(t)}$ values of the rhyolites range from −2.5 to −1.3, indicating the rocks were influenced by crustal material. A 10 percent batch partial melt of a garnet-amphibole metamorphosed normal mid-oceanic ridge basalt (N-MORB) and island arc tholeiite (IAT) crustal material can generate a melt similar to the felsic rocks hosting the Ming deposit; however, the IAT reproduces much better the absolute abundances of LILE (Th, Sr), HFSE (Nb, Zr, Y), and middle rare earth elements (MREE) of the felsic rocks. It is interpreted that the felsic melt came from melting of a subducted slab with IAT affinity, thus explaining the depth of melt generation and FI-FII signatures of the felsic rocks. Moreover, the slab-derived siliceous melt may also have contributed magmatophile elements (for example, Ag, Au, Se, Te, Sn, Sb, Hg) into the hydrothermal system once it had reached near-surface depths, and may explain the epithermal suite element-enrichment in the Ming deposit. This study shows that strongly fractionated felsic volcanic rocks associated with boninites, such as those associated with the Ming VMS deposit, can be important hosts for precious metal-enriched VMS and may be as prospective as tholeiitic felsic volcanic sequences (for example, FIII-FIV-type rhyolite – low La/Yb ratios).**

The base of the Snooks Arm Group is comprised of spatially restricted sulfide-bearing mafic breccia, overlain by a regionally extensive sedimentary sequence ($\varepsilon Nd_{(t)}$ = +3.1 to +5.5), which is in turn overlain by interstratified high-Mg basalt ($\varepsilon Nd_{(t)}$ = +1.6), Th-enriched back-arc basin basalt (BABB), enriched mid-oceanic ridge basalt (E-MORB; $\varepsilon Nd_{(t)}$ = +6.6), and LREE-enriched/low-Ti tholeiitic tuffs ($\varepsilon Nd_{(t)}$ = −0.5). Four generations of mafic to intermediate dikes and sills cross-cut the Rambler Rhyolite formation and share similar geochemical characteristics to the extrusive rocks of the Snooks Arm Group, suggesting comagmatic relationships. The combination of variations in Nb/Yb, Th /Yb, and $\varepsilon Nd_{(t)}$ values within and between units suggest melts derived from depleted to enriched mantle material with melts synchronously generated by both slab-metasomatized mantle wedge and upwelling back-arc asthenosphere.

* Department of Earth Sciences, Memorial University of Newfoundland, 300 Prince Philip Drive, St. John's, Newfoundland and Labrador A1B 3X5, Canada

** Present address: Geological Survey of Canada, 490 rue de la Couronne, Québec, Québec G1K 9A9, Canada

† Corresponding author: jean-luc.pilote@canada.ca

Key words: petrogenesis, Taconic seaway, volcanogenic massive sulfide, FI-type felsic volcanic rocks, Appalachians

INTRODUCTION

The Newfoundland Appalachians host ~45 producing, past producing, and prospective VMS deposits formed during the complex Early Paleozoic evolution of the Iapetus oceanic realm and its subsidiary seaways (Piercey, 2007; van Staal, 2007; Hinchey, 2011). The Ming VMS deposit (combined with the historical Ming West deposit and hereafter referred to as simply the Ming deposit) lies within the obducted Cambro-Ordovician oceanic crustal rocks of the Baie Verte oceanic tract, which is host to six other formerly producing or sub-economic VMS deposits of similar age, including the Rambler, East Rambler, Big Rambler Pond, Terra Nova, Betts Cove, and Tilt Cove deposits (fig. 1). Between 1971 and 1982, the Ming deposit produced over 2.1 Mt at 3.5 percent Cu, 11 g/t Ag, and 2.5 g/t Au (Rambler Metals and Mining Ltd.). Since re-opening in 2012, a total of 809,508 tonnes grading 2.9 percent Cu, 9.63 g/t Ag, and 1.38 g/t Au were commercially produced with combined measured and indicated resources of almost 28 Mt, averaging 1.48 percent Cu, 0.06 percent Zn, 1.99 g/t Ag, and 0.26 g/t Au (as of November 2016, Rambler Metals and Mining Ltd.). The Ming, East Rambler, and Rambler deposits are hosted in the same dome-shaped felsic complex (Rambler Rhyolite formation) that is constructed upon successions of boninitic and island arc tholeiitic rocks (Betts Head and Mount Misery formations, respectively), also host to Cyprus-type VMS mineralization to the south and east of the peninsula (fig. 2; Sangster and others, 2007). These deposits, including the Ming deposit, are stratigraphically overlain by successions of tholeiitic to calc-alkalic mafic to felsic volcanic and volcaniclastic rocks, which collectively forms the ophiolitic cover sequence (Snooks Arm Group; Skulski and others, 2010). In recent years, a number of studies on the Ming deposit have led to the advancement of our understanding on its genesis, including detailed micro-analytical work on the massive and semi-massive sulfide lenses (Brueckner and others, 2011, 2014, 2015, 2016) and the timing of Au-introduction (Pilote and others, 2016), and a number of preliminary reports on the volcanic architecture, stratigraphy, structure, and alteration of the deposit (Pilote and Piercey, 2013; Pilote and others, 2014, 2017). The primary geochemical nature and petrogenesis of the felsic rocks and their relationships within their stratigraphic framework and to mineralization, however, have yet to receive any attention.

The composition of host felsic rocks can have direct controls on the metal budget of VMS deposits, either from direct magmatic degassing (Lydon, 1996; Yang and Scott, 1996; Solomon and Zaw, 1997) and/or hydrothermal leaching of the felsic footwall rocks (Franklin and others, 1981; Lydon, 1988). Not only can a link between the composition of the felsic rocks and associated mineralization be made, tectonic environments they have formed in are interpreted to be a primary controlling factor on magma compositions (Wilson, 1989). Here, an attempt to determine the source of the felsic rocks is made through lithogeochemical modeling of their initial compositions, and additional utilization of immobile compatible (for example, TiO_2, Al_2O_3) and incompatible (for example, Zr, REE) elements to characterize their magmatic and tectonic affinities (for example, Cabanis and Lecolle, 1989; Ross and Bédard, 2009). The base of the overlying Snooks Arm Group is also examined and geochemically characterized in order to reconstruct the magmatic evolution that post-dates the time of formation of the Rambler Rhyolite formation.

The felsic successions that are intimately associated with the Ming massive sulfide lenses are Al-rich and have highly fractionated HREE signatures typical of FI-type rhyolites, which are conventionally considered infertile for hosting VMS mineralization (Lesher and others, 1986; Hart and others, 2004). Hence, the rare association between FI-type felsic rocks and VMS deposits worldwide make the footwall rocks of the

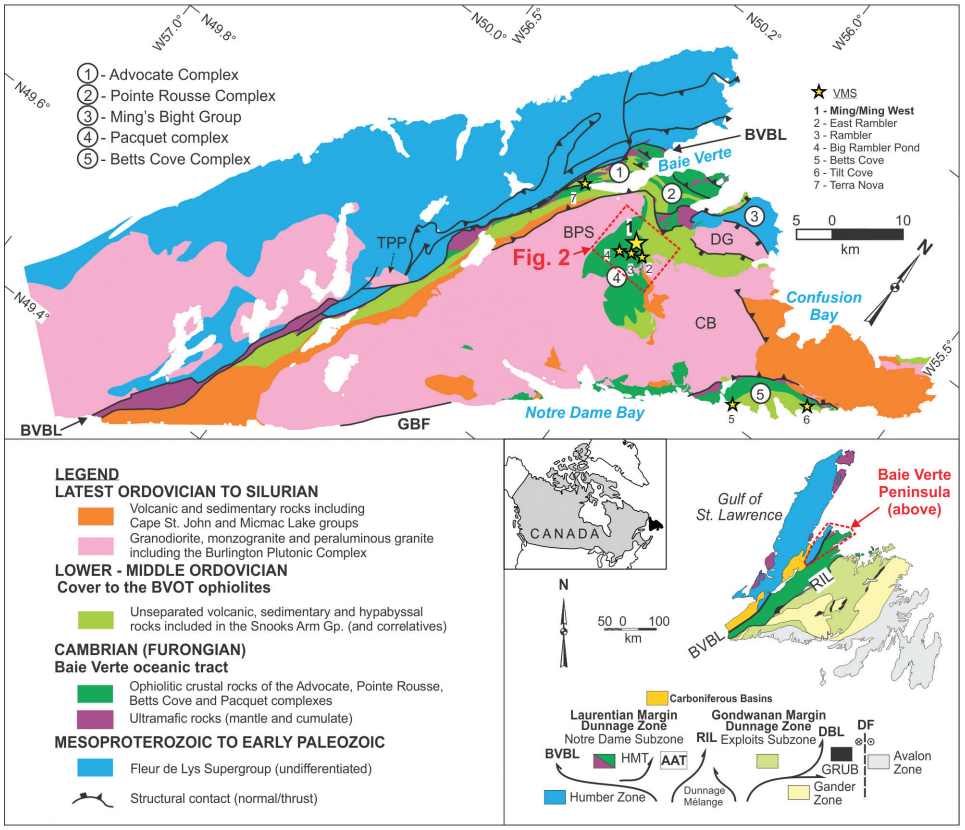

Fig. 1. Simplified geology of the Baie Verte Peninsula with major tectonostratigraphic zones that form the Appalachian orogenic belt in Newfoundland (modified from Castonguay and others, 2014 and references therein). Location of major VMS deposits as yellow stars. AAT = Annieopsquotch Accretionary Tract, BPS = Burlington plutonic Suite, BVBL = Baie Verte-Brompton Line, BVBL = Baie Verte-Brompton Line, CB = Cape Brulé, DBL = Dog Bay Line, DF = Dover Fault, DG = Dunamagon Granite, GBF = Green Bay Fault, GRUB = Gander River Ultramafic Belt, TPP = Trap Pond pluton, RIL = Red Indian Line, HMT = Hungry Mountain Thrust.

Ming deposit an important case study to determine the controlling factors on their genesis, their relationship to mineralization, and how this could impact target generation in other VMS districts, globally. Whereas reconciling the complex tectonic history of the Baie Verte oceanic tract is beyond the scope of this study (for example, Dewey and Casey, 2015 and references therein), the results presented here will also help refine our current understanding of the Cambrian-Ordovician magmatic and tectonic evolution of the peri-Laurentian seaway during the metallogenic evolution of the Appalachians.

GEOLOGIC SETTING

The Baie Verte Oceanic Tract and Adjacent Terranes

The Upper Cambrian to Lower Ordovician (489–477 Ma) Baie Verte oceanic tract (BVOT) forms one of the peri-Laurentian tectonic elements assembled during the Cambrian evolution of the Taconic seaway, which developed following the Ediacaran rifting of Dashwoods block from the eastern Laurentia (Waldron and van Staal, 2001;

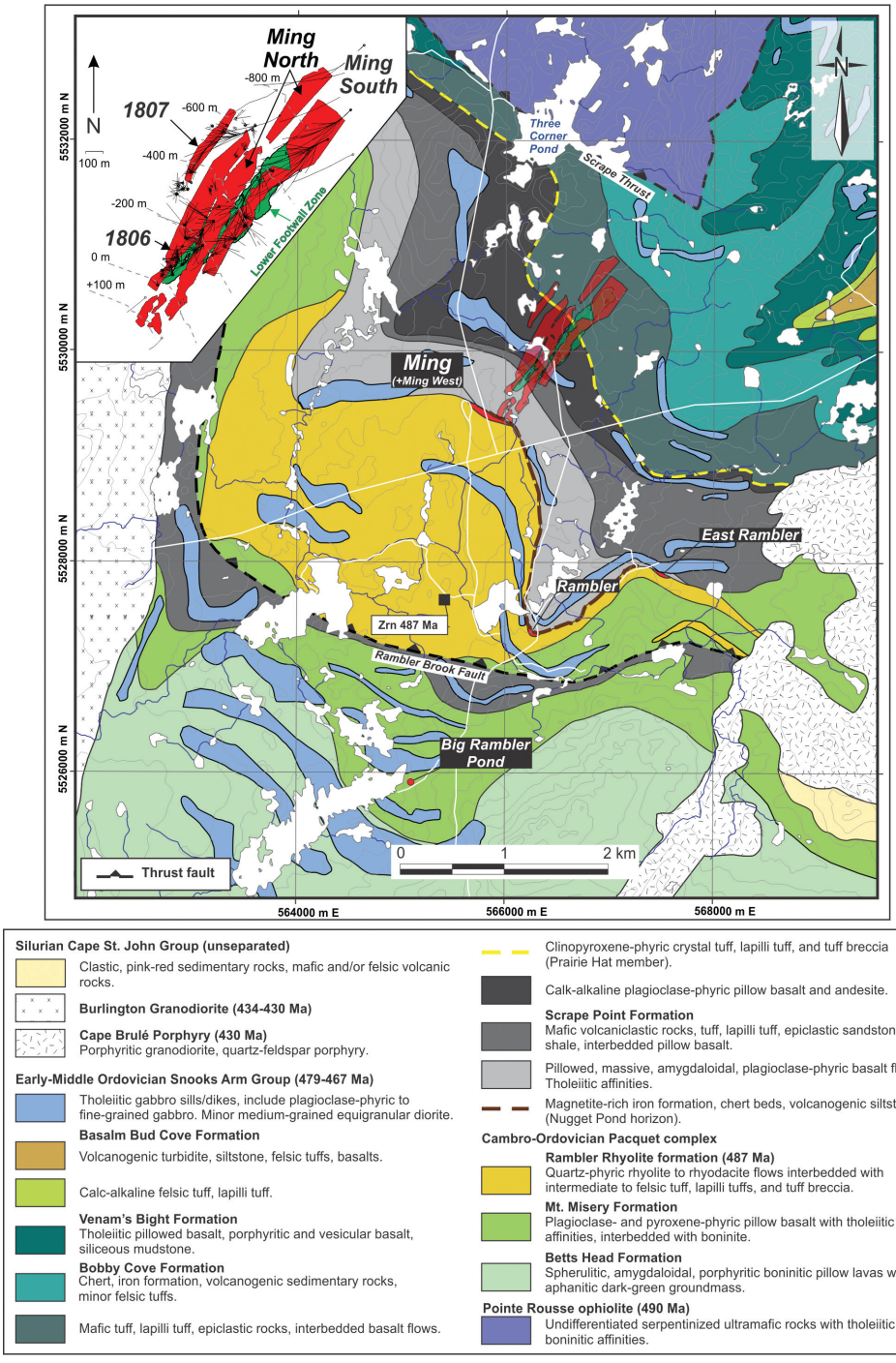

Fig. 2. Geological map of the study area, Baie Verte Peninsula, with Ming VMS orebodies projected to surface (also in the inset) and shown in light red and light green (Lower Footwall Zone = stockwork). Datum is UTM 21N NAD 83. Map compiled and modified from Tuach and Kennedy (1978), Hibbard (1983), Castonguay and others (2009), Pilgrim (2009), and Skulski and others (2010). The U-Pb zircon (Zrn) age is from Skulski and others (2015).

van Staal and Barr, 2012; van Staal and others, 2013). The Baie Verte oceanic tract consists of four ophiolitic bodies of identical age (*ca.* 490 Ma) that have similar geological assemblages and metallogeny (Hibbard, 1983; Dunning and Krogh, 1985; Cawood and others, 1996; Bédard and Escayola, 2010; Skulski and others, 2010, 2015). The four ophiolitic assemblages are the Betts Cove, Pacquet, Pointe Rousse, and Advocate complexes (fig. 1; Skulski and others, 2015) and consist of complete to incomplete oceanic crust assemblages that range from variably serpentinized mantle rocks (dunite and harzburgite), overlain by ultramafic cumulate sections, transitioning upward to isotropic gabbros to sheeted dikes, and pillowed boninites of the Betts Head Formation (fig. 2; Bédard and others, 1996). Conformably overlying boninitic rocks are mafic island arc tholeiites and felsic volcanic rocks of variable thicknesses belonging to the Mount Misery and Rambler Rhyolite formations, respectively (fig. 2). Collectively, the extrusive volcanic rocks of the Baie Verte oceanic tract reach a maximum structural thickness of 5 km in the Pacquet complex, including the Rambler Rhyolite formation, which is host to the Ming deposit.

The Baie Verte oceanic tract is fault bounded to the west by the Baie Verte-Brompton Line and to the east by the Green Bay Fault, juxtaposing ophiolitic rocks with the metamorphosed Neoproterozoic to Upper Cambrian sedimentary rocks of the Laurentian paleo-margin (Fleur de Lys Supergroup) in the west, and the Middle to Upper Cambrian (510–501 Ma) Lushs Bight oceanic tract in the east (fig. 1; for example, van Staal and Barr, 2012). The Lushs Bight oceanic tract comprises a ~505 Ma oceanic assemblage with abundant boninite and primitive oceanic island arc tholeiites (Kean and others, 1995; Swinden, 1996; Swinden and others, 1997). Both the Baie Verte and Lushs Bight oceanic tracts are interpreted to have formed in a supra-subduction zone, probably during their infancy, but the latter is older and was already emplaced onto Dashwoods block by *ca.* 490 Ma, synchronous with the early development of the Baie Verte oceanic tract (Szybinski, ms, 1995; Swinden and others, 1997; Bédard and others, 1998; van Staal and others, 1998, 2007, 2009).

The Upper Pacquet Complex, Ming Deposit, and Cover Sequence

In the Pacquet complex, the Rambler Rhyolite formation forms an approximately 3×5 km dome-shaped felsic complex formed by polyphase deformation (Castonguay and others, 2014). It is overlain and underlain, at least locally, by the mafic-dominated successions of the Mount Misery Formation. Recent detailed work by Pilote and others (2017) distinguished three lithofacies units forming the upper 1 km of the Rambler Rhyolite formation; 1) at the bottom, a coherent facies that consists of quartz-phyric to aphanitic felsic volcanic rocks (unit 1.1), sharply transitional to 2) multiple successions of quartz-bearing felsic bedded to massive volcaniclastic rocks of different fragment sizes (unit 1.2), overlain by 3) a thin blue quartz-phyric to quartz-megacrystic felsic coherent lava flow laterally transitioning to bedded quartz-bearing felsic tuffs (unit 1.3) (fig. 3). Both units 1.2 and 1.3 are fault bounded and/or controlled by synvolcanic faults (fig. 3). The mineralized zones of the Ming deposit occur as massive-sulfide to semi-massive sulfide ruler-shaped lenses, located at the very top of the felsic complex, and they plunge 30 to 35° to the northeast with significant variations in Cu, Zn, Ag, and Au grades (fig. 2; Brueckner and others, 2014, 2016). The 1806 Zone (fig. 2) represents the most precious metal-rich massive sulfide lens with Ag and Au grades of up to 15.07 g/t and 2.97 g/t, respectively. A Cu-rich stringer zone underlies the sulfide lenses, which represents the stockwork (for example, Lydon, 1984) of the deposit. Hydrothermal alteration is ubiquitous in the Ming deposit, although it is highly variable in intensity (Pilote and others, 2015). In the context of the potential mobility of some geochemical elements, alteration is addressed in Appendix A.

The stratigraphic successions that immediately overly the Rambler Rhyolite formation are part of the regionally extensive and correlative Lower to Middle

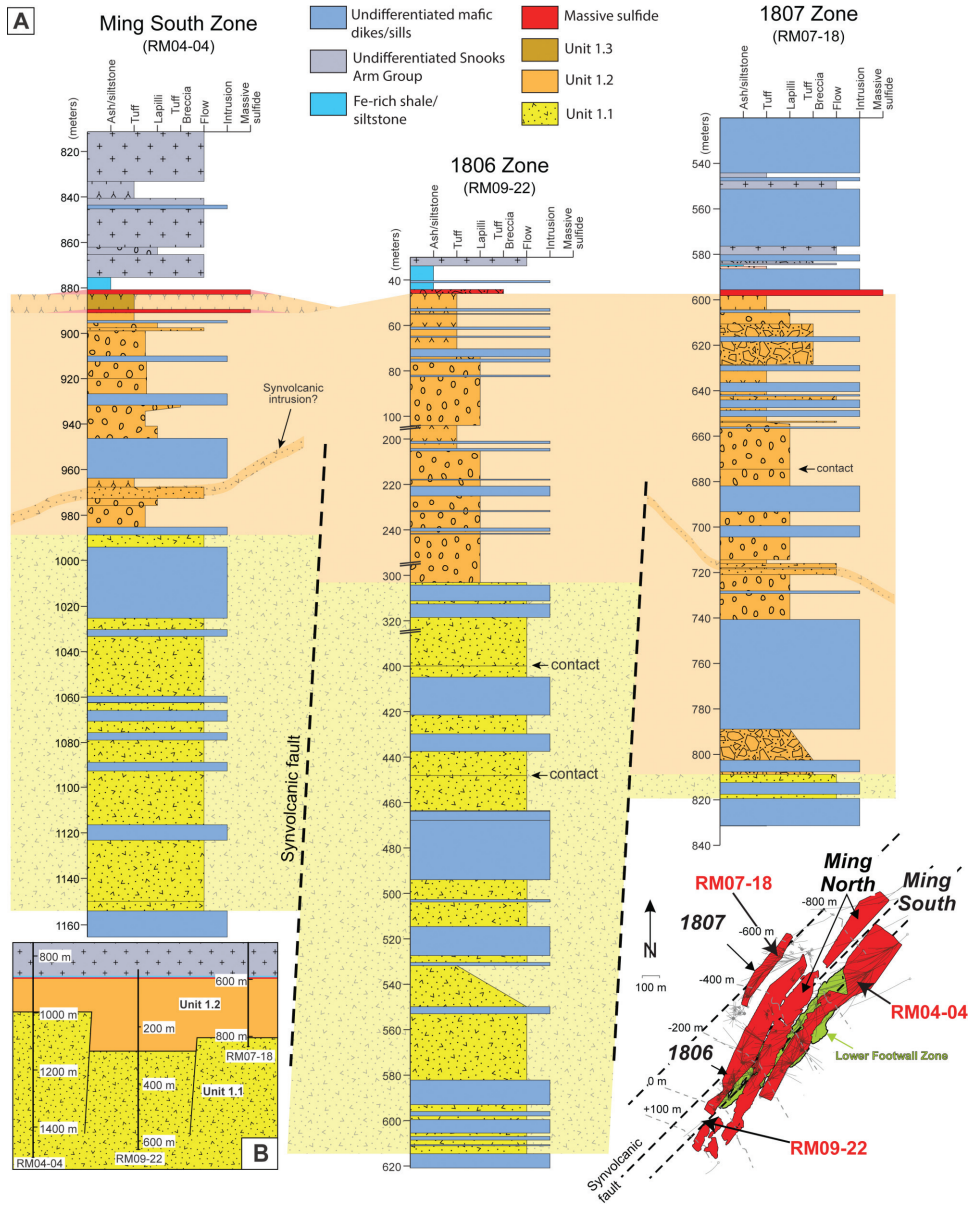

Fig. 3. Composite stratigraphic columns of the Ming South (DDH RM04-04), 1806 (RM09-22), and 1807 (RM07-18) zones. These illustrate the volcaniclastic lithofacies associated with all zones. Note the downhole breaks of lengths in drill hole RM09-22. The synvolcanic faults are interpreted based on the sharp lateral change in lithofacies and on the distribution of the chlorite-rich alteration spatially and genetically associated with the Lower Footwall Zone (Pilote and others, 2017).

Ordovician Snooks Arm Group (also referred to as the cover sequence; Skulski and others, 2010, 2015). At the Ming deposit, the base of the cover sequence is a spatially restricted mafic volcanic breccia with up to 10 volume percent sulfide clasts (unit 2; Pilote and others, 2016). This unit is conformably overlain by a thin (≤1 m), dark purple to black, finely laminated shale to siltstone (unit 3), which is considered

equivalent to the Nugget Pond horizon regionally (Skulski and others, 2010, 2015). The latter is overlain by multiple successions of mafic tuff, tuff breccia, and massive flows that are compositionally indistinguishable visually. All the rocks above are cross-cut by multiple generations of mafic sills and dikes (Pilote and others, 2017); however, these intrusive rocks are geochemically distinctive. Lastly, a major south-directed thrust fault, namely the Rambler Brook Fault, truncates the base of the Rambler Rhyolite formation, structurally juxtaposing the felsic complex with stratigraphically lower parts of the Snooks Arm Group (fig. 2).

Lithogeochemistry and whole-rock Sm-Nd isotope compositions of the Pacquet complex and cover sequence

The average major and trace element geochemistry for 92 samples of all units from the Ming deposit, intrusive rocks, and the lower 150 m of the cover sequence are summarized in table 1. Of these samples, 22 were selected for Nd isotopic analyses; the sample descriptions and results are presented in tables 2 and 3, respectively. Analytical procedures for both whole-rock and isotopic geochemistry are explained in detail in Appendix B. Analytical accuracy and precision values for each element are also presented in Appendix B. It is noteworthy that felsic rocks of the Rambler Rhyolite formation have all experienced some degree of hydrothermal alteration, in addition to regional upper greenschist metamorphism (for example Castonguay and others, 2014). The list presented here represents a set of least-altered samples that were chosen based on a rigorous set of criteria, which are described in Appendix A. The data presented here are supplemented by previously published data from Piercey and others (1997), Kean and others (1995), and Bédard (1999) and will be discussed below. The complete geochemical dataset is available in a digital supplement to this paper (http://earth.geology.yale.edu/%7eajs/SupplementaryData/2018/Pilote).

Footwall Coherent Felsic Volcanic and Felsic Volcaniclastic Rocks (Units 1.1 and 1.2)

The coherent (unit 1.1) and volcaniclastic (unit 1.2) lithofacies in the footwall of the Ming deposit display similar geochemical compositions (fig. 4; table 1). Both have andesitic compositions (fig. 4A); however, the SiO_2 (= 68.12–71.50 wt %) contents are much higher than normal andesitic rocks and are more akin to dacites or rhyodacites (fig. 4B). The units have calc-alkalic affinities (Ross and Bédard, 2009) (fig. 4C; table 1) and Yb_{cn} values and $[La/Yb]_{cn}$ ratios (cn = chondrite normalized) like FII-type rhyolites (fig. 5A), and Y values and Zr/Y ratios similar to FI- and FII-type rhyolites (fig. 5B) (Lesher and others, 1986; Hart and others, 2004). Some of the key geochemical features are the extremely low Zr (57–63 ppm) and Y (6.51–6.59 ppm) contents in these rocks (table 1). On a primitive mantle-normalized plot they have moderate to strong negative Nb ($Nb/Nb^* = \sim 0.6$) and Ti ($Ti/Ti^* = 0.19$) anomalies, positive Zr ($Zr/Zr^* = 2.3–2.5$) anomalies, and weak negative Eu ($Eu/Eu^* = \sim 0.95$) and Y ($Y/Y^* = \sim 0.75$) anomalies (fig. 6A; table 1). The ΣREE in units 1.1 and 1.2 is 8 to 19 times chondritic values, and samples exhibit LREE-enrichment ($[La/Sm]_{pn} = \sim 4.0$) with depleted HREE that are near primitive mantle values (fig. 6A). Two unaltered samples from unit 1.1 show an $\varepsilon Nd_{(t)}$ of −1.5 and −1.8, whereas altered samples from both unit 1.1 and 1.2 yielded $\varepsilon Nd_{(t)}$ ranging between −2.5 and −1.1 (table 3). The unaltered samples of felsic volcanic rocks located at the same stratigraphic horizon (Skulski and others, 2015) collected (~4 km) south of the Ming deposit by Piercey and others (1997) share similar geochemical characteristics (fig. 6A) to units 1.1 and 1.2.

Syn-mineralization Felsic Volcanic Rocks (Unit 1.3)

The thin (<10 m) blue quartz-bearing coherent and volcaniclastic lithofacies overlying unit 1.2 is intimately associated with the massive sulfide lenses (fig. 3; Pilote and others, 2017). Although this unit has previously been mapped and laterally

TABLE 1

Average Chemical Composition of Least Altered Host Rocks of the Ming Cu-Zn-Ag-Au VMS Deposit

	Rambler Rhyolite									Snooks Arm Group					
	Coherent facies Unit 1.1			Volcaniclastic facies Unit 1.2			Felsic tuff Unit 1.3			Sulfide-bearing mafic breccia Unit 2			Magnetite-rich shale (Nugget Pond horizon) Unit 3		
	Mean	2σ	n	Mean	2σ	n	Mean	2σ	n	Mean	2σ	n	Mean	2σ	n
SiO_2	71.50	2.68	3	68.12	10.71	23	65.64	9.13	3	49.19	8.88	3	50.30	3.73	9
Al_2O_3	12.58	0.84	3	13.48	2.96	23	16.07	2.74	3	17.83	0.77	3	16.93	2.23	9
$Fe_2O_{3(total)}$	4.48	0.91	3	6.24	4.79	23	4.58	4.89	3	9.75	4.75	3	8.18	1.65	9
MnO	0.052	0.021	3	0.163	0.526	23	0.034	0.020	3	0.120	0.147	3	0.151	0.080	9
MgO	2.94	0.91	3	2.31	3.87	23	1.84	1.83	3	4.07	2.79	3	4.51	3.59	9
CaO	2.20	1.58	3	3.35	2.48	23	3.18	0.90	3	6.79	6.58	3	8.63	3.86	9
Na_2O	4.06	0.08	3	3.46	1.48	23	4.16	1.26	3	3.46	0.72	3	4.05	2.69	9
K_2O	0.37	0.26	3	1.33	1.32	23	1.83	0.63	3	2.40	1.83	3	1.05	1.70	9
TiO_2	0.211	0.049	3	0.203	0.072	23	0.300	0.197	3	1.674	0.087	3	1.347	0.640	9
P_2O_5	0.05	0.00	3	0.05	0.04	23	0.06	0.11	3	0.10	0.05	3	0.13	0.04	9
LOI	1.53	0.31	3	1.05	0.97	23	1.51	0.39	3	3.82	5.46	3	4.74	3.58	9
Total	99.97	1.05	3	99.8	1.6	23	99.21	1.05	3	99.19	1.31	3	100.02	1.51	9
FeO_t[1]	4.03	0.82	3	5.61	4.31	23	4.12	4.40	3	8.77	4.27	3	7.36	1.48	9
Sr	113	71	3	157	93	23	246	229	3	190	127	3	231	127	9
Sc	17	4	3	22	15	23	18	18	3	31	2	3	28	6	9
Zr	63	8	3	57	20	23	80	22	3	123	8	3	106	29	9
Ba	47.6	21.0	3	308.7	574.9	23	463.4	481.3	3	260.5	202.3	3	125.2	357.9	9
Y	6.59	1.71	3	6.51	3.48	23	5.64	1.65	3	17.54	2.51	3	17.88	4.17	9
Nb	3.24	2.16	3	2.94	1.49	23	2.51	2.04	3	2.92	2.77	3	3.81	2.26	9
Cs	0.43	0.59	3	0.76	0.63	23	0.84	0.30	3	1.17	0.54	3	1.02	1.26	9
La	8.59	3.37	3	7.01	2.49	23	10.84	3.49	3	7.50	1.35	3	8.75	2.41	9
Ce	17.61	6.39	3	15.05	6.53	23	22.16	5.40	3	18.79	1.97	3	20.54	5.75	9
Pr	1.91	0.58	3	1.67	0.56	23	2.50	0.89	3	2.73	0.33	3	2.74	0.70	9
Nd	7.03	1.98	3	6.06	2.11	23	9.00	3.54	3	12.35	1.38	3	11.83	2.92	9
Sm	1.37	0.37	3	1.28	0.49	23	1.75	0.64	3	3.31	0.44	3	3.08	0.75	9
Eu	0.37	0.11	3	0.35	0.14	23	0.55	0.15	3	1.22	0.30	3	1.08	0.25	9
Gd	1.23	0.25	3	1.17	0.51	23	1.41	0.41	3	3.75	0.44	3	3.43	0.85	9
Tb	0.21	0.04	3	0.19	0.09	23	0.20	0.02	3	0.61	0.10	3	0.57	0.14	9
Dy	1.18	0.24	3	1.20	0.60	23	1.19	0.26	3	3.85	0.59	3	3.59	0.96	9
Ho	0.26	0.06	3	0.26	0.13	23	0.23	0.07	3	0.78	0.15	3	0.74	0.19	9
Er	0.80	0.19	3	0.78	0.43	23	0.62	0.19	3	2.15	0.47	3	2.05	0.50	9
Tm	0.13	0.03	3	0.14	0.07	23	0.09	0.02	3	0.32	0.05	3	0.31	0.08	9
Yb	0.83	0.20	3	0.88	0.49	23	0.54	0.10	3	1.87	0.46	3	1.83	0.45	9
Lu	0.14	0.03	3	0.14	0.08	23	0.07	0.01	3	0.25	0.08	3	0.25	0.06	9
Ta	bdl			0.23	0.11	15	0.24	0.13	2	0.23	0.25	2	0.29	0.17	9
Tl	0.08	0.06	3	2.08	4.54	23	3.04	6.37	3	3.05	2.88	3	4.72	16.45	9
Pb	4.8	2.9	3	24.0	41.3	23	10.9	3.6	2	55.4	21.9	3	22.6	33.5	9
Bi	0.05	0.05	3	0.26	0.39	23	0.14	0.12	3	0.53	0.08	3	0.61	2.55	9
Th	3.60	1.12	3	2.58	1.04	23	4.05	1.19	3	1.72	0.53	3	1.94	0.61	9
U	1.42	0.51	3	0.84	1.26	23	2.19	3.73	3	1.68	3.37	3	1.22	0.94	9
V	64.2	30.9	3	108.8	98.6	23	95.9	60.2	3	145.7	99.3	3	167.7	41.9	9
Cr	100.5	78.9	3	105.9	305.6	23	80.9	88.1	3	265.5	125.4	3	153.4	134.8	9
Co	10.5	4.1	3	11.9	15.4	23	8.8	3.7	3	24.4	6.4	3	26.0	9.4	9
Ni	22.7	17.2	3	28.6	62.4	21	16.2	9.9	3	64.8	50.6	3	57.1	41.2	9
Cu	48	37	3	92	210	23	13	14	2	416	320	3	106	135	9
Zn	68	51	3	152	239	23	72	25	2	124	80	3	96	39	9
As	1.0	1.0	2	2.6	3.0	19	0.6	0.5	2	2.8	0.6	3	3.9	6.0	9
Ag	0.1	0.1	3	0.1	0.0	2	1.7		1	0.2		1	0.3	0.4	2
Sn	0.7	0.4	3	0.8	0.5	23	0.8	0.3	3	1.2	0.3	3	1.5	2.0	9
Sb	0.2	0.1	2	0.5	0.7	21	2.3	5.7	3	1.0	0.7	3	1.0	1.7	9
Ti[2]	3804	133	3	3430	1212	23	5006	3282	3	27938	1459	3	22476	10677	9
Mg#[3]	56.37	7.60	3	38.46	26.56	23	44.42	9.15	3	44.97	18.16	3	50.30	19.54	9
$[La/Yb]_{cn}$[4]	6.82	1.17	3	5.59	2.30	23	13.75	6.91	3	2.70	0.20	3	3.22	0.76	9
Yb_{cn}	3.79	0.93	3	3.98	2.23	23	2.45	0.46	3	8.49	2.09	3	8.31	2.05	9
$[La/Yb]_{pn}$[5]	7.32	1.26	3	6.00	2.47	23	14.75	7.41	3	2.89	0.22	3	3.45	0.81	9
$[La/Sm]_{pn}$	4.03	0.54	3	3.57	0.58	23	4.03	0.78	3	1.47	0.14	3	1.86	0.53	9
$[Gd/Lu]_{pn}$	1.08	0.12	3	1.11	0.43	23	2.37	0.94	3	1.87	0.47	3	1.74	0.38	9
Nb/Nb*[6]	0.60	0.34	3	0.64	0.24	23	0.45	0.41	3	0.72	0.65	3	0.89	0.50	9
Ti/Ti*[7]	0.19	0.03	3	0.19	0.05	23	0.24	0.13	3	0.93	0.11	3	0.77	0.30	9
Zr/Zr*[8]	2.50	0.11	3	2.33	0.55	23	2.86	0.41	3	2.96	0.05	3	2.65	0.50	9
Eu/Eu*[9]	0.96	0.19	3	0.95	0.25	23	1.31	0.31	3	1.96	0.40	3	1.81	0.25	9
Y/Y*[10]	0.76	0.12	3	0.74	0.22	23	0.68	0.12	3	1.17	0.11	3	1.22	0.15	9

TABLE 1
(continued)

	Snooks Arm Group											
	High-Mg basalt			Th-enriched back-arc basin basalt			Enriched mid-ocean ridge basalt			LREE-enriched/Low-Ti tholeiitic mafic tuff		
	Mean	2σ	n	Mean	2σ	n	Mean	2σ	n	Mean	2σ	n
SiO_2	49.83	5.66	3	47.12	3.15	4	46.89	5.36	2	54.61	1.92	2
Al_2O_3	17.17	1.18	3	16.63	1.52	4	15.27	1.27	2	16.72	0.56	2
$Fe_2O_{3(total)}$	7.57	0.27	3	9.16	0.62	4	13.55	1.14	2	8.35	0.78	2
MnO	0.136	0.015	3	0.145	0.014	4	0.174	0.010	2	0.126	0.030	2
MgO	6.73	3.92	3	6.09	0.69	4	6.97	2.16	2	4.89	1.95	2
CaO	7.12	4.08	3	9.74	2.17	4	8.84	0.46	2	5.88	0.79	2
Na_2O	4.26	2.25	3	4.09	0.63	4	3.19	0.45	2	3.93	0.31	2
K_2O	0.37	0.49	3	0.50	0.49	4	0.26	0.19	2	1.24	0.32	2
TiO_2	1.095	0.422	3	1.244	0.136	4	2.220	0.277	2	0.646	0.077	2
P_2O_5	0.10	0.08	3	0.12	0.03	4	0.25	0.02	2	0.17	0.07	2
LOI	5.08	3.61	3	4.44	2.67	4	1.79	2.56	2	2.42	2.20	2
Total	99.47	0.90	3	99.27	1.14	4	99.39	1.82	2	98.97	1.04	2
FeO_t[1]	6.81	0.25	3	8.24	0.56	4	12.19	1.03	2	7.51	0.70	2
Sr	219	99	3	224	47	4	190	81	2	279	128	2
Sc	28	1	3	34	3	4	44	9	2	19	2	2
Zr	91	40	3	87	13	4	154	14	2	89	21	2
Ba	83.1	169.1	3	65.1	48.4	4	27.3	17.9	2	256.4	43.0	2
Y	16.47	8.57	3	20.77	2.61	4	30.16	5.83	2	14.46	0.54	2
Nb	3.04	3.09	3	1.83	0.74	4	6.93	3.67	2	4.08	2.22	2
Cs	0.34	0.28	3	0.73	0.82	4	0.26	0.19	2	2.10	0.45	2
La	8.16	1.41	3	3.65	0.45	4	8.45	1.84	2	12.22	1.33	2
Ce	18.35	4.28	3	10.78	1.50	4	23.18	2.32	2	25.64	3.22	2
Pr	2.46	0.74	3	1.85	0.28	4	3.63	0.02	2	3.09	0.50	2
Nd	10.11	3.28	3	9.18	1.02	4	17.11	0.78	2	12.25	1.83	2
Sm	2.66	1.24	3	2.87	0.51	4	4.92	0.63	2	2.67	0.25	2
Eu	0.92	0.45	3	0.98	0.25	4	1.67	0.25	2	0.86	0.03	2
Gd	2.99	1.48	3	3.56	0.63	4	5.80	0.98	2	2.67	0.16	2
Tb	0.50	0.27	3	0.62	0.08	4	0.95	0.17	2	0.45	0.01	2
Dy	3.13	1.52	3	3.97	0.42	4	5.96	1.17	2	2.69	0.15	2
Ho	0.66	0.33	3	0.83	0.09	4	1.22	0.24	2	0.55	0.04	2
Er	1.88	0.97	3	2.37	0.22	4	3.31	0.59	2	1.60	0.04	2
Tm	0.31	0.09	3	0.37	0.07	4	0.48	0.14	2	0.24	0.03	2
Yb	1.72	0.78	3	2.04	0.13	4	2.91	0.57	2	1.51	0.18	2
Lu	0.25	0.14	3	0.29	0.02	4	0.40	0.08	2	0.21	0.02	2
Ta	0.29	0.09	2	0.13	0.02	4	bdl			0.33		1
Tl	0.28	0.57	3	0.21	0.11	4	0.08	0.10	2	0.43	0.28	2
Pb	7.6	5.8	3	8.4	3.3	4	11.7	1.7	2	12.1	6.4	2
Bi	0.10	0.04	3	0.09	0.02	4	0.18	0.07	2	0.14	0.06	2
Th	2.49	1.13	3	0.35	0.16	4	0.97	0.12	2	3.61	1.17	2
U	1.34	0.33	3	0.24	0.10	4	0.23	0.01	2	1.49	0.15	2
V	163.5	5.7	3	209.9	23.2	4	352.4	23.6	2	113.6	5.1	2
Cr	198.6	180.3	3	199.6	25.8	4	159.8	44.6	2	135.7	22.6	2
Co	28.7	14.9	3	33.3	0.5	4	45.7	12.0	2	20.7	3.1	2
Ni	83.7	94.9	3	50.9	7.2	4	54.2	22.1	2	62.3	14.7	2
Cu	78	72	3	80	23	4	194	294	2	185	85	2
Zn	70	13	3	84	12	4	123	43	2	77	6	2
As	3.0	3.4	2	1.0	0.4	3	bdl			0.5		1
Ag	bdl			0.1		1	0.2		1	0.2		1
Sn	1.5	1.6	3	2.8	7.5	4	1.4	0.2	2	1.1	0.2	2
Sb	1.0	1.7	3	0.5	0.2	4	0.5	0.3	2	0.2	0.1	2
Ti[2]	18271	7042	3	20749	2276	4	37035	4622	2	10771	1285	2
Mg#[3]	62.37	14.65	3	56.83	1.90	4	50.19	5.70	2	53.15	12.34	2
$[La/Yb]_{cn}$[4]	3.30	1.22	3	1.20	0.09	4	1.98	0.81	2	5.43	0.05	2
Yb_{cn}	7.81	3.56	3	9.28	0.59	4	13.23	2.60	2	6.85	0.81	2
$[La/Yb]_{pn}$[5]	3.54	1.31	3	1.28	0.09	4	2.13	0.87	2	5.82	0.06	2
$[La/Sm]_{pn}$	2.06	0.75	3	0.82	0.05	4	1.12	0.39	2	2.95	0.04	2
$[Gd/Lu]_{pn}$	1.51	0.10	3	1.55	0.19	4	1.78	0.04	2	1.60	0.08	2
Nb/Nb*[6]	0.69	0.74	3	0.85	0.42	4	1.98	0.89	2	0.75	0.48	2
Ti/Ti*[7]	0.67	0.10	3	0.72	0.05	4	1.00	0.05	2	0.41	0.03	2
Zr/Zr*[8]	2.45	0.54	3	2.20	0.19	4	3.02	0.05	2	2.43	0.48	2
Eu/Eu*[9]	1.64	0.40	3	1.66	0.34	4	2.18	0.16	2	1.57	0.11	2

TABLE 1
(continued)

	Post-mineralization dikes and sills (feeders to the Snooks Arm Group and younger successions)											
	Low Nb/Yb tholeiitic gabbro IN1			Intermediate Nb/Yb tholeiitic gabbro IN2			Transitional diorite IN3			Calc-alkaline quartz monzodiorite IN4		
	Mean	2σ	n	Mean	2σ	n	Mean	2σ	n	Mean	2σ	n
SiO_2	45.36	5.23	9	46.63	1.81	7	45.62	8.62	9	58.24	5.54	15
Al_2O_3	16.42	1.65	9	15.72	2.01	7	14.34	2.40	9	16.49	1.85	15
$Fe_2O_{3(total)}$	10.11	1.70	9	11.47	2.10	7	11.11	5.75	9	5.73	0.99	15
MnO	0.153	0.023	9	0.255	0.404	7	0.182	0.103	9	0.100	0.125	15
MgO	7.92	1.66	9	6.81	1.06	7	5.98	3.95	9	3.88	1.91	15
CaO	10.14	2.98	9	10.02	2.96	7	9.67	4.83	9	5.16	1.95	15
Na_2O	2.85	1.05	9	2.77	1.07	7	3.00	1.15	9	4.29	1.49	15
K_2O	0.28	0.47	9	0.60	1.65	7	0.83	1.65	9	1.92	0.95	15
TiO_2	1.453	0.405	9	1.566	0.290	7	1.521	0.765	9	0.801	0.121	15
P_2O_5	0.14	0.03	9	0.16	0.05	7	0.21	0.13	9	0.28	0.16	15
LOI	4.72	6.19	9	3.57	2.52	7	6.45	8.41	9	2.77	3.11	15
Total	99.55	1.82	9	99.75	1.69	7	98.90	2.89	9	99.67	1.69	15
FeO_t[1]	9.09	1.53	9	10.32	1.89	7	10.00	5.18	9	5.15	0.89	15
Sr	232	44	9	268	147	7	178	117	9	231	219	15
Sc	37	7	9	40	10	7	35	19	9	14	5	15
Zr	98	23	9	100	30	7	108	45	9	129	62	15
Ba	30.0	55.6	9	86.1	197.6	7	90.1	123.2	9	391.3	414.8	15
Y	19.98	5.02	9	22.24	4.37	7	19.33	12.58	9	14.06	5.69	15
Nb	1.11	0.68	9	4.70	2.40	7	5.61	8.84	9	4.61	6.29	15
Cs	0.40	1.10	9	0.38	1.16	7	0.74	1.56	9	2.28	2.17	15
La	4.71	1.52	9	5.80	1.79	7	11.29	5.81	9	22.42	10.60	15
Ce	13.28	4.12	9	15.56	4.30	7	26.35	13.22	9	46.87	22.50	15
Pr	2.21	0.60	9	2.44	0.56	7	3.64	1.77	9	5.77	2.76	15
Nd	10.66	2.83	9	11.95	2.91	7	15.66	8.15	9	21.78	10.48	15
Sm	3.23	0.78	9	3.53	0.68	7	3.83	1.93	9	3.98	1.80	15
Eu	1.17	0.31	9	1.24	0.30	7	1.28	0.65	9	1.04	0.45	15
Gd	3.86	0.84	9	4.19	0.80	7	4.00	2.22	9	3.21	1.29	15
Tb	0.64	0.16	9	0.70	0.14	7	0.64	0.37	9	0.47	0.18	15
Dy	4.04	0.96	9	4.45	0.71	7	3.99	2.39	9	2.79	1.03	15
Ho	0.82	0.20	9	0.92	0.20	7	0.79	0.51	9	0.55	0.22	15
Er	2.28	0.61	9	2.50	0.50	7	2.15	1.42	9	1.55	0.56	15
Tm	0.33	0.09	9	0.37	0.07	7	0.33	0.19	9	0.24	0.09	15
Yb	1.94	0.52	9	2.19	0.44	7	1.85	1.33	9	1.36	0.53	15
Lu	0.28	0.08	9	0.31	0.08	7	0.26	0.17	9	0.19	0.07	15
Ta	0.09	0.05	7	0.29	0.09	6	0.38	0.51	6	0.42	0.41	8
Tl	0.29	0.76	9	0.65	2.52	6	2.01	5.05	9	3.45	7.78	15
Pb	17.0	23.0	9	7.7	15.2	7	52.8	119.2	9	40.2	81.9	15
Bi	0.19	0.20	9	0.13	0.10	7	1.49	3.97	9	2.94	17.52	15
Th	0.38	0.21	9	0.50	0.46	7	1.86	0.91	9	5.58	2.43	15
U	0.17	0.18	9	0.18	0.12	7	1.09	2.54	9	1.72	0.97	15
V	210.0	39.9	9	252.6	63.3	7	217.9	172.2	9	106.8	20.0	15
Cr	241.1	43.9	9	201.5	126.6	7	231.7	338.0	9	70.0	66.4	15
Co	42.1	8.2	9	40.9	8.4	7	39.9	19.7	9	18.6	5.7	15
Ni	90.6	36.5	9	69.5	46.4	7	77.6	103.1	9	67.6	63.7	15
Cu	145	266	9	95	73	7	497	1188	8	168	604	15
Zn	115	95	9	121	101	7	219	525	9	181	333	15
As	10.5	42.0	9	1.3	1.7	5	23.9	90.2	8	10.1	37.0	12
Ag	bdl			0.3		1	0.3	0.3	4	0.3	0.6	8
Sn	0.8	0.4	9	0.9	0.8	7	1.0	1.0	8	1.0	1.1	15
Sb	1.0	1.6	9	0.5	0.5	7	4.1	13.9	9	2.9	15.9	14
Ti[2]	24239	6759	9	26128	4846	7	25387	12758	9	13387	2082	15
Mg#[3]	60.76	2.97	9	54.07	7.29	7	50.85	23.93	9	56.53	10.36	15
$[La/Yb]_{cn}$[4]	1.64	0.61	9	1.77	0.22	7	4.30	2.00	9	10.99	2.98	15
Yb_{cn}	8.82	2.38	9	9.95	1.98	7	8.39	6.07	9	6.19	2.41	15
$[La/Yb]_{pn}$[5]	1.76	0.65	9	1.89	0.24	7	4.61	2.14	9	11.80	3.20	15
$[La/Sm]_{pn}$	0.94	0.18	9	1.06	0.23	7	1.91	0.33	9	3.64	0.34	15
$[Gd/Lu]_{pn}$	1.72	0.35	9	1.68	0.17	7	1.95	0.44	9	2.13	0.56	15
Nb/Nb*[6]	0.46	0.24	9	1.73	0.46	7	1.22	1.80	9	0.64	0.81	15
Ti/Ti*[7]	0.80	0.14	9	0.83	0.09	7	0.79	0.23	9	0.44	0.07	15
Zr/Zr*[8]	2.35	0.35	9	2.29	0.51	7	2.47	0.63	9	3.02	0.83	15
Eu/Eu*[9]	1.87	0.30	9	1.90	0.31	7	1.93	0.53	9	1.63	0.39	15
Y/Y*[10]	1.29	0.17	9	1.37	0.16	7	1.25	0.42	9	1.09	0.23	15

TABLE 1
(continued)

	Rambler Rhyolite									Snooks Arm Group					
	Coherent facies Unit 1.1			Volcaniclastic facies Unit 1.2			Felsic tuff Unit 1.3			Sulfide-bearing mafic breccia Unit 2			Magnetite-rich shale (Nugget Pond horizon) Unit 3		
	Mean	2σ	n	Mean	2σ	n	Mean	2σ	n	Mean	2σ	n	Mean	2σ	n
Zr/Y	9.70	1.51	3	9.23	4.63	23	14.41 290.8	4.29 142.9	3	7.02	0.83	3	5.96	1.53	9
Zr/TiO_2	302.89	38.60	3	283.46	64.68	23	4	3	3	73.37	8.55	3	81.37	28.80	9
Th/Yb	4.30	0.37	3	3.10	1.60	23	7.66	3.64	3	0.95	0.52	3	1.08	0.43	9
Al_2O_3/TiO_2	60.64	15.82	3	67.41	15.70	23	59.89	38.65	3	10.66	0.50	3	13.28	6.27	9
La/Yb	10.20	1.76	3	8.36	3.44	23	20.56	10.33	3	4.03	0.30	3	4.81	1.13	9
Nb/Y	0.48	0.24	3	0.47	0.29	23	0.43	0.24	3	0.17	0.15	3	0.21	0.12	9
Nb/Th	0.87	0.40	3	1.13	0.31	23	0.65	0.65	3	1.64	1.38	3	1.98	1.20	9
Nb/Yb	3.77	1.84	3	3.52	2.07	23	4.57	3.13	3	1.59	1.44	3	2.10	1.18	9

	Snooks Arm Group											
	High-Mg basalt			Th-enriched back-arc basin basalt			Enriched mid-ocean ridge basalt			LREE-enriched/Low-Ti tholeiitic mafic tuff		
	Mean	2σ	n	Mean	2σ	n	Mean	2σ	n	Mean	2σ	n
Zr/Y	5.61	0.90	3	4.19	0.48	4	5.13	0.53	2	6.11	1.22	2
Zr/TiO_2	83.15	10.27	3	69.94	6.89	4	69.46	2.36	2	136.62	16.24	2
Th/Yb	1.57	1.27	3	0.17	0.07	4	0.34	0.11	2	2.43	1.06	2
Al_2O_3/TiO_2	16.14	4.88	3	13.41	1.83	4	6.89	0.29	2	26.02	3.97	2
La/Yb	4.93	1.82	3	1.79	0.13	4	2.96	1.22	2	8.12	0.08	2
Nb/Y	0.18	0.14	3	0.09	0.04	4	0.24	0.17	2	0.28	0.14	2
Nb/Th	1.40	1.67	3	5.66	4.41	4	7.08	2.94	2	1.21	1.01	2
Nb/Yb	1.67	1.27	3	0.90	0.39	4	2.47	1.75	2	2.67	1.16	2

	Post-mineralization dikes and sills (feeders to the Snooks Arm Group and younger successions)											
	Low Nb/Yb tholeiitic gabbro IN1			Intermediate Nb/Yb tholeiitic gabbro IN2			Transitional diorite IN3			Calc-alkaline quartz monzodiorite IN4		
	Mean	2σ	n	Mean	2σ	n	Mean	2σ	n	Mean	2σ	n
Zr/Y	4.93	1.05	9	4.47	0.98	7	5.83	2.01	9	9.17	2.25	15
Zr/TiO_2	67.60	4.68	9	63.27	8.53	7	72.85	26.62	9	160.30	64.15	15
Th/Yb	0.20	0.10	9	0.22	0.17	7	1.10	0.73	9	4.14	1.46	15
Al_2O_3/TiO_2	11.46	2.53	9	10.12	2.28	7	10.08	5.65	9	20.63	1.86	15
La/Yb	2.45	0.91	9	2.64	0.33	7	6.43	2.99	9	16.44	4.46	15
Nb/Y	0.06	0.03	9	0.21	0.08	7	0.26	0.28	9	0.31	0.36	15
Nb/Th	3.05	2.03	9	10.51	5.42	7	3.03	4.63	9	0.83	1.05	15
Nb/Yb	0.58	0.40	9	2.12	0.74	7	2.78	3.17	9	3.27	3.89	15

[1]Calculated from Fe_2O_{3t}, assuming all iron is present as FeO.
[2]Calculated from TiO_2; 10000 x (TiO_2/0.5993).
[3]Mg# = $Mg^{2+}/(Mg^{2+} + Fe^{2+})$ (molar %).
[4]Normalized to Chondrite (cn) value (Nakamura, 1974).
[5]Normalized to Primitive Mantle (pn) value (Sun and McDonough, 1989).
[6]$Nb/Nb^* = Nb_n/(Th_n + La_n)^{0.5}$ (Normalized to Primitive Mantle).
[7]$Ti/Ti^* = Ti_n/(Gd_n + Sm_n)^{0.5}$ (Normalized to Primitive Mantle).
[8]$Zr/Zr^* = Zr_n/(Gd_n + Sm_n)^{0.5}$ (Normalized to Primitive Mantle).
[9]$Eu/Eu^* = Eu_n/(Gd_n + Sm_n)^{0.5}$ (Normalized to Primitive Mantle).
[10]$Y/Y^* = Y_n/(Dy_n + Er_n)^{0.5}$ (Normalized to Primitive Mantle).
bdl = below detection limit.

constrained to the Ming South Zone (Pilote and others, 2017), quartz-bearing tuff and synvolcanic dikes with similar geochemical characteristics have been locally observed below the 1807 Zone (drill hole RM07-18) and are thus considered as part of the same unit. Three representative samples have andesitic affinities (fig. 4A), but contain higher SiO_2 contents than typical andesite (fig. 4B; table 1). The samples of unit 1.3 have some of the highest Zr/Y ratios in the deposit (average of 14.4; fig. 4C; table 1), but with calc-alkalic affinities (Ross and Bédard, 2009). The samples have FI-type

TABLE 2

Sample Locations and Descriptions for Whole-Rock Nd Isotopic Analyses

Sample	Unit	Sample location (Zone; DDH/Level; Depth)	Description
106407	Unit 1.1	1806; RM09-22; 612 m	Dark bluish gray, coherent quartz-phyric (7 vol %), felsic flow with minor chlorite alteration
62521	Unit 1.1	1807; RM07-18; 823 m	Dark purple, coherent quartz-phyric felsic flow with minor silica alteration
62501	Unit 1.3	1807; RM07-18; 607 m	Fine-grained, dark purple, quartz-bearing felsic tuff with silica alteration
60591	Fe-shale (Unit 3)	1807; RM07-20K; 652 m	Fine-grained, laminated shale intercalated with well sorted, immature, siltstone/sandstone overprinted by magnetite-actinolite-chlorite porphyroblasts
60600	Fe-shale (Unit 3)	1807; RM07-18; 589 m	Finely laminated silstone overprinted by magnetite-actinolite-chlorite porphyroblasts
29885	Fe-shale (Unit 3)	1806; RM08-150; 76 m	Dark greenish to pinkish gray, bedded and laminated siltstone with minor shale
29896	Fe-shale (Unit 3)	1807; RM07-20H; 655 m	Dark greenish to pinkish gray, bedded and laminated siltstone with minor shale
62168	LREE/LOTI	Ming South; RM05-08; 915 m	Moderate gray, fine-grained, finely laminated mafic ash tuff/epiclastic, overprinted by biotite porphyroblasts
62175	E-MORB	Ming South; RM05-08; 960 m	Dark gray, fine-grained moderately chloritized mafic flow
62176	High-Mg	Ming South; RM05-08; 990 m	Mafic lapilli tuff with < 1cm bleached angular fragments in a fine-grained moderately chloritized matrix with biotite porphyroblasts
60584	IN1	1807; RM07-20M; 661 m	Dark gray, medium-grained gabbro overprinted by pyrite-actinolite-biotite porphyroblasts
36648	IN2	Ming South; RM04-04; 327 m	Dark gray, medium-grained, equigranular gabbro with minor chlorite alteration
62510	IN4	1807; RM07-18; 701 m	Dark purplish gray, fine-grained, hornblende microporphyritic intermediate intrusive rock

DDH = diamond drill hole; (d) = downhole.

rhyolite affinities (figs. 5A and 5B) with higher La/Yb and Z/Yb ratios than units 1.1 and 1.2; this unit also has higher Al_2O_3, TiO_2, Zr, and Th (table 1) and ΣREE (18 to 24 times chondritic values). In addition, rocks of unit 1.3 exhibit enrichment in LREE ($[La/Sm]_{pn}$ = 4.03) with depletion in HREE ($[Gd/Lu]_{pn}$ = 2.37) and Y (5.64 ppm) (fig. 6B; table 1). Moreover, the HREE and Y average values are lower, and MREE are higher than that of units 1.1 and 1.2 (table 1; fig. 6B). On a primitive mantle-normalized diagram, the rocks of unit 1.3 have moderate to strong negative Nb (Nb/Nb* = 0.45) and Ti (Ti/Ti* = 0.24) anomalies, positive Zr (Zr/Zr* = 2.86) anomalies, absent to weak positive Eu (Eu/Eu* = 1.31) anomalies, and weak negative Y (Y/Y* = 0.68) anomalies (fig. 6B; table 1). All units (1.1 to 1.3) show a strong positive Al anomaly on the primitive mantle-normalized extended element plots (figs. 6A and 6B). A sample of this unit has an $\varepsilon Nd_{(t)}$ of −1.5, and the two altered samples have values of −1.5 and −2.1 (table 3).

Sulfide-bearing Mafic Volcanic Breccia (Unit 2)

The sulfide-bearing volcaniclastic lithofacies immediately overlying parts of the massive sulfide in the 1806 and 1807 zones is dominated by basaltic lapilli sized fragments, although it is locally polylithic with felsic and basaltic fragments, with locally up to 10 volume percent sulfide clasts (Pilote and others, 2016). Representative

TABLE 3

Neodymium Isotopic Data for Representative Samples from the Ming Deposit and Area

Sample	Unit	Nd (ppm)	Sm (ppm)	$^{147}Sm/^{144}Nd_{(0)}$	$^{143}Nd/^{144}Nd_{(0)}$	$^{143}Nd/^{144}Nd_{(t)}$	$\varepsilon Nd_{(t)}$
Unaltered							
106407	Unit 1.1	5.34	1.10	0.1249	0.512336	0.511943	-1.5
62521	Unit 1.1	8.01	1.55	0.1170	0.512296	0.511928	-1.8
62501	Unit 1.3	7.80	1.61	0.1248	0.512334	0.511942	-1.5
60591	Fe-shale (Unit 3)	10.52	2.65	0.1521	0.512710	0.512232	4.1
60600	Fe-shale (Unit 3)	13.94	3.76	0.1632	0.512813	0.512300	5.5
29885	Fe-shale (Unit 3)	14.70	3.83	0.1575	0.512674	0.512179	3.1
29896	Fe-shale (Unit 3)	12.55	3.41	0.1644	0.512759	0.512242	4.3
62168	LREE/LOTI	10.04	2.30	0.1389	0.512433	0.511996	-0.5
62175	E-MORB	16.66	4.60	0.1670	0.512883	0.512358	6.6
62176	High-Mg	8.36	2.08	0.1505	0.512576	0.512103	1.6
60584	IN1	8.94	2.81	0.1901	0.512979	0.512381	7.1
36648	IN2	10.10	3.03	0.1814	0.512962	0.512392	7.3
62510	IN4	19.99	3.69	0.1116	0.512495	0.512144	2.4
Altered							
29952	Unit 1.2	2.61	0.51	0.1179	0.512313	0.511942	-1.5
60551	Unit 1.2	3.91	0.82	0.1273	0.512365	0.511965	-1.1
62506	Unit 1.2	5.05	1.00	0.1197	0.512268	0.511892	-2.5
29883	Unit 1.2	4.52	0.92	0.1234	0.512310	0.511922	-1.9
29827	Unit 1.2	4.84	1.00	0.1244	0.512334	0.511943	-1.5
29832	Unit 1.2	4.06	0.85	0.1262	0.512349	0.511952	-1.3
62525	Unit 1.3	4.83	0.88	0.1109	0.512257	0.511908	-2.2
62177	Unit 1.3	5.42	0.98	0.1096	0.512284	0.511939	-1.6
60587	IN3	21.23	5.00	0.1423	0.512587	0.512140	2.3

Note: $^{143}Nd/^{144}Nd_{(0)}$ and $^{147}Sm/^{144}Nd_{(0)}$ are measured values; analytical uncertainty in $^{143}Nd/^{144}Nd_{(0)}$ is ± 0.000007 or better; $^{143}Nd/^{144}Nd_{(t)}$ is initial ratio at t = 480 Ma; Present-day $^{143}Nd/^{144}Nd_{(CHUR)}$ and $^{147}Sm/^{144}Nd_{(CHUR)}$ values of 0.512638 and 0.1967, respectively, were used to calculate $\varepsilon Nd_{(t)}$.

samples of unit 2 collected from monolithic intersections have basaltic affinities (figs. 4A and 4B), with calc-alkalic Th/Yb (= 0.95) and Zr/Y (= 7.02) ratios (fig. 4C); however, these latter ratios are accentuated by both strong to weak positive Zr (Zr/Zr* = 2.96) and Y (Y/Y* = 1.17) anomalies (fig. 6C). In both the Th-Zr-Nb diagram of Wood (1980) and La-Y-Nb diagram of Cabanis and Lecolle (1989), samples of unit 2 show depletion of Nb relative to other HFSE, plotting in the arc fields (figs. 7A and 7B). Furthermore, on an extended elements-normalized diagram, unit 2 shares geochemical patterns similar to as typical low Ti-tholeiites with a weak LREE enrichment ($[La/Sm]_{pn}$ = 1.47) and positive Th and negative asymmetric Nb (Nb/Nb* = 0.72) anomalies (fig. 6C). Their low Al_2O_3/TiO_2 (= 10.66) ratios and high TiO_2 (= 1.674 ppm) and low V (= 145.7 ppm) contents are, however, inconsistent with low Ti-tholeiitic rocks (fig. 7C; Shervais, 1982) and are more similar to back-arc basin affinities.

Fe-rich Shale (Unit 3)

The thin (≤1 m) and extensive sedimentary sequence that overlies the Ming massive sulfide lenses, shares similar geochemical characteristics with unit 2. The fine-grained sedimentary rocks of unit 3 contain minimal variations in SiO_2 (= 48.01–53.08 wt %), Al_2O_3 (= 15.55–19.49 wt %), and Fe_2O_{3t} (= 6.70–9.40 wt %) and show SiO_2/Al_2O_3 and Fe_2O_{3t}/K_2O ratios that are typical of Fe-rich shale (fig. 7D; Herron, 1988), reflecting the high magnetite content in these rocks. Accordingly, the wide spread of Fe_2O_{3t}/K_2O ratios is due to the variations in K_2O (= 0.20 to 3.08 wt %; fig. 7D; table 1). For the sake of simplification, rocks of unit 3 will be hereafter

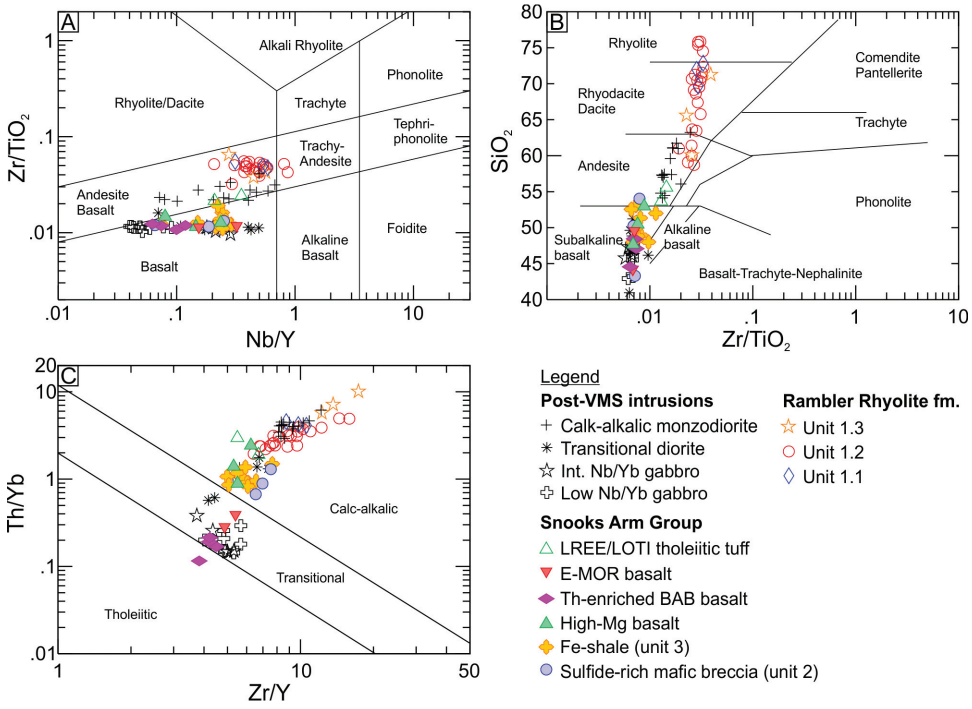

Fig. 4. Major and trace element plots of the average composition of the least altered samples of the host units and intrusive rocks of the Ming deposit. (A) Zr/TiO_2 vs. Nb/Y discrimination diagram from Winchester and Floyd (1977), revised by Pearce (1996). (B) Zr/TiO_2 vs. SiO_2 discrimination diagram from Winchester and Floyd (1977). (C) Th/Yb vs. Zr/Y discrimination diagram from Ross and Bédard (2009).

referred to as Fe-rich shale. The latter contains relatively low Th (= 1.44–2.58 ppm), Zr (= 81–125 ppm), and La (= 7.07–11.45 ppm), whereas Ni (= 28.5–84.9 ppm) and Sc (= 23–33 ppm) values are high. On a primitive mantle-normalized plot, the samples show weak negative Nb ($Nb/Nb^* = 0.89$) and weak positive Zr ($Zr/Zr^* = 2.65$) anomalies (fig. 6C) and much like the rocks of unit 2, the Fe-rich shale samples are strongly depleted in V (= 167.7 ppm). On a post-Archean Australian shale (PAAS)-normalized plot, the Fe-rich shale shows depletion in LREE and near flat MREE and HREE patterns, with moderate positive Eu anomalies, and devoid of Ce ($Ce/Ce^* \approx 1$) anomalies (fig. 6D). Four samples have $\varepsilon Nd_{(t)}$ ranging from +3.1 to +5.5 (table 3; fig. 8). Samples with lower Cr values and Mg# have more evolved $\varepsilon Nd_{(t)}$ values (tables 1 and 3).

Lower Section of the Snooks Arm Group (Hanging Wall)

The rocks that overly unit 2 and locally intercalated with the Fe-shale were recently combined as part of the Snooks Arm Group (Skulski and others, 2010, 2015) (fig. 1); herein, an emphasis is made on the 200 m section that overlies the Ming deposit. Figure 9 illustrates the intersected immediate hanging wall; although, the Fe-shale is absent here. The mafic-dominated volcanic and volcaniclastic successions show distinct geochemical characteristics and are described below.

High-Mg basalt.—The massive flows to volcaniclastic rocks of the lowermost Snooks Arm Group (fig. 9), which also represent the first pulse of volcanism in the Rambler area that post-dates the deposition of the Fe-shale, are basaltic in composition (SiO_2 =

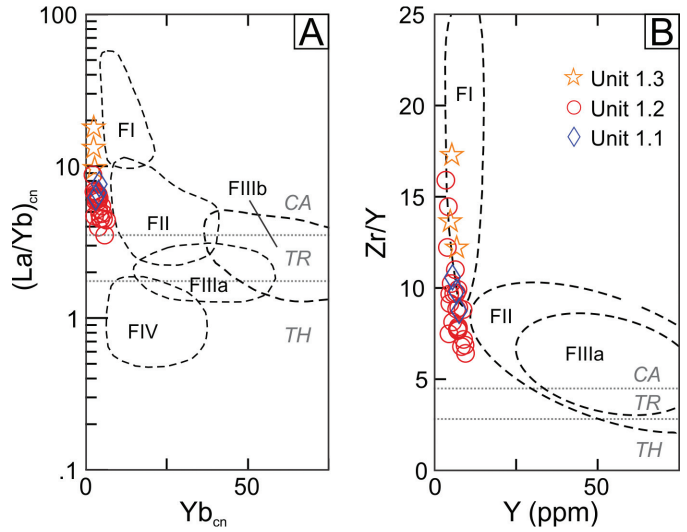

Fig. 5. Petrochemical affinity of the least-altered felsic rocks from the Rambler Rhyolite formation. (A) Chondrite-normalized $[La/Yb]_{cn}$ vs. Yb_{cn} and (B) Zr/Y vs. Y discrimination diagrams from Lesher and others (1986) and Hart and others (2004). Symbols are as in figure 4. CA = calc-alkalic, TH = tholeiitic, TR = transitional.

49.83 wt %; Zr/TiO_2 = 83.15; figs. 4A and 4B) and characterized by primitive Mg# (= 62.4) and high Cr (= ~200 ppm) and Ni (= ~84 ppm) values (table 1). Their Zr/Y (= 5.61) and La/Yb (= 10.20) ratios suggest a transitional affinity (Barrett and MacLean, 1999); however, the enrichment in Th (= ~2.5 ppm) relative to other HFSE and REE suggests a calk-alkalic affinity (fig. 4C; Ross and Bédard, 2009). The arc-like affinity is mirrored by low Nb/Th (≪5; Swinden and others, 1989) ratios and they plot in the arc-like fields of Wood (1980) and Cabanis and Lecolle (1989) (figs. 7A and 7B). On a primitive mantle-normalized diagram (fig. 9B), the high-Mg basalt shows enrichment in LREE ($[La/Sm]_{pn}$ = 2.06) with a weak positive Zr (Zr/Zr^* = 2.45) anomaly. An $\varepsilon Nd_{(t)}$ value of +1.6 was obtained from this unit (table 3; fig. 8).

Th-enriched back-arc basin basalt.—This unit consists of massive flows, locally variolitic and/or vesicular, and fragmental rocks of variable thicknesses, intercalated with other units of distinct geochemical affinities (fig. 9). The rocks are basaltic in composition with Zr/TiO_2 = 69.94, Nb/Y = 0.09, and SiO_2 = 47.12 weight percent (figs. 4A and 4B; Winchester and Floyd, 1977; Pearce, 1996). This unit shows fractionated Mg# (= 56.83) with no significant enrichment in Cr, Co, and Ni (table 1). This unit is tholeiitic to transitional based on Zr/Y (= 4.19) and Th/Yb (= 0.17) ratios (fig. 4C; Barrett and MacLean, 1999; Ross and Bédard, 2009) and plots both in the volcanic arc tholeiite and back-arc basin basalt fields on the La-Y-Nb plot (fig. 7B; Cabanis and Lecolle, 1989). This range is due to a systematic drop in Nb (and Eu) and concomitant increase in Th when moving up-stratigraphy. On a primitive mantle-normalized diagram, the rocks of this unit show depletion in LREE and HREE relative to MREE ($[La/Sm]_{pn}$ = 0.82 and $[Gd/Lu]_{pn}$ = 1.55) with a weak positive Zr (Zr/Zr^* = 2.20) anomaly (fig. 9C).

Enriched mid-ocean ridge basalt (E-MORB).—This unit consists of <25 m thick massive flows intercalated with pillow lavas of mafic composition (SiO_2 = 46.89 wt %; Zr/TiO_2 = 69.46; fig. 4B and C; Winchester and Floyd, 1977; Pearce, 1996) with fractionated Mg# (= 50.19). The two analyzed samples of this unit share similar

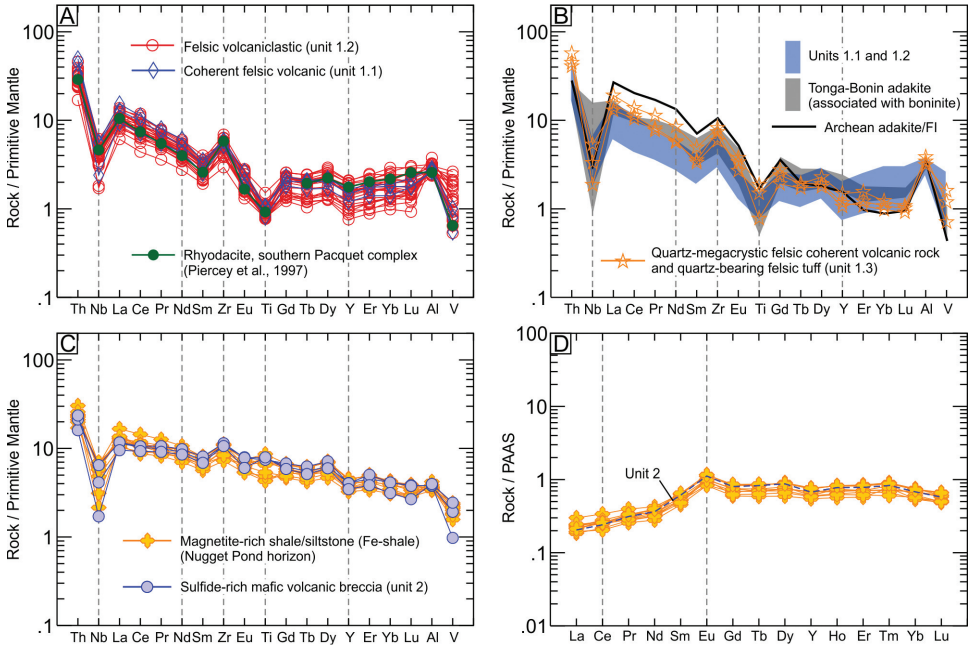

Fig. 6. Primitive mantle- and post-Archean Australian shale (PASS)-normalized extended-element plots for least-altered rocks of the Rambler Rhyolite formation and base of the Snooks Arm Group, subdivided based on geochemical criteria (see text for details). Also included is a rhyodacite sample from the southern Pacquet complex (Piercey and others, 1997), adakite associated with boninite in the Tonga (Falloon and others, 2008) and Bonin (Li and others, 2013) fore-arcs, and one adakite/FI-type felsic sample from the Archean Wawa greenstone belt, Superior Province (Polat and Kerrich, 2001). Normalizing values are those of Sun and McDonough (1989) and Taylor and McLennan (1985).

geochemical characteristics, except for one sample that shows a moderate negative Nb (Nb/Nb* = 1.98) anomaly (fig. 9D). The rocks have characteristically the lowest Al_2O_3/TiO_2 (= 6.89) ratios (and highest TiO_2) of all rocks analyzed and contain the highest Co and V values of the hanging wall volcanic succession, with averages of 45.7 ppm and 352.4 ppm, respectively (table 1). The basalt shows near-flat LREE to MREE patterns ($[La/Sm]_{pn}$ = 1.12) on primitive mantle-normalized diagrams with a weak depletion in HREE ($[Gd/Lu]_{pn}$ = 1.78) (fig. 9D). The samples straddle the boundary between the arc-basalt and E-MORB fields of Wood (1980) and the back-arc basin basalt (BABB) field of Cabanis and Lecolle (1989) (figs. 7A and 7B). Despite the latter ambiguous magmatic and tectonic affinities, the low Th/Yb and Zr/Y ratios reflect a transitional affinity typical for E-MORB and/or BABB (fig. 4C; Ross and Bédard, 2009), supported by their high Nb/Th ratio (>5), typical for non-arc-like basalts (Swinden and others, 1989). A representative sample of this unit yielded a primitive $\varepsilon Nd_{(t)}$ value of +6.6 (table 3; fig. 8).

LREE-enriched/Low-Ti calc-alkalic mafic tuff.—The rocks of this unit share similar geochemical characteristics with the high-Mg basalt (table 1), except that the mafic tuff is more enriched in LREE ($[La/Sm]_{pn}$ = 2.95) and shows a relatively strong negative Ti (Ti/Ti* = 0.41) anomaly, which is mirrored in the high Al_2O_3/TiO_2 and Zr/TiO_2 ratios (table 1). Based on the SiO_2 (= 54.64 wt %) content and Zr/TiO_2 (= 136.62) ratio, the rocks have andesitic affinities (figs. 4A and 4B). The rocks of this unit show variable but overall fractioned Mg# (= 53.15) and are characterized by low V (= 113.6 ppm), Cr (= 135.7 ppm), and Co (= 20.7 ppm). The high Th/Yb (= 2.43) ratios are

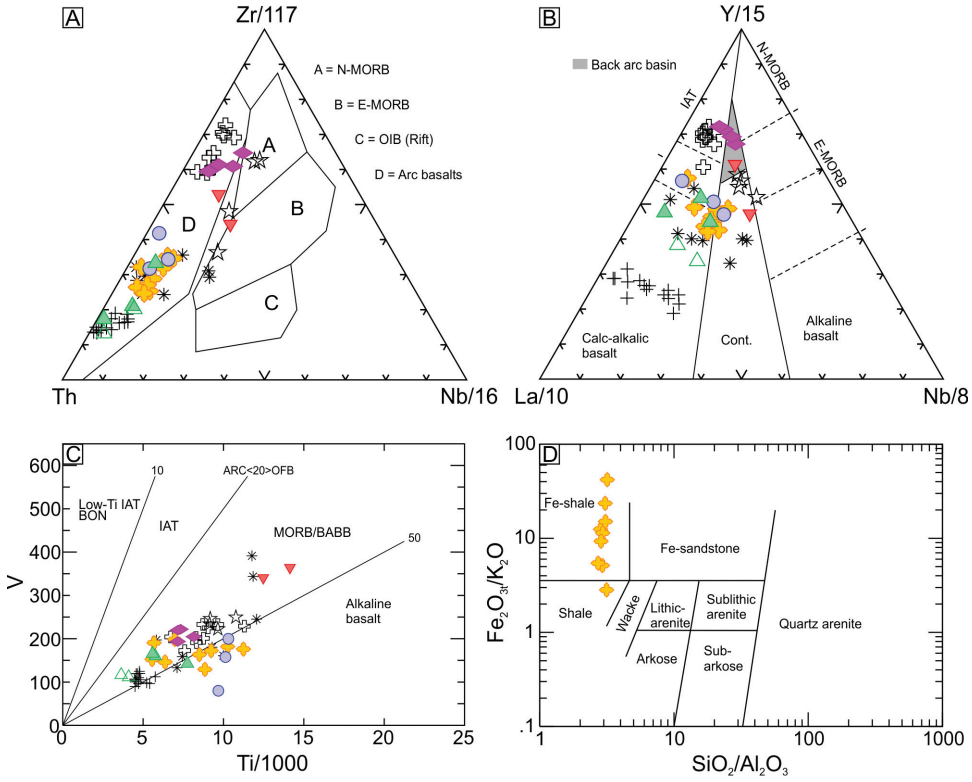

Fig. 7. Petrochemical affinity of the Snooks Arm Group. (A) Th-Zr-Nb discrimination diagram from Wood (1980). (B) Y-La-Nb discrimination diagram from Cabanis and Lecolle (1989). (C) V vs. Ti discrimination diagram from Shervais (1982). (D) Fe_2O_{3t}/K_2O vs. SiO_2/Al_2O_3 discrimination diagram from Herron (1988). Symbols are as in figure 4. BON = boninite, IAT = island arc tholeiite, OIB = ocean island basalt.

characteristic of calc-alkalic rocks (fig. 4C; Ross and Bédard, 2009), also reflected by low Nb/Th ratios (= 1.21) (Swinden and others, 1989) and the proportions of Th-Zr-Nb and La-Y-Nb in the rocks (figs. 7A and 7B). A sample from this unit yielded an $\varepsilon Nd_{(t)}$ value of -0.5, making this unit the most evolved rocks of the immediate cover sequence (table 3; fig. 8).

Post-VMS Mineralization Intrusions

The multiple generations of sills and dikes cross-cutting the host sequences at the Ming deposit can be divided into four distinct assemblages based on distinct geochemical characteristics, which are as follows: 1) low Nb/Yb and 2) intermediate Nb/Yb tholeiitic gabbros (IN1 of Pilote and others, 2015), 3) transitional diorite (IN2 of Pilote and others, 2015), and 4) calc-alkalic porphyritic quartz monzodiorite (IN3 of Pilote and others, 2015). The contact relationship between the low Nb/Yb gabbro and intermediate Nb/Yb gabbro is unclear; however, both the latter intrusive units are cross-cut by the transitional diorite followed by the calc-alkalic porphyritic quartz monzodiorite (Pilote and others, 2015).

Low Nb/Yb tholeiitic gabbro.—The coarse, melanocratic, equigranular gabbro shows a tholeiitic affinity on various discrimination diagrams (figs. 4C, 7A–7C); Irvine and Baragar, 1971; Barrett and MacLean, 1999; Ross and Bédard, 2009), although its high

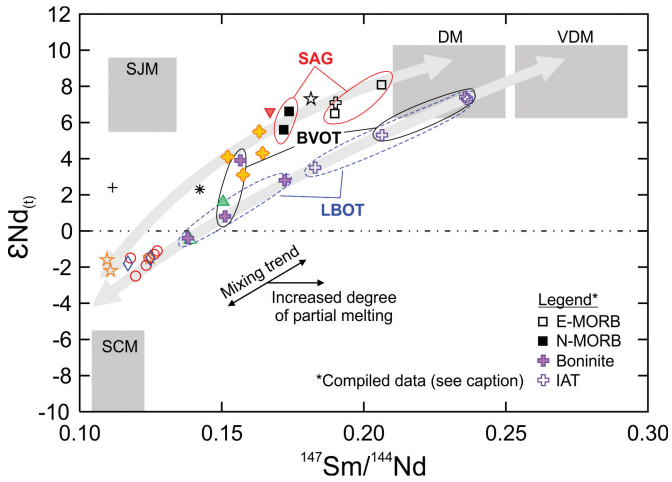

Fig. 8. $^{147}Sm/^{144}Nd$ vs. εNd(t) diagram for the altered and unaltered samples from the Rambler Rhyolite formation and Snooks Arm Group with various mantle and subduction components interpreted to be involved in its petrogenesis (fields from Swinden and others, 1990). Also shown are compiled values from Swinden and others (1997) for representative samples from the N- and E-MORB of the Snooks Arm Group, boninites and IAT from the Baie Verte and Lushs Bight oceanic tracts. BVOT = Baie Verte oceanic tract, DM = depleted mantle, IAT = island arc tholeiite, LBOT = Lushs Bight oceanic tract, SAG = Snooks Arm Group, SCM = subducted continental material, SJM = subducted juvenile material, VDM = very depleted mantle. Symbols are as in figure 4.

Zr (= 98 ppm) and low Y contents (= 19.98 ppm) is atypical for such a magmatic affinity (Barrett and MacLean, 1999). The rocks of this unit show a slight enrichment in LREE ($[La/Yb]_{pn}$ = 1.76) with a strong depletion in Nb on the extended element diagram (fig. 10A). Their high Zr/Y ratios, low Nb, La, and Th are consistent with rocks formed in volcanic arc settings (figs. 7A and 7B; Wood, 1980; Cabanis and Lecolle, 1989). A sample of low Nb/Yb tholeiitic gabbro yielded a primitive $εNd_{(t)}$ value of +7.1 (table 3; fig. 8).

Intermediate Nb/Yb tholeiitic gabbro.—This fine-grained porphyritic to coarse equigranular gabbro has a tholeiitic affinity (figs. 4C, 7A–7C); Irvine and Baragar, 1971; Barrett and MacLean, 1999; Ross and Bédard, 2009) and shares many geochemical similarities with the low Nb/Yb tholeiitic gabbro; however, with significant key major and trace element distinctions; for instance, their respective Mg# and Nb/Yb ratios (table 1; fig. 10C). The highly fractionated intermediate Nb/Yb tholeiitic gabbro generally contains higher V (= 252.6 ppm) and lower Ni (= 69.5 ppm) values than the low Nb/Yb tholeiitic gabbro. The intermediate Nb/Yb tholeiitic gabbro is slightly more enriched in LREE than its counterpart ($[La/Sm]_{pn}$ = 1.06) and shows no Nb/Nb* anomalies on the extended element diagram (fig. 10C), except for samples with higher Th values. Based on the HFSE contents and the variability of Th (= 0.50 ppm), intermediate Nb/Yb tholeiitic gabbro range from N-MORB to E-MORB to BABB (figs. 7A and 7B; Wood, 1980; Cabanis and Lecolle, 1989). A representative sample of this unit shows a primitive $εNd_{(t)}$ value of +7.3, similar to that of the low Nb/Yb tholeiitic gabbro (table 3; fig. 8).

Transitional diorite.—Although most samples of this unit show a tholeiitic trend on a AFM diagram (not shown; Irvine and Baragar, 1971), they straddle the transitional to calc-alkalic fields on a discrimination diagram using immobile trace element systematics (fig. 4C; Barrett and MacLean, 1999; Ross and Bédard, 2009). The transitional diorite shows a wide range in transition elements (that is, V, Cr, Co, Ni; table 1) and

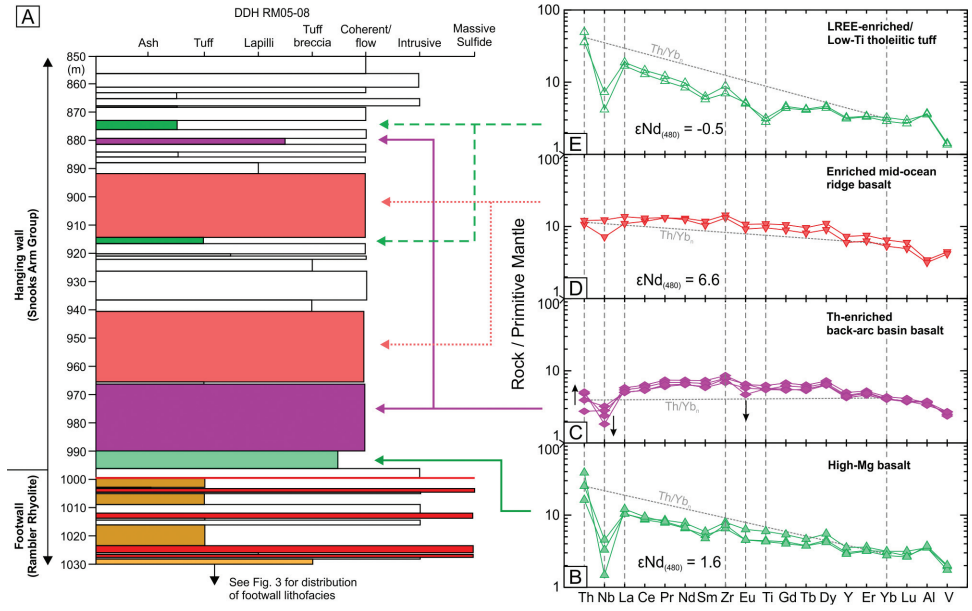

Fig. 9. (A) Stratigraphic column for part of drill hole RM05-08 (Ming South Zone) and (B–E) primitive mantle-normalized extended-element plots, including respective εNd(t) values, for representative samples from the base of the Snooks Arm Group, subdivided based on geochemical criteria (see text for details). Normalizing values are those of Sun and McDonough (1989). Symbols are as in figure 4. Note that the Fe-shale does not occur in this drill hole.

Mg# (table 1). Nonetheless, this unit shows LREE enrichment ($[La/Sm]_{pn}$ = 1.91) with a strong to weak Nb anomaly (Nb/Nb* = 1.22) (fig. 10B). On tectonic setting discrimination diagrams, the rocks of this unit have E-MORB to arc-like signatures (figs. 7A and 7B; Wood, 1980; Cabanis and Lecolle, 1989). A sample of this unit, although showing weak metamorphic alteration, yielded an $\varepsilon Nd_{(t)}$ value of +2.3 (table 3).

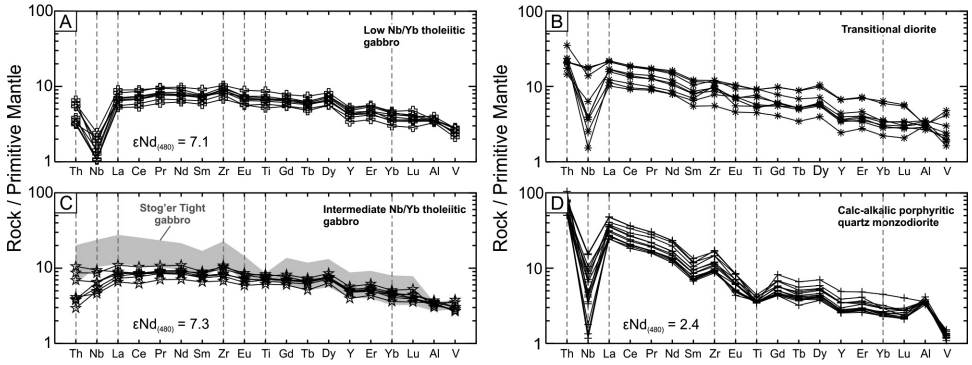

Fig. 10. Primitive mantle-normalized extended-element plots, including respective εNd(t) values, for the intrusive rocks cross-cutting the Ming deposit, subdivided based on geochemical criteria (see text for details). Normalizing values are those of Sun and McDonough (1989). Samples of the 483 Ma Stog'er Tight gabbro are shown (shaded gray) in figure 10C.

Calk-alkalic porphyritic quartz monzodiorite.—The dikes and sills of this unit are unequivocally calk-alkalic ($Zr/Y > 4.5$, $Th/Yb > 0.8$; fig. 4C; Ross and Bédard, 2009) and intermediate in composition (SiO_2 = 58.24 wt. %; Zr/TiO_2 = 160.30; figs. 4A and 4B), which is consistent with the high abundance of quartz. They show low TiO_2 (= 0.801 wt %), Y (= 14.06 ppm), and transition elements such as V (= 106.8 ppm), Cr (= 70.0 ppm), Co (= 18.6 ppm). Interestingly, the contents in Ni are found clustering into two groups, one between 31.1 and 51.0 ppm, another one between 91.0 and 117.6 ppm. Samples with high Ni values were collected near (<2 m) the massive sulfide and the high values are possibly due to cross-cutting remobilized sulfide-rich stringers (Pilote and others, 2017) containing Ni-rich phases, which have been observed in the massive and semi-massive sulfides (Brueckner and others, 2016). The rocks show LREE enrichment ($[La/Yb]_{pn}$ = 11.80) and strong negative Nb (Nb/Nb^* = 0.64) and Ti (Ti/Ti^* = 0.44) and positive Zr (Zr/Zr^* = 3.02) anomalies on the primitive mantle-normalized diagram (fig. 10D). On a Th-Zr-Nb diagram, this unit plots in the arc field (fig. 7A; Wood, 1980). A sample of this unit yielded an $\varepsilon Nd_{(t)}$ value of +2.4 with a significantly lower $^{147}Sm/^{144}Nd$ ratio (= 0.1116) compared to other rocks of the cover sequence, which range between 0.1389 and 0.1901 (table 3; fig. 8).

DISCUSSION

Petrogenesis of the FI- and FII-type Rambler Rhyolite Formation: Evidence of Deep Melting and Possible Link to Adakite

The FI- and FII-type geochemical signatures of the Rambler Rhyolite volcanic and volcaniclastic rocks (Lesher and others, 1986; Hart and others, 2004) are part of a four-fold classification of felsic rocks to discriminate potentially prospective vs. less prospective rocks. While originally created for VMS deposits in Archean belts, it has also proven to be applicable to many Proterozoic and Phanerozoic deposits (Lentz, 1998; Piercey, 2011). Briefly, FI- and FII-type rocks are typically moderately to strongly HREE- and Y-depleted with high $[La/Yb]_{cn}$ and Zr/Y ratios and are interpreted to represent products of deep (≥30 km) to intermediate (10–15 km), low temperature (~650 to ~1000 °C), low degree partial melts where garnet and amphibole are stable in the residue (Lesher and others, 1986; Hart and others, 2004). In contrast, FIII- and FIV-types generally exhibit flat REE patterns ($[La/Yb]_{cn}$ = 0.2–5), higher Y content, significantly more pronounced negative Eu/Eu* anomalies, and considered to have formed at much shallower (<10 km; ~0.75–0.1 GPa) depths at high solidus temperatures (>1000 °C) where plagioclase is stable in the residue. In general, previous workers have suggested that "tholeiitic" rocks of FIII and FIV affinity are more prospective for VMS formation because the melts are generated at higher crustal levels generally reaching the subvolcanic to volcanic environment with their heat intact, and are generally reflective of an environment with an elevated geothermal gradient at shallow levels in the crust (for example, Lesher and others, 1986; Lentz, 1998; Hart and others, 2004; Piercey, 2011). In contrast, "calc-alkalic" FI and FII felsic rocks are interpreted to be less prospective because they form at deeper levels in the crust and reflect colder melts that rarely reach the near surface environment with their heat of fusion intact (for example, Lesher and others, 1986; Lentz, 1998; Hart and others, 2004; Piercey, 2011).

The Rambler Rhyolite formation shows strong depletions in HREE and Y, high $[La/Yb]_{cn}$ and Zr/Y ratios, and lack of negative Eu/Eu* anomalies, suggesting that garnet and/or amphibole were stable in the residue during magma generation (Peacock, 1990) with the melts generated at depths greater than 15 to 30 km since garnet and amphibole preferentially partition HREE (and Y) and MREE, respectively. Moreover, the Rambler Rhyolite units 1.1 and 1.2 have systematically lower $[La/Yb]_{cn}$ and $[Gd/Lu]_{pn}$ ratios relative to unit 1.3 (table 1), which suggests that amphibole was present in the residue during melting during formation of unit 1.3, whereas garnet was

likely present in the residue during the formation of units 1.1 and 1.2. Although this can be readily observed in figure 6B, the overall geochemical and isotopic variations between units 1.1 to 1.3 are nonetheless minimal on the broader scale. The predominantly FI- to FII-type felsic volcanic rocks hosting the Ming VMS deposits are in stark contrast with conventional wisdom for the prospectivity of VMS-related felsic volcanic rocks, despite the deposit having a significant resource of Cu and Au.

Interestingly, many of the geochemical characteristics of FI-type felsic volcanic rocks hosting massive sulfides at Ming are similar to adakite-like rocks that are host to many world-class porphyry Cu-Au(±Mo) deposits (for example, Defant and Kepezhinskas, 2001; Mungall, 2002). Adakites and adakite-like rocks are generally intermediate to felsic (≥56 wt % SiO_2) arc magmas with high Sr/Y (≥20), La/Yb (≥20), Al_2O_3 (≥15 wt %), Ni (≥20 ppm), Cr (≥30 ppm), and low Y (≤18 ppm) and Yb (≤1.9 ppm) (for example, Defant and Drummond, 1990; Drummond and others, 1996; Sajona and Maury, 1998; Castillo, 2006, 2012; Richards and Kerrich, 2007). The high LREE/HREE and Sr/Y ratios found in the Rambler Rhyolite and in adakite-like rocks has been interpreted by Defant and Drummond (1990) to reflect partial melts from young (<25 m.y.) hydrated subducted oceanic crust(±sediments) that undergoes amphibolitization and/or eclogitization (garnet-amphibole-pyroxene-oxide-dominated assemblage) leading to Sr enrichments due to the lack of plagioclase in the residue, and Y and HREE depletion due to amphibole and/or garnet in the residue. The proposed link between slab-melts and adakites was re-evaluated by Richards and Kerrich (2007) and Richards (2011) where these authors favor an alternative model where adakite-like compositions can form in mature oceanic arcs or continental arcs due to: 1) fractionation of or equilibration in primitive basaltic arc magmas with mantle or lower crustal garnet that stall at density barriers in the mantle wedge or within the thickened crust; 2) contamination of primitive basaltic arc magmas with deep crustal garnet amphibolites; and/or 3) fractionation of hornblende±titanite±zircon during primitive basaltic arc magma ascent. Richards and Kerrich (2007) and Richards (2011) have argued that the adakitic signatures and processes above occur in evolved arcs with oceanic and/or continental crust that exceed 20 to 30 km in thickness. In light of the architecture of the Baie Verte oceanic tract, it seems highly unlikely that a crustal thickening model would work for the adakite-like signatures present in the Rambler Rhyolite formation. In particular, the ophiolitic host rocks of the Baie Verte Peninsula are relatively thin (Bédard and others, 1996; Skulski and others, 2015). Even exposed serpentinized ultramafic rocks and the most complete ophiolitic section in the Betts Cove Complex contains no more than 4 to 5 km of coeval sheeted dikes and associated low-Ti and boninitic flows (Dunning and Krogh, 1985; Bédard and others, 1996; Skulski and others, 2015). Correspondingly, a crustal thickening model for forming the adakitic signatures does not seem to be consistent with observed geological thicknesses of units on the peninsula. In addition, regional tectonics models for the Baie Verte oceanic tract argue that this area underwent Cambrian-Ordovician arc rifting and extension with crustal thickening related to obduction only occurring after VMS formation (for example, Bédard and others, 1998; van Staal and others, 2007; Pilote and others, 2017). Finally, the restricted variation of the incompatible elements within and between units 1.1 to 1.3, the absence of negative Eu/Eu* anomalies, and the lack of intermediate volcanic rocks in the Pacquet complex and throughout the peninsula suggests that the felsic volcanic rocks are unlikely the product of magmatic differentiation (for example, crystal fractionation; Shukuno and others, 2006). Correspondingly, the Richards and Kerrich (2007) and Richards (2011) models for the genesis of adakite-like melts, while certainly explaining adakite-like signatures present in porphyry Cu-Au systems, are not consistent with geological and petrological features in the Baie Verte oceanic tract, and cannot explain the garnet and amphibole control on FI-type melt of the Rambler Rhyolite

formation. Thus, it appears that a slab melting model might be more appropriate for explaining the origin of these FI- and FII-type rhyodacite with high $[La/Yb]_{cn}$ ratios and low Y values that are host to the Ming deposit.

Petrogenesis of the Rambler Rhyolite Formation

Given the spatial and temporal coexistence of boninites, low-Ti tholeiites, and felsic volcanic rocks in the Ming area (Piercey and others, 1997; Skulski and others, 2010, 2015), one could postulate that the depleted HFSE and REE nature of the Rambler Rhyolite are or in part are the result of partial melting and/or differentiation of their immediately underlying boninitic/low-Ti tholeiitic crust. The constraints established above on the posited depth (that is, garnet stability zone) at which melting had to occur to generate high $[La/Yb]_{cn}$ and low Y rhyodacite argue against a possible petrogenetic linkage between the Rambler Rhyolite and its underlying boninitic and low-Ti lower crust since the Baie Verte oceanic tract has insufficient crustal thickness, and shows no evidence of crustal thickening during its evolution that could have otherwise involved intracrustal melting (Bédard and others, 1998). In addition to the arguments provided in the previous section of this paper, a slab melt origin for the FI-FII Rambler Rhyolite felsic rocks is also favored because of: 1) the presence of arc signatures in the spatially and temporally associated mafic volcanic rocks suggesting subduction zone magmatism to explain the geochemistry of the Baie Verte oceanic tract at the time of its formation (Piercey and others, 1997; Bédard and others, 1998; Bédard, 1999; Bédard and Escayola, 2010; Skulski and others, 2010, 2015); and 2) the required derivation from deep melting where the source would have contained a garnet-bearing residue to account for the HREE-Y depletions, and enrichments in Sr and other LREE.

To further examine the hypothesis of a slab-derived melt at Ming, REE and HFSE of units 1.1 to 1.3 are tested as a function of potential source compositions and depth of melting (fig. 11), as inferred from minerals present in the residue during melting, using the equilibrium partial melting (modal) equation of Shaw (1970):

$$C^l = C^o/(D_o + F[1 - D_o]) \quad (1)$$

where C^l and C^o are the concentration of an element in the melt and residual solid, respectively, F is the weight fraction of the melt produced, and D_o the bulk partition coefficient of the element in the original solid. Because of the absence of or the inaccessibility to samples representative of the subducted crust, assumptions have to be made on the metamorphic mineral assemblages present at depth during crust anatexis. As such, three residual assemblages with different mineral proportions are used in the calculations, together with mineral-melt partition coefficients typical of adakite-like melting assemblages (Martin, 1987; Sajona and others, 2000; Bourdon and others, 2002), including: 1) garnet amphibolite (53% hornblende; 20% plagioclase; 15% garnet; 10% clinopyroxene; 2% ilmenite); 2) amphibolite (68% hornblende; 25.5% plagioclase; 5% clinopyroxene; 1.5% ilmenite); and 3) eclogite (50% garnet; 50% clinopyroxene) (fig. 11). In both hornblende-rich residual assemblages, the high abundances of residual plagioclase could account for the sub-adakitic Sr values ($\geq$400 ppm). However, given the high mobility of Sr during hydrothermal alteration (for example, Jenner, 1996), it is possible that the Sr abundance is underestimated for units 1.1 to 1.3, even for the least-altered samples, and therefore, Sr cannot be considered as a reliable discriminant. The first inferred source modeled was an N-MORB (Sun and McDonough, 1989), typical of oceanic crust being subducted and often considered the source for slab-derived adakite (for example, Sajona and others, 2000; Bourdon and others, 2002). On modeled curves, the La/Yb ratios of unit 1.3 are intermediate between eclogite and garnet amphibolite ranging between 5 to 30 percent partial

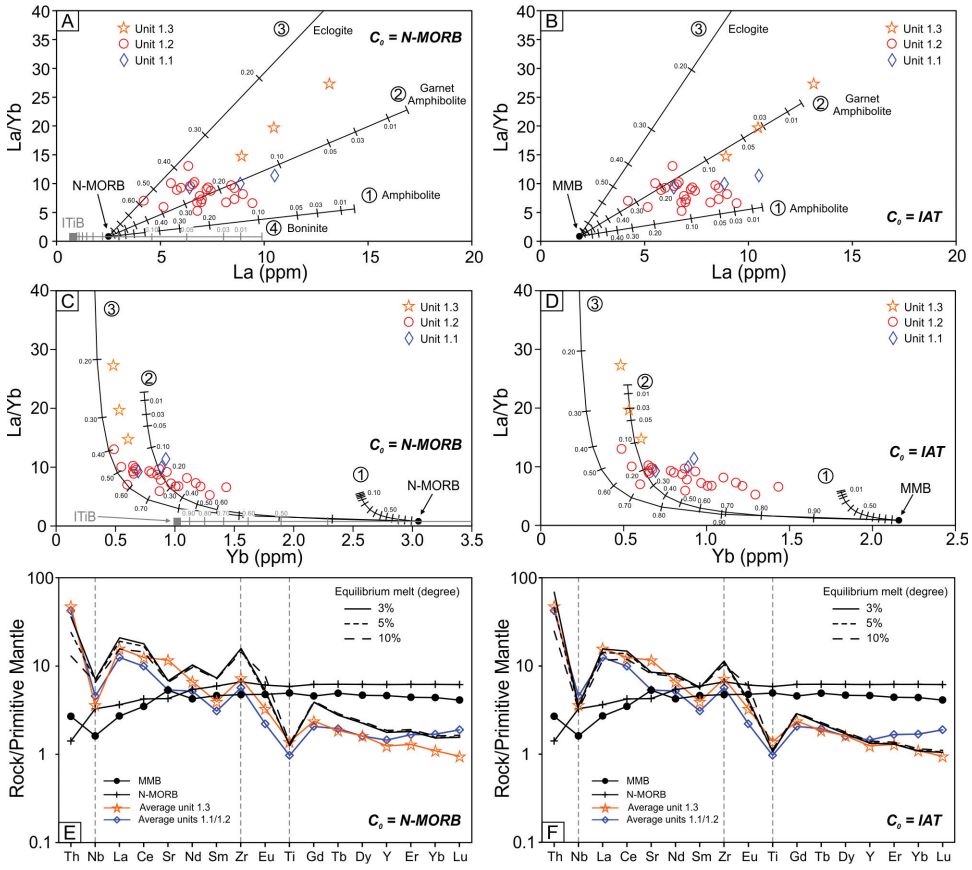

Fig. 11. Modeled resulting compositions from simple batch melting. Evolution of (A) and (B) La/Yb vs. La and (C) and (D) La/Yb vs. Yb obtained by melting an average N-MORB (values from Sun and McDonough, 1989) and island arc tholeiite (Mount Misery Formation; MMB; values from Bédard, 1999) considering three different melting residues, including: (1) amphibolite (68% hornblende, 25.5% plagioclase, 5% clinopyroxene, 1.5% ilmenite), (2) garnet amphibolite (53% hornblende, 20% plagioclase, 15% garnet, 10% clinopyroxene, 2% ilmenite), and (3) eclogite (50% garnet, 50% clinopyroxene). Residues are adjusted from Martin (1987). Ticks on curves are percentages of partial melting. (E) and (F) Theoretical primitive mantle-normalized extended-element plots obtained by models of 3%, 5%, and 10% partial melting of an average N-MORB and island arc tholeiite (both shown), using the garnet amphibolite residue (1). Also shown for comparison purposes are average values for units 1.1/1.2 and 1.3. Normalizing values are those of Sun and McDonough (1989).

melting, whereas unit 1.1/1.2 produces a horizontal array, at constant La/Yb, intersecting the same modeled curves as unit 1.3 at degrees of melting ranging between 30 to 40 percent (figs. 11A and 11C). In figure 11E, we represent melt models for a broader suite of trace elements, including the residual garnet amphibolite at 3 percent, 5 percent, and 10 percent partial melt. Although the model generally recreates most natural values for Ti and Y at low degrees of partial melts (≤10%), significant differences exist for most trace elements (fig. 11E). With the exception of Th, using an N-MORB source, most elements are overestimated by our model and therefore N-MORB does not appear to be a suitable source for melting.

Given the overestimation using a MORB source, it requires a source with overall lower HFSE, REE, and higher Th abundances. These requirements can be accommodated by melting instead a slightly more evolved source with the composition of an

island arc tholeiite. The nearby Mount Misery Formation, which has been geochemically characterized by Bédard (1999), is dominated by island arc tholeiitic flows of Cambrian age and thus, represents a reasonable analogue for our required modeled source composition. We applied the same model above but using the average values of least-altered (that is, low LOI, Na_2O = 2–5 wt %) islands arc tholeiites of the surrounding Mount Misery Formation (Bédard, 1999). In this case, the trace element signatures from unit 1.3 can be explained by 1 to 10 percent partial melts of garnet amphibolite curves, whereas samples of units 1.1 and 1.2 can be explained by roughly 20 to 30 percent partial melting (figs. 11B and 11D). On an extended-element plot (fig. 11F), with the exception of the modeled MREE that show slightly higher values, melting an island arc tholeiitic source provides a better fit to the Rambler Rhyolite samples, and lower degrees of partial melting than N-MORB sources.

There are slight variations in the model results. In particular, the listric-shaped trace element patterns and lower LREE contents of units 1.1 and 1.2 relative to the linear slopes of unit 1.3, are suggestive of a greater amphibole control on their melt (figs. 7A and 7B, 11E and 11F; table 1) since amphibole preferentially partitions MREE and HREE (that is, $D_{Dy}D_{Yb}D_{La}$). Accordingly, the variations in array shown in figures 11A to 11D between units 1.1 to 1.3 likely reflects the heterogeneity of the garnet-amphibole-clinopyroxene proportions during melting of an island arc tholeiitic source. The results above have attempted to quantify the specific degree of partial melting involved during slab anatexis, it is often difficult to model in ancient sequences. Nevertheless, the results presented herein and the ≤30 percent slab partial melt values are similar to models of adakite formation under hornblende eclogitic conditions (Tsuchiya and Kanisawa, 1994), and overlaps the optimum conditions for siliceous melt segregation from a garnet- and hornblende-bearing basaltic protolith (Rapp, 1995).

Rising felsic magmas will likely interact with the mantle wedge and/or overriding crust and this often results in Ni-Cr enrichments in the adakite-like felsic rocks (Frey and others, 1978; Kay, 1978; Sen and Dunn, 1994; Drummond and others, 1996; Martin, 1999; Smithies, 2000). Nickel and Cr typically partition into ferromagnesian minerals (for example, olivine, orthopyroxene, and hornblende); however, Kelemen (1995) suggested that when slab melts interact with the mantle wedge they can dissolve olivine and/or react with the wall rock resulting in Ni-Cr enrichments in the felsic rocks. The high average Ni and Cr (adakitic) values in units 1.1 to 1.3 at Ming (table 1) relative to normal intermediate to felsic volcanic rocks from island arcs (~9 ppm Ni, ~21 ppm Cr; Drummond and others, 1996) provide additional support for potential slab melting and melt-mantle interaction; however, further work is needed to test these processes more fully.

An alternative process to the generation of slab-derived melt in juvenile (<10 m.y.) and thin (<15 km) oceanic arc environments was proposed by Macpherson and others (2006) in which ascending basaltic arc magma derived from slab-dehydration could pond at thermal or rheological boundaries at or below the Moho or within the mantle (≥30 km; that is, garnet stability field) and undergo fractional crystallization of a garnet-bearing residual assemblage to produce adakite-like magmas. Although we agree with the possibility of thermal and/or rheological boundaries existing beneath some thin arcs (for example, Stratford and Stern, 2004), it is very difficult to prove their existence in ancient orogenic belts, such as the Appalachians, given the absence of preserved sections of the deeper mantle. Despite the latter, the restricted geochemical variations within the felsic units at Ming and the absence of intermediate rocks do not support crystal fractionation as a viable magmatic process to generate the FI(±FII)-type rhyodacite at Ming and hence, argue against any types of protracted magma ponding below the crust.

The slab melt model also potentially explains rocks that precede the formation of the Rambler Rhyolite and the isotopic systematics of the BVOT. Bédard (1999)

estimated that the Betts Cove boninitic rocks, which are similar to those underlying the Rambler Rhyolite, had a small (<0.25%) contribution derived from the subducted slab and was identified as a mixture of hydrous phases, sediments, and/or slab-melts (that is, adakite). Moreover, slab derived melting has been advocated for the genesis of boninites, globally (Pearce and others, 1992; Pearce and Parkinson, 1993). It is a difficult problem, however, to discriminate between the relative involvements for each component, if all are contributing in the generation of boninite (for example, Bédard, 1999). An input of material such as Laurentian-derived sediments, which can be isotopically evolved ($\varepsilon Nd_{(560)} = -7.7$ from a sample of psammite; van Staal and others, 2013), could explain the relatively evolved $\varepsilon Nd_{(t)}$ values in the boninites (+0.7 to +3.9) from Betts Cove, which would have been influenced by slab melts, as opposed to their coeval island arc tholeiites (+5.2 to +8.0), which were likely derived predominantly from the mantle wedge (fig. 8; Swinden and others, 1997; Bédard, 1999). For the Rambler Rhyolite formation, a crustal contribution is unambiguous as it exhibits relatively low $\varepsilon Nd_{(t)}$ values (−2.5 to −1.1). Moreover, Skulski and others (2015) reported the inheritance of zircons of 1.1 Ga and 2.5 Ga from a sample collected near the historical Rambler mine (fig. 2). It is, however, difficult to assert with certainty this crustal input to result from a direct bulk sediment influx within the slab-derived melts or by high level contamination within the arc crust. The lack of any field evidence for an underlying old and evolved crust (for example, Laurentian margin or Dashwoods) beneath the Baie Verte oceanic tract favors derivation of continental material via slab melting. The low $\varepsilon Nd_{(t)}$ values in the Rambler Rhyolite together with the inherited zircon patterns are consistent with Laurentian-derived sediments reported by van Staal and others (2013).

To summarize, we propose that the units 1.1 to 1.3 hosting the Ming VMS deposit result from low (≤10%; unit 1.3) to moderate (~30%; units 1.2/1.3) degree of partial melting of a sediment-rich/hydrated subducted oceanic crust composed of island arc tholeiites undergoing amphibolite to eclogite metamorphism at depths exceeding 30 km. Melting with a garnet-amphibole-rich residual solid produced a high $[La/Yb]_{cn}$, Sr/Y, Zr/Y, and low Y, FI- to FII-type rhyodacite with geochemical characteristics that resemble greatly adakites found in many active margins (Defant and Drummond, 1990).

Zircon Saturation Temperature

Despite the multiple attempts made during the course of this study to extract zircons from a quartz-bearing felsic tuff located immediately below the massive sulfide lens of the 1807 Zone, no grains were yielded. The lack of zircons in the sample collected may be due to: 1) the undersaturation of Zr in the melt (Hanchar and Watson, 2003); and/or 2) rapid cooling inhibiting nucleation of zircons and subsequent growth. Assuming low temperatures (~650–700 °C) for melt generation at Ming, only a small concentration (~50 ppm) of Zr is required to reach zircon saturation in the felsic melt, irrespective of the alkalinity of the melt (Watson and Harrison, 1983). Except for rocks of unit 1.3, where concentrations reach up to 90 ppm Zr, all samples of units 1.1 and 1.2 range between 40 and 70 ppm Zr, which are near or above the saturation curve of Watson and Harrison (1983). Skulski and others (2010, 2015) extracted a small number of zircons and reported an unpublished U-Pb (SHRIMP) crystallization age of 487±4 Ma with Grenvillian inheritance (1.0–2.4 Ga), southwest of the Rambler deposit (sample location in fig. 2). For the sake of the discussion, assuming that the sample collected at the Ming deposit was in fact saturated, but rapid cooling inhibited nucleation of zircon grains, saturation thermometry can be calculated using the following solubility model

$$\ln D_{Zr}^{zircon/melt} = (-3.80 - [0.85(M - 1)]) + 12900/T \qquad (2)$$

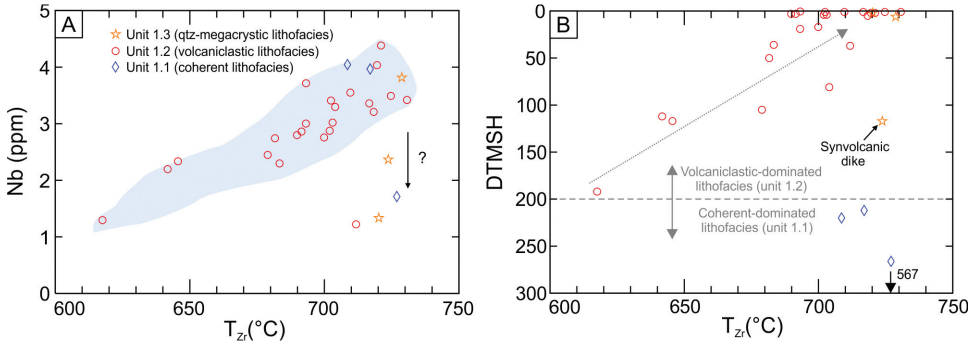

Fig. 12. (A) Nb vs. zircon saturation temperature (T_{Zr}) and (B) relative (depth) to the massive sulfide horizon (DTMSH) vs. T_{Zr} where 0 m represents the ore horizon. Zircon saturation temperature calculations were done exclusively on the least-altered felsic rocks of the Rambler Rhyolite formation. See text for details.

of Watson and Harrison (1983) and adapted by Hanchar and Watson (2003), where $D_{Zr}^{zircon/melt}$ is the concentration ratio of Zr in zircon and in the melt, M is the cation ratio or alumina saturation factor for the rock $(Na+K+2 \cdot Ca)/(Al \cdot Si)$, and T is temperature in Kelvin. Results of these calculations are shown in figure 12 with zircon saturation temperature (T_{Zr}) ranging from 615 °C to 730 °C, which have the same temperature ranges as have been inferred for the genesis of FI-type felsic magmas, globally (Hart and others, 2004; P-T conditions and source compositions based on experimental work by Spulber and Rutherford, 1983; Beard and Lofgren, 1991; Wyllie and Wolf, 1993; Rapp, 1995). When Nb (also considered as a proxy for HFSE) is plotted against T_{Zr}, a positive covariation exists between the two variables, with minor exceptions (fig. 12A). Samples from units 1.1 and 1.3 are restricted to the higher spectrum of the temperature range, whereas unit 1.2 shows a wide range of temperatures. Except for a few outliers, a positive relationship similar to this is observed at the Wolverine VMS deposit, Yukon, and was interpreted by Piercey and others (2008) as the result of higher temperature at the melting source accommodating greater amounts of REE and HFSE in the resulting melt. The latter also implies that higher degree of partial melting would be generated for samples with high T_{Zr} and Nb values (Hanchar and Watson, 2003; Piercey and others, 2008 and references therein).

By evaluating the relationship between T_{Zr} and the stratigraphic position the samples were collected relative to the massive sulfide horizon (DTMSH; fig. 12B), an abrupt temperature change exists between unit 1.1 (that is, the deepest unit of the Ming deposit) and the base of unit 1.2, which shows a systematic increase of temperature with decreasing depth (or DTMSH), reaching a maxima (together with unit 1.3) near or at the contact with the mineralized horizon. This implies that the initial eruption of the volcaniclastic lithofacies (unit 1.2) during or after subsidence of the domal structure (unit 1.1) and development of the nested basin (Pilote and others, 2017) was formed by low temperature melts (~620–650 °C; low partial melting) and progressively became hotter (~700–730 °C; greater partial melting) until onset of the VMS-forming hydrothermal circulation system. Accordingly, this rising temperature of melts (and probably concomitant rising of the geothermal gradient) became the driving mechanism for hydrothermal circulation (for example, Franklin and others, 2005) and the formation of the Ming VMS deposit.

Petrogenesis of the Cover Sequence and Relationships to Post-mineralization Dikes

The base of the cover sequence (lower 200 m) consists of multiple flows and epiclastic to volcaniclastic accumulations of distinct geochemical and isotopic

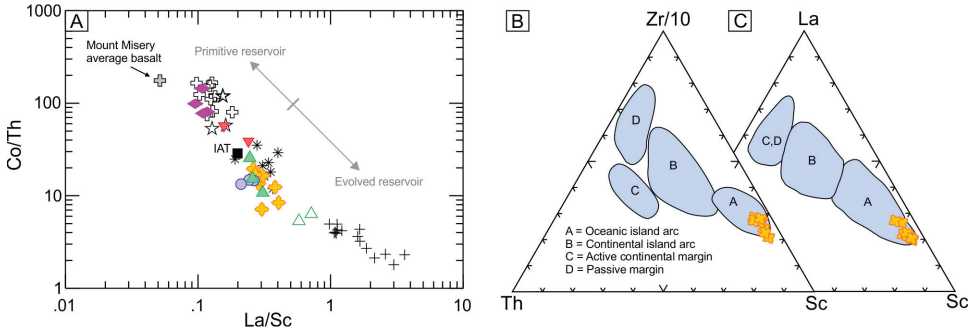

Fig. 13. Source plots for the Fe-shale and other rocks of the Snooks Arm Group. (A) Co/Th vs. La/Sc plot. The average composition of the basalt from the Mount Misery Formation is also shown. (B) and (C) Zr (La)-Th-Sc discrimination diagrams of Bhathia and Crook (1986). Symbols are as in figure 4.

affinities. Some of the mafic to intermediate sills and dikes that intrude the Ming deposit share geochemical signatures with the extrusive rocks that suggest comagmatic relationships. As such, based on their magmatic and tectonic affinities (figs. 4C and 7), incompatible element ratios (table 1), and trace element patterns (figs. 6, 9, and 10), three intrusive-extrusive assemblages are discriminated, including: 1) low Nb/Yb tholeiitic gabbro and Th-enriched back-arc basin basalt; 2) intermediate Nb/Yb tholeiitic gabbro and enriched mid-ocean ridge basalt; and 3) transitional diorite and sulfide-rich mafic breccia and high-Mg basalt. Because the transitional diorite shows evidence of differentiation (La = 8.4–15.1 ppm; Mg# ~18–53) at near constant La/Sm (~3), it overlaps both the high-Mg basalt (Mg# ~45–53) and sulfide-rich mafic breccia (Mg# ~19–36). Mafic volcanic rocks of the Silurian Micmac Lake and Cape St. John groups (fig. 1) are dominantly alkalic (high Th, Nb, Ba; DeGrace and others, 1976; Skulski and others, 2017) and therefore are unlikely to be the extrusive equivalent to the mafic intrusive rocks at Ming. Moreover, the $483\ ^{+3}/_{-2}$ Ma Stog'er Tight gabbro (Ramezani and others, 2000), located north of the Scrape Thrust (fig. 2), is geochemically similar to the intermediate Nb/Yb tholeiitic gabbro (fig. 10C), which further substantiates the consanguineous relationship between the mafic dikes and the Snooks Arm Group. In the case of the calc-alkalic porphyritic quartz monzodiorite, its Th- and LREE-enrichment is beyond any other units discussed here and therefore is likely unrelated to rocks from the base of the cover sequence. These calc-alkalic rocks, nonetheless, form only a minor proportion of all the intrusive units at the Ming deposit (Pilote and others, 2017).

On an extended element plot, the Fe-shale shares similar patterns with its nearby high-Mg basalt and sulfide-rich mafic breccia (figs. 6C and 6D), suggesting that the sediments are likely derived from these proximal surrounding units. Inter-element ratios such as Co/Th and La/Sc can be used to determine the bulk composition of the source (fig. 13A) as they are generally immune to secondary processes (for example, metamorphism; Condie and Wronkiewicz, 1990). The results show congruent ratios to the underlying and overlying units (table 1) and to the average oceanic island-arc tholeiitic basalts of Kelemen and others (2003). On Th-Zr-Sc and Th-La-Sc discrimination diagrams (figs. 13B and 13C) of Bhatia and Crook (1986), samples of the shale plot in the oceanic island-arc field, consistent with the juvenile arc signature of the adjacent rocks. The Fe-shale, however, exhibits significantly higher $\varepsilon Nd_{(t)}$ (+3.1 to +5.5) than the other two units (−0.5 to +1.6), which indicates that the high-Mg basalts and sulfide-rich mafic breccia are not the exclusive sources and therefore, requires a more juvenile input during deposition.

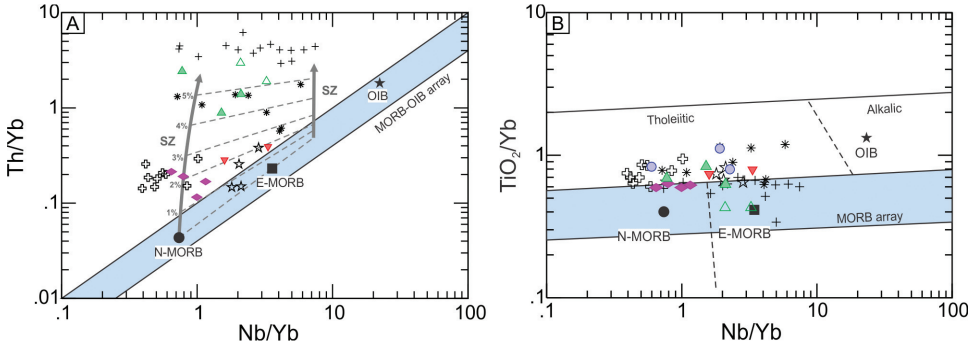

Fig. 14. Magmatic differentiation of variably incompatible elements within and between mafic units of the Snooks Arm Group. (A) Th/Yb vs. Nb/Yb plot with vectors indicating subduction component (in %) addition and assimilation-fractional crystallization (AFC; Depaolo, 1981) from Pearce (2008). (B) TiO_2/Yb vs. Nb/Yb plot. Compositional fields of modern MORB-OIB array and volcanic array are from Pearce and Peate (1995) and Pearce (2008). Average N-MORB, E-MORB, and OIB are from Sun and McDonough (1989). Symbols are as in figure 4.

The sulfide-rich mafic breccia, Fe-shale, high-Mg basalt, LREE-enriched/low-Ti tholeiitic tuff, and transitional diorite all show enrichment in Th and depletion in HFSE (Nb, Y) and HREE, signatures typically associated with arc-derived magmas (Tatsumi, 1989), which is supported by their inter-element ratios (figs. 6 and 7). In all of these rocks, an evolved crustal contribution at the source and/or during magma ascent is evidenced by their $\varepsilon Nd_{(t)}$ values near the chondritic uniform reservoir ($\varepsilon Nd = 0$) (table 3; fig. 8). On primitive mantle-normalized plots (figs. 6, 9, and 10), their patterns compare to island-arc tholeiites from other ancient systems (Jenner, 1996; Piercey, 2010). Above the high-Mg basalts and intercalated with the LREE-enriched/low-Ti tholeiitic tuffs are multiple successions of mafic flows from depleted mantle sources ($\varepsilon Nd_{(t)} = +6.6$ to $+7.3$), including Th-enriched back-arc basin basalts and enriched mid-ocean ridge basalt (fig. 9). This transition indicates variability in the sources and processes, and the dynamism in the Cambro-Ordovician subduction complex (for example, Pearce and Peate, 1995).

Incompatible element ratios such as Th/Yb and Nb/Yb (fig. 14A) are used to assess the mantle composition (for example, depleted vs fertile), the potential involvement of slab-derived components (for example, melts, fluids), and/or degree of partial melt controlling the derived melt composition (Pearce and others, 1995; Pearce and Peate, 1995; Peate and Pearce, 1998; Pearce, 2008). For basaltic melts of oceanic realms where the mantle source has not been affected by the addition of subduction-related material, they should plot along the MORB-OIB array on a Th/Yb vs Nb/Yb plot (fig. 14A), where Nb/Yb reflects the incompatible element enrichment of the mantle source. Dynamic (or continuous) melting (Langmuir and others, 1977) and/or melting of heterogeneous mantle compositions (for example, E- and N-MORB) will displace the resulting melt parallel to this array since Th and Nb behave similarly during melting (that is, both are highly incompatible elements; Pearce and others, 1995). Because Th is highly soluble in fluids derived from the dehydration of the subducted slab (as opposed to Yb), a Th-enrichment in the mantle wedge will result in melts with higher Th/Yb ratios. Other types of crustal contribution (slab-derived melt, subducted sediments, overriding crustal contamination) can also influence Th/Yb ratios, thus shifting samples above the MORB-OIB array. With the exception of two samples from the intermediate Nb/Yb tholeiitic gabbro, all units above the massive sulfides at Ming plot above the MORB-OIB array (fig. 14A), indicating a crustal or slab

input within a subduction setting. Moreover, most units show a horizontal spread. One possible explanation for this wide range in Nb/Yb at near constant Th/Yb includes the addition of crustal material into a heterogeneous mantle wedge undergoing progressive melting (Pearce and others, 1995; Peate and others, 1997). The two samples from the intermediate Nb/Yb tholeiitic gabbro that plot inside the array show, however, a compositional trend that can be traced from near a primitive mantle value, increase to higher Th/Yb at constant Nb/Yb, and finally vary parallel to and slightly above the MORB-OIB array (fig. 14A). Note that, the extrusive equivalent of the gabbro, the enriched mid-ocean ridge basalt, shows a similar pattern (fig. 14A). Interestingly, the first enriched mid-ocean ridge basalt that reaches surface in the Ming area (fig. 9) plots higher on the slope (fig. 14A), whereas the stratigraphically higher flow plots with lower ratios (samples from this unit collected beyond the 200 m also show the same systematic decrease in Th and Nb against Yb). This magmatic evolution from high to low Th and Nb against Yb, which is likely mirrored by the comagmatic gabbroic dikes, is best explained by the increase of degree of melting of an enriched mantle source (Pearce and Peate, 1995; Peate and Pearce, 1998; Pearce, 2008), possibly pre-enriched by Th-rich fluids derived by the subducted slab and/or Th-rich melts.

The depth and changes in degree of partial melting can also be evaluated using the TiO_2/Yb vs. Nb/Yb projection of Pearce (2008). This plot is meant as a proxy for melting depth and is typically used for samples unaffected by crustal contamination ($Th/Nb < 0.2$) and/or oxide fractionation ($Ti/Ti^* \approx 1$), that is, samples that plot inside the MORB-OIB array in the Th/Yb vs. Nb/Yb diagram (fig. 14B). Ocean island basalts (OIB) have high TiO_2/Yb and Nb/Yb ratios because of the presence of residual garnets and low degree of partial melting. Any MORB affected by an OIB (for example, plume-ridge interaction) or OIB-like rocks should display a diagonal or positive trend. Pearce (2008) also demonstrated that variations in partial melting should be reflected by diagonal trends, although less pronounced at pressures ≤2 GPa. Whereas almost all samples of the cover sequence plot outside the MORB-OIB array (fig. 14A), they show systematically high TiO_2/Yb ratios regardless of Nb/Yb (fig. 14B) without positive correlations leading to the OIB field. This argues against the presence of an OIB source in the mantle wedge and deep level melting (low degree of partial melt), which is supported by the lack of alkalic end member magmas in the area, and it is consistent with the conclusions from Bédard (1999) for the lower stratigraphic successions. One viable explanation for this Ti-enrichment is the metasomatism of the mantle wedge by slab-melt during the building of the Rambler Rhyolite formation. This early hybridization process from siliceous melts is commonly thought to form zones enriched in Ti-hosting minerals, such as amphiboles and/or titanium-bearing oxides in the peridotite, which become unstable during subsequent melting (for example, Arculus and Powell, 1986; Ryerson and Watson, 1987; Kepezhinskas and others, 1996; Sajona and others, 1996, 2000). The same process of hybridization has been proposed by many workers as a prerequisite for the formation of high-Mg basalts and andesites in adakite-endowed regions (Kay, 1978; Saunders and others, 1987; Tatsumi, 2006) and could be responsible for the high Mg values in the high-Mg basalt at the base of the Snooks Arm Group.

Implications for the Evolution of the Baie Verte Oceanic Tract

The evolution of the Baie Verte oceanic tract (for example, Bédard and others, 1998; Bédard, 1999; van Staal and others, 2013) is interpreted to reflect sea-floor spreading in a peri-continental supra-subduction zone based on the petrological assemblages present in the Betts Cove ophiolite and regional equivalents, which are commonly restricted to fore-arc environments (Stern and Bloomer, 1992; Bédard and others, 1998; Bédard, 1999; Stern, 2004). Despite remaining uncertainties on the timing of events prior to and during the obduction of the Baie Verte oceanic tract, the

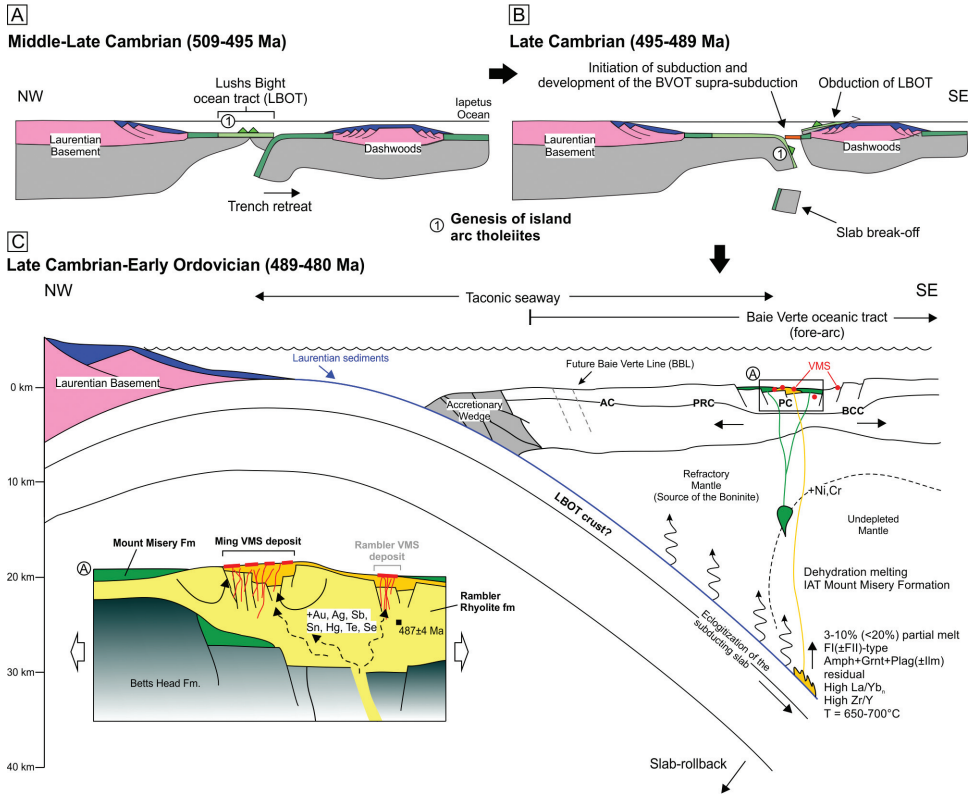

Fig. 15. Schematic partial geodynamic and tectonic evolution of the Taconic seaway between the Middle Cambrian and Early Ordovician (*ca.* 510–480 Ma). These figures are based on the work of Bédard and others (1998), Bédard (1999), van Staal and Barr (2012), van Staal and others (2013), and Castonguay and others (2014). They do not take into account the initial opening nor the final closing stages of the seaway (see aforementioned references for more details). The model presented here shows (A) the development of the Lushs Bight supra-subduction crust (LBOT) onto which island arc tholeiites were constructed, (B) then the eastward emplacement of the LBOT onto Dashwoods and nucleation of subduction which led to (C) the development of the extensional Baie Verte supra-subduction zone. The felsic FII- and FI-type host rocks of the Ming deposit result from low-temperature (650–700 °C) slab-derived partial melting (~3–10%) accommodating significant amounts of Au and other magmatophile elements. The subduction of remnant arc-like rocks (IAT) from the Lushs Bight oceanic tract that experienced amphibolite facies metamorphism and dehydration could explain the amount of hornblende and garnet required to generate the FI-(±FII-)type felsic magmas. Abbreviations: AC = Advocate Complex, BCC = Betts Cove Complex, PC = Pacquet complex, PRC = Pointe Rousse Complex.

most recent tectonic models (van Staal and others, 2013; Castonguay and others, 2014) suggests the following: 1) west-vergent (present coordinates) subduction at *ca.* 510 to 505 Ma of oceanic crust (Taconic seaway) that separated Laurentia from the Dashwoods block, forming the supra-subduction zone-related Lushs Bight oceanic tract; 2) incomplete closure of the Taconic seaway led to the eastward obduction of part of the Lushs Bight oceanic tract onto the Dashwoods block at *ca.* 495 Ma; 3) subsequent nucleation of an east-vergent subduction of the remnant Lushs Bight oceanic tract, outboard of the Dashwoods block led to the development of the supra-subduction Baie Verte oceanic tract at *ca.* 495 to 490 Ma (fig. 15); and 4) a westward obduction of the Baie Verte oceanic tract on the Laurentian margin at *ca.* 479 Ma and shortly after the establishment of a back-arc spreading system generating tholeiitic and calc-alkalic volcanism in the cover sequence (that is, Snooks Arm Group) (Bédard and others,

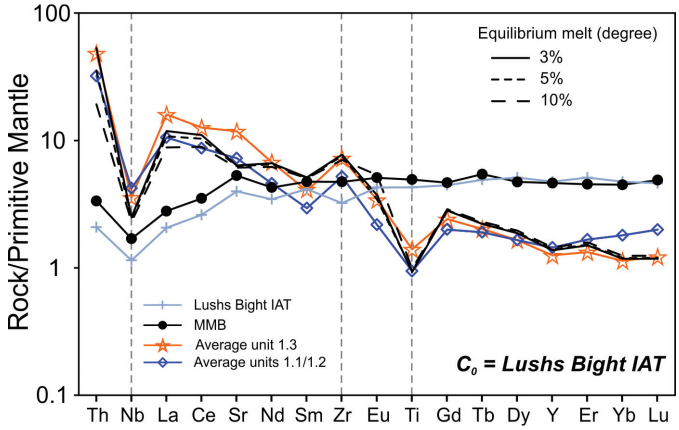

Fig. 16. Modeled resulting compositions from simple batch melting of the average Lushs Bight island arc tholeiites from Kean and others (1995). All units here are recalculated with volatile-free at a total of 100 wt % in order to be consistent with Kean and others (1995) data. The modeled compositions use the same parameters as in figure 11. Normalizing values are those of Sun and McDonough (1989).

1998; Cousineau and Bédard, 2000; Kessler and Bédard, 2000; Skulski and others, 2010). Petrogenetic modeling of the Rambler Rhyolite, and petrogenetic and stratigraphic relationships in cover sequence rocks, provides critical tests and implications for the model outlined above. Firstly, the modeling of the Rambler Rhyolite suggests that the source region for the rhyolites must have had an island arc tholeiite signature, but also its high $[La/Yb]_{pn}$ ratio requires that the source be generated at depth with residual garnet and amphibole. At the time of formation there is ample evidence stratigraphically to suggest that the fore-arc was under extension and the Rambler Rhyolites were forming in volcanic/volcaniclastic basins that were extending with no evidence for crustal thickening (Pilote and others, 2017). Correspondingly, this requires a source that maintained the depth of melting where garnet and amphibole were stable with partial melting of an island arc tholeiite. These requirements can be accommodated in light of recent models for closure of the Taconic Seaway. As mentioned above, the nucleation of an east-vergent subduction may have entrained crust at depth of the Lushs Bight oceanic tract to become the (fluid and melt) source for the Baie Verte oceanic tract. To test this, the average composition of island arc tholeiites from the uppermost section of the Lushs Bight ophiolite (Kean and others, 1995) are plotted in figure 16 and their modeled composition after 10 percent partial melting from a garnet amphibolite are calculated applying the same method above. The resulted compositions are not only consistent with units 1.1 and 1.1/1.2 but show better fits than the Mount Misery Formation. The implication here is that the subduction of an island arc tholeiite necessitates the pre-existence of a subduction complex in the reverse direction (fig. 15), hence a polarity flip, which corroborates with the tectonic reconstructions of Zagorevski and van Staal (2011), van Staal and Barr (2012), van Staal and others (2013), and Castonguay and others (2014).

The association between boninite and adakite in the Pacquet complex is not uncommon. Their coexistence has been reported in ancient (Polat and Kerrich, 2001, 2004; Ishiwatari and others, 2006; Niu and others, 2006) and modern day (Falloon and others, 2008; Li and others, 2013) oceanic arc systems. Whereas boninite can form in peri-continental rifting (Piercey and others, 2001), in juvenile oceanic settings such as the Izu-Bonin-Mariana-Tonga trench and the Baie Verte oceanic tract, most boninites (and associated adakites) are generally accepted to form shortly after subduction

initiation (Pearce and others, 1992; Stern, 2004; Ishizuka and others, 2006, 2011; Reagan and others, 2010). The resulting extension of the overriding crust from the sinking slab enables ascending asthenospheric mass transfer to undergo significant partial melting (~20–30%), and hence produce N-MORB melts (with lherzolitic residual). Subsequent melting of this refractory mantle would form boninite (with harzburgitic residual). If a pre-depletion event occurred prior to subduction, boninite melts would form first and predominate the base of the newly formed crust. Based on the geology and the nature of the Betts Cove Complex (Bédard and others, 1996; Skulski and others, 2015), Bédard (1999) has favored the latter for its formation. Shortly after (<5 m.y.), the juxtaposition of hot mantle with hydrated, young, and hot oceanic crust undergoing amphibolite to eclogite metamorphism allows the subducted slab (and its overlying sediments) to partially melt (at ~650–750 °C), leaving a garnet-amphibole-rich residua. The melt interacts with the mantle wedge (high Ni, Cr) to finally extrude as a highly fractionated (or adakite/FI-type) felsic rock, with characteristics that are shared with the Rambler Rhyolite formation (fig. 15).

The Snooks Arm Group was interpreted by previous work as an arc (Snooks Arm arc) developed on and during the obduction of the Baie Verte ophiolite (Bédard and others, 1998). The sediment at its base is viewed as the disconformity that marks a change in the geodynamics of the Taconic Seaway, that is, from fore-arc spreading to a compressional regime leading to the obduction of the ophiolite. Although the time gap between the formation of the Rambler Rhyolite (487 ± 4 Ma)/Mount Misery formations and the first pulse of volcanism overlying the shale is poorly constrained (Skulski and others, 2010), the presence of high-level tholeiitic basalts with primitive $\varepsilon Nd_{(t)}$ (+6.6 to +7.3) values indicates that extension had to continue in order to accommodate upwelling of mantle. However, Skulski and others (2010) reported a polymictic conglomerate that overlies the Advocate Complex in the western part of the peninsula (fig. 1) with lithologies and mineralogy suggestive of exhumation from obduction. Nonetheless, it is possible that localized spreading from transtensional strike-slip movements occurred as some studies suggest a non-orthogonal plate convergence during closure of the Taconic seaway (Cawood and Suhr, 1992; Dewey, 2002). Regardless of the plate dynamics, the interstratification of arc- to non-arc-related rocks with variable Nd isotopic signatures at the base of the Snooks Arm Group reflects the heterogeneity of the mantle, which is a common trait in many evolving arc systems (for example, Peate and Pearce, 1998). As subduction continued after the volcanic hiatus (deposition of the Fe-shale), slab-dehydration induced partial melting of the HFSE-enriched ($TiO_2/Yb > 5$) overlying mantle wedge, which led to the formation of the high-Mg basalts (and its intrusive equivalent) and LREE-enriched/low-Ti island arc tholeiite. Thinning of the refractory harzburgitic mantle (due to protracted spreading of the overriding crust) allowed mass transfer of N-MORB to E-MORB mantle material near the base of the crust. More geochronological constraints are needed in order to refine the timing of these pre- to syn-accretionary events.

Implications of High LREE/HREE Felsic Volcanic Rocks on the Nature and Style of Mineralization at the Ming Deposit

The lithogeochemistry of VMS-related felsic volcanic rocks is well documented (for example, Lesher and others, 1986; Lentz, 1998; Yang and Scott, 2003; Hart and others, 2004; Gaboury and Pearson, 2008; Piercey, 2010, 2011). There has been considerable research into the petrogenetic evolution of magmas and their tectonic settings and how they influence deposit localization and genesis. Moreover, some authors have argued that magmas may directly contribute magmatophile elements (Au, Ag, Te, Se, Bi, Sn) to hydrothermal fluids that form VMS at or near the seafloor (for example, Urabe and others, 1983; Urabe, 1987; Lydon, 1996; Sillitoe and others, 1996; Hannington and others, 1999, 2005; Yang and Scott, 2003; Brueckner and

others, 2014, 2016). The importance of a direct magmatic input in the Ming deposit has been documented mineralogically (Brueckner and others, 2014, 2016; Pilote and others, 2016). The contribution of magmatic fluids in modern deposits has been established in many cases (for example, Sillitoe and others, 1996), but in the ancient record, the results are much less concrete and are often by inference (Lydon, 1996). Moreover, linkages between the magmatic evolution of a felsic magma and the precious metal enrichment of VMS deposits is in its infancy (for example, Urabe, 1987; Urabe and others, 1995; Lydon, 1996; Yang and Scott, 2002, 2003). Recently, workers globally have illustrated that many Au-Ag-bearing deposits are hosted by strongly fractionated FI-type (+/− FII-type) felsic rocks (for example, Bousquet mining district - Mercier-Langevin and others, 2007; Eagle-Telbel, Géant Dormant, and Duvan deposits - Tremblay and others, 1996; Gaboury and Daigneault, 1999; Gauthier and others, 2003). These authors, however, have not linked the petrogenetic histories of these magmas, nor their tectonic histories to the precious metal endowment present in the associated deposits. The results herein illustrate that it is possible that FI-type (+/− some FII-type) magmas may be associated with slab melting, and while previous studies have considered them less prospective (for example, Lesher and others, 1986; Lentz, 1998; Hart and others, 2004; Piercey, 2011), these may be attractive targets for Au-Ag-rich VMS mineralization.

The question arises as to why do felsic rocks associated with slab melting lead to Au-Ag-rich VMS mineralization. A potential solution to this comes from previous work by Mungall (2002), who presented a geochemical model where partial melting of subducted ocean crust generates a highly fractionated melt, such as the Rambler Rhyolite (FI-/FII-types), that is highly oxidized. The fO_2 should be significantly greater in slab-derived melts than normal arc melts due to high Fe^{3+} content from sea-floor alteration and their carrying ability for ferric iron by over 10^4 times more than can dehydration fluids (Mungall, 2002). This high redox potential of the melts allows not only to maintain sulfur in oxidized forms (Hamilyn and others, 1985), but the removal of chalcophile elements (for example, Ag, As, Bi, Cu, Se, and Te) from the mantle wedge during hybridization into the sulfide-undersaturated silicate melt. Metals remain in the melt until they are partitioned into the exsolved hydrothermal fluids. Although we agree that most arc magmas (by dehydration of slab melting) are H_2O-rich and represent an essential parameter to magmatic-hydrothermal ore-forming systems (Richards, 2011), in nascent arcs with boninite-adakite (FI/FII-types) associations, the higher fO_2 (redox state) from slab-melting may explain the Au-Ag endowment in ore-deposits, regardless of the magmatic water content. From their work on the LaRonde Penna Au-rich VMS deposit in Abitibi, Mercier-Langevin and others (2007) recognized the hosting potential of FI-type rhyolite elsewhere and the results presented here provide a possible explanation for their enrichment in precious metals from a petrogenetic perspective. The boninite-adakite(FI-/FII-types) association observed in terranes as old as the Archean may therefore become an important geological assemblage for exploration for precious metal-rich VMS deposits.

CONCLUSIONS

The study of the felsic volcanic and volcaniclastic rocks that host the Ming VMS deposit in Newfoundland, using a variety of major, trace, and isotopic Sm-Nd systematics on least-altered rocks, suggests that their HREE and HFSE depletion (FI- and FII-type) were products of subducted slab-derived partial melts generated at relatively low temperatures (<750 °C) where garnet and amphibole were stable in the residue. Although felsic successions have been observed in small amounts elsewhere on the peninsula, the Rambler Rhyolite formation is the result of a combination of optimal conditions (for example, locally more hydrated crusts and/or higher geothermal gradient) to generate larger amounts of partial melting. Batch melting calculations

using island arc tholeiite source suggests ~10 percent partial melting is sufficient to emulate the immobile trace element compositions of the Rambler Rhyolite formation. Moreover, slab melting was likely critical in generating oxidized, sulfide undersaturated, siliceous magmas from which precious metals and other magmatophile elements were later exsolved during ascent and/or cooling. Slab melting of island arc tholeiites in a subduction environment is consistent with recent tectonic reconstructions proposed by other workers for the Baie Verte oceanic tract. The magmas derived from these slab melting events have FI to FII affinities, often considered less prospective for VMS mineralization; however, this work has illustrated that FI- and FII-type felsic volcanic rocks may no longer be regarded as non-prospective for hosting VMS, and may be important for the formation of Au-Ag-rich VMS deposits given the increasing numbers of recent studies reporting their associations with Au-Ag-rich VMS in Archean to Paleozoic successions.

The complex stratigraphic and geochemical relationships of the base of the overlying Snooks Arm Group suggest the extension of the overriding plate (evidenced by the presence of rift-related primitive tholeiitic rocks) while the contribution from the subducted slab continued (presence of evolved transitional to calk-alkalic rocks). The lack of geochronological constraints makes it difficult to determine the time span from the formation of the Ming deposit and the deposition of the volcanic rocks of the Snooks Arm Group. However, the lack of visible unconformity (let alone the presence of the thin Fe-shale sequence reflecting volcanic hiatus) and the interstratification of different volcanic units suggest that the onset of the Snooks Arm volcanism occurred shortly after the formation of the Ming deposit.

ACKNOWLEDGMENTS

The authors would like to thank Larry Pilgrim, Paul Legrow, and the staff of Rambler Metals and Mining Canada Ltd. for providing access to the underground workings, drill core, data, and samples; the miners who work or have worked at surface or underground for accommodating so generously despite the busy production schedule; Pam King (retired), Sherry Strong, and Lakmali Hewu (retired) of CREAIT at Memorial University of Newfoundland (MUN) for their technical support and guidance during the multiple stages of sample preparation and geochemical and isotopic analyses. We appreciate the technical support from and insightful discussions with S.M. Brueckner (Auburn University), J.M. Hanchar (MUN), G. Dunning (MUN), P. Mercier-Langevin (GSC), and T. Skulski (GSC). This research was funded by grants to S.J. Piercey, including a NSERC Discovery Grant and the NSERC-Altius Industrial Research Chair in Mineral Deposits funded by NSERC, Altius Minerals Inc., and the Research and Development Corporation of Newfoundland and Labrador. This study was also funded in part by the Geological Survey of Canada's Volcanogenic Massive Sulphide Ore System of the Targeted Geoscience Initiative 4 (TGI-4) Program. This manuscript was significantly improved through the reviews of C.R. van Staal, H.S. Swinden, and W. Sun.

APPENDIX A

Selection of Least-Altered Samples

The felsic rocks that host the Ming VMS deposit are in many parts of the deposit, affected by hydrothermal alteration. A regional metamorphic overprint (upper greenschist facies) affects all rocks of the peninsula and therefore, fluids associated with both hydrothermal alteration and metamorphism could have mobilized elements that are most susceptible to these secondary events (large ion lithophile (LILE); Cs, K, Ba, Sr). Petrogenetic signatures and primary geochemical discriminations of a suite of samples can only be achieved using elements that are relatively immune to secondary processes, such as high field strength elements (HFSE; Zr, Nb, Y, Ti, V) and rare earth elements (REE; La-Lu). Although the latter group of elements are generally immobile and resistant to alteration, in order to avoid the exception, only samples that meet the following criteria were used for primary characterization: 1) presence of primary features in a

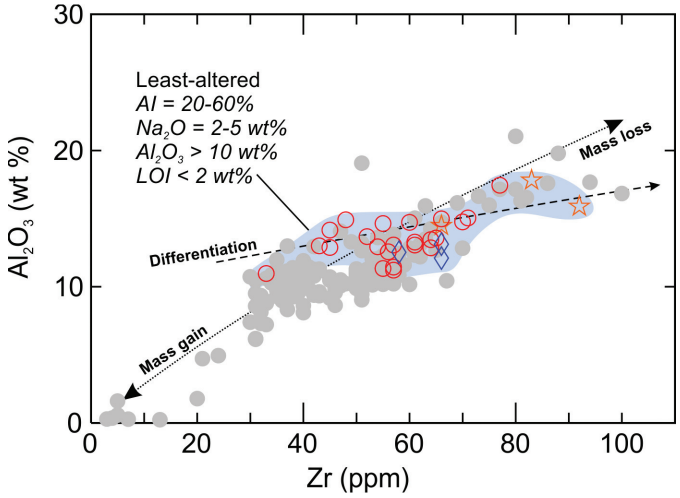

Fig. A1. Al_2O_3 vs. Zr diagram. This plot shows the variation in Al_2O_3 and Zr contents due to mass change associated with hydrothermal alteration (gray circles). This highlights the importance for establishing a rigorous set of criteria when determining rocks that are the least altered and subsequently used for petrogenetic assessments. See text for details. Symbols for least-altered samples are as in figure 4.

mineralogical assemblage that shows minimal evidence or absence of hydrothermal alteration in thin sections (for example, interlocking textures, relic feldspar/amphibole phenocrysts, absence of triple junctions in quartz, absence of foliation or porphyroblasts); 2) loss on ignition (LOI) contents lower than or equal to 2 wt %; 3) Al_2O_3 content higher than 10 wt %; 4) Na_2O between 2 and 5 wt %; and 5) alteration index (AI) between 20 and 60. Aluminum is used here as a proxy for mass change. Samples with less than 10 wt % Al_2O_3 are generally indicative of significant mass gain, hence possible leaching of key diagnostic elements (Lentz, 1998). In figure A1, we compare samples that satisfy the rigorous criteria above with samples that show evidence of alteration (for example, chlorite-sericite-carbonate-sulfide alteration). Any variation along a slope that intersects the origin is interpreted as the result of mass changes (see Barrett and MacLean, 1994), whereas differentiation will vary along a shallower slope that intersects the Y-axis.

Because samples of the cover sequence and associated dikes post-date the ore-forming hydrothermal activity, it is reasonable to assume that the use of immobile elements such as HFSE and REE will most likely reflect the original geochemical signatures of these rocks. We have nonetheless applied selection, but less rigorous than the underlying felsic rocks, criteria, that is only samples with Na_2O between 2 and 5 wt % and AI between 20 and 60 were used in this study (supplementary data, http://earth.geology.yale.edu/%7eajs/SupplementaryData/2018/Pilote).

APPENDIX B

Analytical Methods

Whole-rock major, trace, and rare earth elements (REE).—A total of 312 samples from the Ming deposit were selected from eight underground workings and 22 drill holes. The sampling methodology during field work was twofold: 1) collect least-altered samples from each unit and facies for a complete primary geochemical characterization (this study) and 2) collect samples throughout the deposit to reconstruct the hydrothermal alteration architecture, which will be published subsequently.

The samples were analyzed for major element oxides (SiO_2, Al_2O_3, Fe_2O_3, MnO, MgO, CaO, Na_2O, K_2O, TiO_2, and P_2O_5) and a selective suite of trace elements (Sr, Sc, and Zr) at Activation Laboratories Ltd. in Ancaster, Ontario, Canada. The samples were crushed and pulverized using mild steel before undergoing lithium metaborate/tetraborate fusion followed by HF-HNO_3 dissolution and subsequent analysis by inductively coupled plasma emission-mass spectrometry (ICP-ES). A laboratory-independent quality control and assurance using the relative difference (%RD) method of Jenner (1996) and Piercey (2014) on four different reference materials (JR-1, BAMAP-01, PER-1, and CHA-2) of mafic to felsic compositions revealed excellent (<3%RD) accuracy for all major elements, except for P_2O_5 (>10%), which can be explained by the values being below lower limits of detection and/or quantification. For the trace elements, Sr showed

TABLE B1

Analytical Precision for Each Element

	CV (%)	n		CV (%)	n
SiO_2	0.75	17	Gd	4.28	15
Al_2O_3	1.24	17	Tb	4.64	15
Fe_2O_{3t}	0.80	17	Dy	3.97	15
MnO	0.92	17	Ho	4.86	15
MgO	1.35	17	Er	5.21	15
CaO	1.13	17	Tm	4.95	15
Na_2O	0.97	17	Yb	6.07	15
K_2O	1.46	17	Lu	9.00	15
TiO_2	1.35	17	Ta	15.31	15
P_2O_5	9.65	17	Tl	14.21	15
LOI	1.77	17	Pb	14.76	15
Sr	1.12	17	Bi	15.26	15
Sc	1.67	17	Th	4.36	15
Zr	1.48	17	U	5.67	14
Ba	4.10	15	V	8.26	16
Y	4.66	15	Cr	8.44	16
Nb	5.50	15	Co	8.54	16
Cs	6.13	15	Ni	11.18	16
La	3.17	15	Cu	33.95	16
Ce	2.91	15	Zn	10.93	16
Pr	2.93	15	As	36.80	16
Nd	3.67	15	Sn	21.84	16
Sm	3.68	15	Sb	17.70	16
Eu	3.15	15			

n = number of duplicate sets.

very good accuracy (<5%RD), whereas both Sc and Zr showed excellent (<3%RD) to good (~10%RD) recoveries.

An additional suite of trace elements, including LILE, REE, and HFSE, were analyzed by the first author at the Department of Earth Sciences at Memorial University of Newfoundland using the pulps returned from the Activation Laboratory Ltd. The dissolution procedure used here is a modified version of that described by Jenner and others (1990) and Longerich and others (1990) and includes the following: 0.1 g of each sample were weighed into a dry teflon screw cap jar with the addition of 2 ml of 8N HNO_3 and 1 ml of HF acids. The covered jars were then placed onto a hot plate at 70 °C for ~72 hours. The covers were removed and rinsed with nanopure water and left on the hot plate at 100 °C until complete dryness. 2 ml of 8N HNO_3 and 1 ml of HF acids were added, covered for ~24 hours, and dried. 2 ml 8N HNO_3 acid and 1 ml boric acid (0.453M) were added and dried. 2 ml of 8N HNO_3 acid was added then dried. The latter step was repeated. Finally, 2 ml of 8N HNO_3 acid was added, covered, cooled, and transferred into a 120 ml snap seal container with an addition of 1.3 ml oxalic acid (0.22M), 0.665 ml of HF/boric (0.113M HF/0.453M boric) solution, and nanopure water to make up to a final weight of 60 g. Samples were then spiked and analyzed using a Perkin Elmer Elan DRCII Quad© inductively coupled plasma-mass spectrometry (ICP-MS) instrument and followed by offline data reduction. Using the reference materials AGV-2 and JR-1, accuracy tests (relative differences; %RD) on all samples yielded excellent accuracy (<3%RD) for Nb, Ba, Cs, La, Ce, Pr, Nd, Er, Tm, Lu, Pb, Tl and U, very good accuracy (3-7%RD) for Sm, Eu, Gd, Tb, Dy, Ho, Yb, Ta, Bi, V, Sb, Cr, and Ni, and good accuracy (http://earth.geology.yale.edu/%7eajs/SupplementaryData/2018/Pilote).

Precision was calculated for each analyzed element by using a series of sample duplicates (Jenner, 1996). Table B1 shows the calculated precision values as coefficient of variation (CV), which is

$$CV\ (\%) = 100*SD/X$$

where SD is the standard deviation and X the population mean (Jenner ,1996). Most elements show excellent (≤3%) to good (≤10%) precisions, except for Ta, Tl, Pb, Bi, Ni, Cu, Zn, As, Sn, and Sb, which show imprecise (>10%) values, mainly due to their contents being near the lower limits of detection.

Whole-rock Sm and Nd isotope determination.—Whole-rock powders were dissolved in Savilex© Teflon capsules using an 8 ml (4:1) mixture of 29 M HF – 15 M HNO_3. Prior to acid digestion, a mixed $^{150}Nd/^{149}Sm$ spike is added to each sample. After five days of acid digestion on a hotplate, the solution is then evaporated

to dryness, taken back up in 6M HCl for 4-5 days. The sample is finally dried down and then re-dissolved in 2.5 M HCL. The sample is loaded into column containing cation exchange resin AG-50W-X8, H+ form, and 200–400 mesh where a fraction containing REE is isolated. This REE split is then dried and taken up in 0.18 M HCl and loaded on a column containing Eichrom© Ln resin (50-100 mesh) to isolate Sm and Nd separately from the other REE. All reagents are purified in order to ensure a low contamination level. Sm and Nd concentrations and isotopic compositions are determined using a multi-collector Finnigan Mat 262 mass spectrometer at Memorial University of Newfoundland in static mode for concentration determination, and dynamic mode for isotopic composition determination. Instrumental mass fractionation of Sm and Nd isotopes are corrected using a Rayleigh law relative to $^{146}Nd/^{144}Nd = 0.7219$ and $^{152}Sm/^{147}Sm = 1.783$. The reported $^{143}Nd/^{144}Nd$ ratio is corrected for the deviation from repeated duplicates of the JNdi-1 ($^{143}Nd/^{144}Nd = 0.512115$, Tanaka and others, 2000) standard. Replicates of the standard give a 4-month (June-September, 2015) mean value of $^{143}Nd/^{144}Nd = 0.512100 \pm 0.000016$ (2σ, n = 23) and a long-term (2010-2015) mean value of $^{143}Nd/^{144}Nd = 0.512101 \pm 0.000016$ (2σ, n = 185).

The TIMS laboratory periodically analyzes the USGS whole-rock reference material BCR-2 with each analysis comprising a separate dissolution and thus provides the best estimate of the reproducibility of an individual whole-rock analysis. The results of their BCR-2 analyses over time show an average value of 0.512636 ± 0.000014 (2σ, n = 11), which is in agreement with the results reported by Raczek and others (2003), Weis and others (2005), and Jweda and others (2016).

REFERENCES

Arculus, R. J., and Powell, R., 1986, Source component mixing in the regions of arc magma generation: Journal of Geophysical Research-Solid Earth, v. 91, n. B6, p. 5913–5926, https://doi.org/10.1029/JB091iB06p05913

Barrett, T. J., and MacLean, W. H., 1994, Chemostratigraphy and hydrothermal alteration in exploration for VHMS deposits in greenstones and younger volcanic rocks: Geological Association of Canada, Short Course Notes 11, p. 433–467.

——— 1999, Volcanic sequences, lithogeochemistry, and hydrothermal alteration in some bimodal volcanic-associated massive sulfide systems, *in* Barrie, C. T., and Hannington, M. D., editors, Volcanic Associated Massive Sulfide Deposits: Processes and Examples in Modern and Ancient Settings: Reviews in Economic Geology, v. 8, p. 101–131, https://doi.org/10.5382/Rev.08

Beard, J. S., and Lofgren, G. E., 1991, Dehydration melting and water-saturated melting of basaltic and andesitic greenstones and amphibolites at 1, 3 and 6.9 kb: Journal of Petrology, v. 32, n. 2, p. 365–401, https://doi.org/10.1093/petrology/32.2.365

Bédard, J. H., 1999, Petrogenesis of boninites from the Betts Cove ophiolite, Newfoundland, Canada: Identification of subducted source components: Journal of Petrology, v. 40, p. 1853–1889, https://doi.org/10.1093/petroj/40.12.1853

Bédard, J. H., and Escayola, M., 2010, The Advocate Ophiolite mantle, Baie Verte, Newfoundland: Regional correlations and evidence for metasomatism: Canadian Journal of Earth Sciences, v. 47, n. 3, p. 237–253, https://doi.org/10.1139/E10-004

Bédard, J. H., Lauzière, K., Sangster, A., Boisvert, E., Tellier, M., Tremblay, A., and Dec, T., 1996, Geological map of the Betts Cove ophiolitic massif and its cover rocks: Geological Survey of Canada, Canadian Geoscience Map 3271, scale 1:20 000, https://doi.org/10.4095/208188

Bédard, J. H., Lauzière, K., Tremblay, A., and Sangster, A., 1998, Evidence for forearc seafloor-spreading from the Betts Cove ophiolite, Newfoundland: Oceanic crust of boninitic affinity: Tectonophysics, v. 284, n. 3–4, p. 233–245, https://doi.org/10.1016/S0040-1951(97)00182-0

Bhatia, M. R., and Crook, K. A. W., 1986, Trace element characteristics of graywackes and tectonic setting discrimination of sedimentary basins: Contributions to Mineralogy and Petrology, v. 92, n. 2, p. 181–193, https://doi.org/10.1007/BF00375292

Bourdon, E., Eissen, J.-P., Gutscher, M.-A., Monzier, M., Samaniego, P., Robin, C., Bollinger, C., and Cotten, J., 2002, Slab melting and slab melt metasomatism in the Northern Andean Volcanic Zone: Adakites and high-Mg andesites from Pichincha volcano (Ecuador): Bulletin de la Société Géologique de France, v. 173, n. 3, p. 195–206, https://doi.org/10.2113/173.3.195

Brueckner, S. M., Piercey, S. J., Sylvester, P. J., Pilgrim, L., Maloney, S., Hyde, D., and Ogilvie, G., 2011, Stratigraphy, mineralogy, geochemistry, and genesis of an Au-rich volcanogenic massive sulfide (VMS) system from the Baie Verte Peninsula, NW Newfoundland, Canada: The 1806 zone as an example from the Ming Mine, Rambler Camp, *in* Deschenes, G., Dimitrakopoulos, R., and Bouchard, J., editors, World Gold 2011: Montreal, Quebec, Canada, Canadian Institute of Mining, Metallurgy and Petroleum, p. 899–911.

Brueckner, S. M., Piercey, S. J., Sylvester, P. J., Maloney, S., and Pilgrim, L., 2014, Evidence for syngenetic precious metal enrichment in an Appalachian volcanogenic massive sulfide system: The 1806 Zone, Ming Mine, Newfoundland, Canada: Economic Geology, v. 109, n. 6, p. 1611–1642, https://doi.org/10.2113/econgeo.109.6.1611

Brueckner, S. M., Piercey, S. J., Layne, G. D., Piercey, G., and Sylvester, P. J., 2015, Variations of sulphur isotope signatures in sulphides from the metamorphosed Ming Cu(−Au) volcanogenic massive sulphide deposit, Newfoundland Appalachians, Canada: Mineralium Deposita, v. 50, p. 1–22, https://doi.org/10.1007/s00126-014-0567-7

Brueckner, S. M., Piercey, S. J., Pilote, J.-L., Layne, G. D., and Sylvester, P. J., 2016, Mineralogy and mineral

chemistry of the metamorphosed and precious metal-bearing Ming deposit, Canada: Ore Geology Reviews, v. 72, Part 1, p. 914–939, https://doi.org/10.1016/j.oregeorev.2015.09.016
Cabanis, B., and Lecolle, M., 1989, Le diagramme La/10–Y/15–Nb/8: un outil pour la discrimination des séries volcaniques et la mise en évidence des processus de mélange et/ou de contamination crustal: Comptes Rendus de l'Académie des Sciences, v. 309, p. 2023–2029.
Castillo, P. R., 2006, An overview of adakite petrogenesis: Chinese Science Bulletin, v. 51, n. 3, p. 257–268, https://doi.org/10.1007/s11434-006-0257-7
——— 2012, Adakite petrogenesis: Lithos, v. 134–135, p. 304–316, https://doi.org/10.1016/j.lithos.2011.09.013
Castonguay, S., Skulski, T., van Staal, C. R., and Currie, M., 2009, New insights on the structural geology of the Pacquet Harbour group and Point Rousse complex, Baie Verte Peninsula, Newfoundland: Newfoundland and Labrador Department of Natural Resources, Geological Survey, Current Research, Report 09-1, p. 147–158.
Castonguay, S., van Staal, C. R., Joyce, N., Skulski, T., and Hibbard, J. P., 2014, Taconic metamorphism preserved in the Baie Verte Peninsula, Newfoundland Appalachians: Geochronological evidence for ophiolite obduction and subduction and exhumation of the leading edge of the Laurentian (Humber) margin during closure of the Taconic seaway: Geoscience Canada, v. 14, n. 4, p. 459–482, https://doi.org/10.12789/geocanj.2014.41.055
Cawood, P. A., and Suhr, G., 1992, Generation and obduction of ophiolites: Constraints from the Bay of Islands Complex, western Newfoundland: Tectonics, v. 11, n. 4, p. 884–897, https://doi.org/10.1029/92TC00471
Cawood, P. A., van Gool, J. A. M., and Dunning, G. R., 1996, Geological development of eastern Humber and western Dunnage zones: Corner Brook-Glover Island region, Newfoundland: Canadian Journal of Earth Sciences, v. 33, n. 2, p. 182–198, https://doi.org/10.1139/e96-017
Condie, K. C., and Wronkiewicz, D. J., 1990, The Cr/Th ratio in Precambrian pelites from the Kaapvaal Craton as an index of craton evolution: Earth and Planetary Science Letters, v. 97, n. 3–4, p. 256–267, https://doi.org/10.1016/0012-821X(90)90046-Z
Cousineau, P. A., and Bédard, J. H., 2000, Sedimentation in a subaqueous arc/back-arc setting: The Bobby Cove Formation, Snooks Arms Group, Newfoundland: Precambrian Research, v. 101, n. 2–4, p. 111–134, https://doi.org/10.1016/S0301-9268(99)00097-2
Defant, M. J., and Drummond, M. S., 1990, Derivation of some modern arc magmas by melting of young subducted lithosphere: Nature, v. 347, p. 662–665, https://doi.org/10.1038/347662a0
Defant, M. J., and Kepezhinskas, P., 2001, Evidence suggests slab melting in arc magmas: Eos, Transactions, American Geophysical Union, v. 82, n. 6, p. 65, https://doi.org/10.1029/01EO00038
DeGrace, J. R., Kean, B. F., Hsu, E., and Green, T., 1976, Geology of the Nippers Harbour area (2E/13), Newfoundland: Newfoundland, Canada, Department of Mines and Energy, Report 76-3, 73 p., scale 1:50 000.
DePaolo, D. J., 1981, Trace element and isotopic effects of combined wallrock assimilation and fractional crystallization: Earth and Planetary Science Letters, v. 53, n. 2, p. 189–202, https://doi.org/10.1016/0012-821X(81)90153-9
Dewey, J. F., 2002, Transtension in arcs and orogens: International Geology Review, v. 44, n. 5, p. 402–439, https://doi.org/10.2747/0020-6814.44.5.402
Dewey, J. F., and Casey, J. F., 2015, Reply to Discussion on "The sole of an ophiolite; the Ordovician Bay of Islands Complex, Newfoundland" 170, 2013, p. 715–722: Journal of the Geological Society, London, v. 172, p. 521–532, https://doi.org/10.1144/jgs2014-086
Drummond, M. S., Defant, M. J., and Kepezhinskas, P. K., 1996, Petrogenesis of slab-derived trondhjemite-tonalite-dacite/adakite magmas: Geological Society of America, Special Papers, v. 315, p. 205–215, https://doi.org/10.1130/0-8137-2315-9.205
Dunning, G. R., and Krogh, T. E., 1985, Geochronology of ophiolites of the Newfoundland Appalachians: Canadian Journal of Earth Sciences, v. 22, n. 11, p. 1659–1670, https://doi.org/10.1139/e85-174
Falloon, T. J., Danyushevsky, L. V., Crawford, A. J., Meffre, S., Woodhead, J. D., and Bloomer, S. H., 2008, Boninites and adakites from the northern termination of the Tonga Trench: Implications for adakite petrogenesis: Journal of Petrology, v. 49, n. 4, p. 697–715, https://doi.org/10.1093/petrology/egm080
Franklin, J. M., Lydon, J. W., and Sangster, D. F., 1981, Volcanic-associated sulfide deposits: Economic Geology Publishing Company, Seventy-Fifth Anniversary Volume, p. 485–627, https://doi.org/10.5382/AV75.15
Franklin, J. M., Gibson, H. L., Jonasson, I. R., and Galley, A. G., 2005, Volcanogenic massive sulfide deposits, *in* Hedenquist, J. W., Thompson, J. F. H., Goldfarb, R. J., and Richards, J. P., editors, Economic Geology 100th Anniversary Volume, p. 523–560, https://doi.org/10.5382/AV100.17
Frey, F. A., Green, D. H., and Roy, S. D., 1978, Integrated models of basalt petrogenesis: A study of quartz tholeiites to olivine melilitites from South eastern Australia utilizing geochemical and experimental petrological data: Journal of Petrology, v. 19, n. 3, p. 463–513, https://doi.org/10.1093/petrology/19.3.463
Gaboury, D., and Daigneault, R., 1999, Evolution from sea floor-related to sulfide-rich quartz vein-type gold mineralization during deep submarine volcanic construction; the Géant Dormant gold mine, Archean Abitibi Belt, Canada: Economic Geology, v. 94, n. 1, p. 3–22, https://doi.org/10.2113/gsecongeo.94.1.3
Gaboury, D., and Pearson, V., 2008, Rhyolite geochemical signatures and association with volcanogenic massive sulfide deposits: Examples from the Abitibi Belt, Canada: Economic Geology, v. 103, n. 7, p. 1531–1562, https://doi.org/10.2113/gsecongeo.103.7.1531
Gauthier, M., Baillargeon, F., and Legault, M., 2003, Étude des faciès sédimentaires et des faciès d'altération primaires du gisement d'or archéen d'Eagle-Telbel, canton de Joutel, Abitibi: Géologie Québec Report MB 2002-06, 33 p.

Hamilyn, P. R., Keays, R. R., Cameron, W. E., Crawford, A. J., and Waldron, H. M., 1985, Precious metals in magnesian low-Ti lavas: Implications for metallogenesis and sulfur saturation in primary magmas: Geochimica et Cosmochimica Acta, v. 49, n. 8, p. 1797–1811, https://doi.org/10.1016/0016-7037(85)90150-4

Hanchar, J. M., and Watson, E. B., 2003, Zircon saturation thermometry: Reviews in Mineralogy and Geochemistry, v. 53, p. 89–112, https://doi.org/10.2113/0530089

Hannington, M. D., Poulsen, K. H., Thompson, J. F. H., and Sillitoe, R. H., 1999, Volcanogenic gold in the massive sulfide environment, *in* Barrie, C. T., Hannington, M. D. , editors, Volcanic-associated massive sulfide deposits: Processes and examples in modern and ancient settings: Reviews in Economic Geology, v. 8, p. 325–351, https://doi.org/10.5382/Rev.08.14

Hannington, M. D., De Ronde, C. E. J., and Petersen, S., 2005, Sea-floor tectonics and submarine hydrothermal systems: Economic Geology 100th Anniversary Volume, p. 111–141, https://doi.org/10.5382/AV100.06

Hart, T. R., Gibson, H. L., and Lesher, C. M., 2004, Trace element geochemistry and petrogenesis of felsic volcanic rocks associated with volcanogenic massive Cu-Zn-Pb sulfide deposits: Economic Geology, v. 99, n. 5, p. 1003–1013, https://doi.org/10.2113/gsecongeo.99.5.1003

Herron, M. M., 1988, Geochemical classification of terrigenous sands and shales from core or log data: Journal of Sedimentary Research, v. 58, n. 5, p. 820–829, https://doi.org/10.1306/212F8E77-2B24-11D7-8648000102C1865D

Hibbard, J. P., 1983, Geology of the Baie Verte Peninsula, Newfoundland: St. John's, Newfoundland, Canada, Department of Mines and Energy, Government of Newfoundland and Labrador, Memoir 2, 279 p.

Hinchey, J. G., 2011, The Tulks Volcanic Belt, Victoria Lake Supergroup, Central Newfoundland – Geology, tectonic setting and volcanogenic massive sulphide mineralization: St. John's, Newfoundland, Canada, Government of Newfoundland and Labrador, Department of Natural Resources, Geological Survey, St. John's, Report 2011-02, 167 p.

Irvine, T. N., and Baragar, W. R. A., 1971, A guide to the chemical classification of the common volcanic rocks: Canadian Journal of Earth Sciences, v. 8, n. 5, p. 523–548, https://doi.org/10.1139/e71-055

Ishikawa, Y., Sawaguchi, T., Iwaya, S., and Horiuchi, M., 1976, Delineation of prospecting targets for Kuroko deposits based on modes of volcanism of underlying dacite and alteration halos: Mining Geology, v. 26, n. 136, p. 105–117, https://doi.org/10.11456/shigenchishitsu1951.26.105

Ishiwatari, A., Yanagida, Y., Li, Y. B., Ishii, T., Haraguchi, S., Koizumi, K., Ichiyama, Y., and Umeka, M., 2006, Dredge petrology of the boninite- and adakite-bearing Hahajima Seamount of the Ogasawara (Bonin) forearc: An ophiolite or a serpentinite seamount?: Island Arc, v. 15, n. 1, p. 102–118, https://doi.org/10.1111/j.1440-1738.2006.00512.x

Ishizuka, O., Kimura, J. I., Li, Y. B., Stern, R. J., Reagan, M. K., Taylor, R. N., Ohara, Y., Bloomer, S. H., Ishii, T., Hargrove, U. S., III, and Haraguchi, S., 2006, Early stages in the evolution of Izu-Bonin arc volcanism: New age, chemical, and isotopic constraints: Earth and Planetary Science Letters, v. 250, n. 1–2, p. 385–401, https://doi.org/10.1016/j.epsl.2006.08.007

Ishizuka, O., Tani, K., Reagan, M. K., Kanayama, K., Umino, S., Harigane, Y., Sakamoto, I., Miyajima, Y., Yuasa, M., and Dunkley, D. J., 2011, The timescales of subduction initiation and subsequent evolution of an oceanic island arc: Earth and Planetary Science Letters, v. 306, n. 3–4, p. 229–240, https://doi.org/10.1016/j.epsl.2011.04.006

Jenner, G. A., 1996, Trace element geochemistry of igneous rocks; geochemical nomenclature and analytical geochemistry: Geological Association of Canada, Short Course Notes 12, p. 51–77.

Jenner, G. A., Longerich, H. P., Jackson, S. E., and Fryer, B. J., 1990, ICP-MS – a powerful tool for high-precision trace element analysis in Earth sciences: Evidence from analysis of selected USGS reference samples: Chemical Geology, v. 83, n. 1–2, p. 133–148, https://doi.org/10.1016/0009-2541(90)90145-W

Jweda, J., Bolge, L., Class, C., and Goldstein, S. L., 2016, High precision Sr-Nd-Hf-Pb isotopic compositions of USGS reference material BCR-2: Geostandards and Geoanalytical Research, v. 40, n. 1, p. 101–115, https://doi.org/10.1111/j.1751-908X.2015.00342.x

Kay, R. W., 1978, Aleutian magnesian andesites: Melts from subducted Pacific Ocean crust: Journal of Volcanology and Geothermal Research, v. 4, n. 1–2, p. 117–132, https://doi.org/10.1016/0377-0273(78)90032-X

Kean, B. F., Evans, D. T. W., and Jenner, G. A., 1995, Geology and mineralization of the Lushs Bight Group: St. John's, Newfoundland, Canada, Newfoundland and Labrador Department of Natural Resources, Geological Survey, Report 95-2, 223 p.

Kelemen, P. B., 1995, Genesis of high Mg# andesites and the continental crust: Contributions to Mineralogy and Petrology, v. 120, n. 1, p. 1–19, https://doi.org/10.1007/BF00311004

Kelemen, P. B., Hanghøj, K., and Greene, A. R., 2003, One view of the geochemistry of subduction-related magmatic arcs, with emphasis on primitive andesite and lower crust,: Elsevier, Treatise on Geochemsitry, v. 3, p. 593–659, https://doi.org/10.1016/B0-08-043751-6/03035-8

Kepezhinskas, P., Defant, M. J., and Drummond, M. S., 1996, Progressive enrichment of island arc mantle by melt-peridotite interaction inferred from Kamchatka xenoliths: Geochimica et Cosmochimica Acta, v. 60, n. 7, p. 1217–1229, https://doi.org/10.1016/0016-7037(96)00001-4

Kessler, L. G., and Bédard, J. H., 2000, Epiclastic volcanic debrites-evidence of flow transformations between avalanche and debris flow processes, Middle Ordovician, Baie Verte Peninsula, Newfoundland, Canada: Precambrian Research, v. 101, n. 2–4, p. 135–161, https://doi.org/10.1016/S0301-9268(99)00086-8

Langmuir, C. H., Bender, J. F., Bence, A. E., Hanson, G. N., and Taylor, S. R., 1977, Petrogenesis of basalts from the FAMOUS area: Mid-Atlantic Ridge: Earth and Planetary Science Letters, v. 36, n. 1, p. 133–156, https://doi.org/10.1016/0012-821X(77)90194-7

Large, R. R., Gemmell, J. B., Paulick, H., and Huston, D. L., 2001, The alteration box plot: A simple approach to understanding the relationship between alteration mineralogy and lithogeochemistry associated with volcanic-hosted massive sulfide deposits: Economic Geology, v. 96, n. 5, p. 957–971, https://doi.org/10.2113/96.5.957

Lentz, D. R., 1998, Petrogenetic evolution of felsic volcanic sequences associated with Phanerozoic volcanic-hosted massive sulphide systems: The role of extensional geodynamics: Ore Geology Reviews, v. 12, n. 5, p. 289–327, https://doi.org/10.1016/S0169-1368(98)00005-5

Lesher, C. M., Goodwin, A. M., Campbell, I. H., and Gorton, M. P., 1986, Trace-element geochemistry of ore-associated and barren, felsic metavolcanic rocks in the Superior Province, Canada: Canadian Journal of Earth Sciences, v. 23, n. 2, p. 222–237, https://doi.org/10.1139/e86-025

Li, Y., Kimura, J.-I., Machida, S., Ishii, T., Ishiwatari, A., Maruyama, S., Qiu, H., Ishikawa, T., Kato, Y., Haraguchi, S., Takahata, N., Hirahara, Y., and Miyazaki, T., 2013, High-Mg adakite and low-Ca boninite from a Bonin fore-arc seamount; implications for the reaction between slab melts and depleted mantle: Journal of Petrology, v. 54, n. 6, p. 1149–1175, https://doi.org/10.1093/petrology/egt008

Longerich, H. P., Jenner, G. A., Fryer, B. J., and Jackson, S. E., 1990, Inductively coupled plasma-mass spectrometric analysis of geological samples: A critical evaluation based on case studies: Chemical Geology, v. 83, n. 1–2, p. 105–118, https://doi.org/10.1016/0009-2541(90)90143-U

Lydon, J. W., 1984, Volcanogenic massive sulphide deposits Part 1: A descriptive model: Geoscience Canada, v. 11, p. 195–202.

——— 1988, Volcanogenic massive sulphide deposits Part 2: Genetic models: Geoscience Canada, v. 15, p. 43–65.

——— 1996, Characteristics of volcanogenic massive sulphide deposits; interpretations in terms of hydrothermal convection systems and magmatic hydrothermal systems: Boletin Geologico y Minero, v. 107, p. 215–264.

Macpherson, C. G., Dreher, S. T., and Thirlwall, M. F., 2006, Adakites without slab melting; high pressure differentiation of island arc magma, Mindanao, the Philippines: Earth and Planetary Science Letters, v. 243, n. 3–4, p. 581–593, https://doi.org/10.1016/j.epsl.2005.12.034

Martin, H., 1987, Petrogenesis of Archaean trondhjemites, tonalites and granodiorites from eastern Finland: Major and trace element geochemistry: Journal of Petrology, v. 28, n. 5, p. 921–953, https://doi.org/10.1093/petrology/28.5.921

——— 1999, Adakitic magmas: Modern analogues of Archaean granitoids: Lithos, v. 46, n. 3, p. 411–429, https://doi.org/10.1016/S0024-4937(98)00076-0

Mercier-Langevin, P., Dubé, B., Hannington, M. D., Richer-Laflèche, M., and Gosselin, G., 2007, The LaRonde Penna Au-rich volcanogenic massive sulfide deposit, Abitibi Greenstone Belt, Quebec: Part II. Lithogeochemistry and paleotectonic setting: Economic Geology, v. 102, n. 4, p. 611–631, https://doi.org/10.2113/gsecongeo.102.4.611

Mungall, J. E., 2002, Roasting the mantle: Slab melting and the genesis of major Au and Au-rich Cu deposits: Geology, v. 30, n. 10, p. 915–918, https://doi.org/10.1130/0091-7613(2002)030<0915:RTMSMA>2.0.CO;2

Nakamura, N., 1974, Determination of REE, Ba, Fe, Mg, Na and K in carbonaceous and ordinary chondrites: Geochimica et Cosmochimica Acta, v. 38, n. 5, p. 757–775, https://doi.org/10.1016/0016-7037(74)90149-5

Niu, H., Sato, H., Zhang, H., Ito, J. I., Yu, X., Nagao, T., Terada, K., and Zhang, Q., 2006, Juxtaposition of adakite, boninite, high TiO_2 and low TiO_2 basalts in the Devonian southern Altay, Xinjiang, NW China: Journal of Asian Earth Sciences, v. 28, n. 4–6, p. 439–456, https://doi.org/10.1016/j.jseaes.2005.11.010

Peacock, S. M., 1990, Fluid processes in subduction zones: Science, v. 248, n. 4953, p. 329–337, https://doi.org/10.1126/science.248.4953.329

Pearce, J. A., 1996, A user's guide to basalt discrimination diagrams: Geological Association of Canada, Short Course Notes 12, p. 79–113.

——— 2008, Geochemical fingerprinting of oceanic basalts with applications to ophiolite classification and the search for Archean oceanic crust: Lithos, v. 100, n. 1–4, p. 14–48, https://doi.org/10.1016/j.lithos.2007.06.016

Pearce, J. A., and Parkinson, I. J., 1993, Trace element models for mantle melting: Application to volcanic arc petrogenesis: Geological Society, London, Special Publications, v. 76, p. 373–403, https://doi.org/10.1144/GSL.SP.1993.076.01.19

Pearce, J. A., and Peate, D. W., 1995, Tectonic implications of the composition of volcanic arc magmas: Annual Review of Earth and Planetary Sciences, v. 23, p. 251–285, https://doi.org/10.1146/annurev.ea.23.050195.001343

Pearce, J. A., van der Laan, S. R., Arculus, R. J., Murton, B. J., Ishii, T., Peate, D. W., and Parkinson, I. J., 1992, Boninite and harzburgite from Leg 125 (Bonin-Mariana forearc): A case study of magma genesis during the initial stages of subduction: Proceedings of the Ocean Drilling Program, Scientific Results, v. 125, p. 623–659, https://doi.org/10.2973/odp.proc.sr.125.172.1992

Pearce, J. A., Baker, P. E., Harvey, P. K., and Luff, I. W., 1995, Geochemical evidence for subduction fluxes, mantle melting and fractional crystallization beneath the South Sandwich island arc: Journal of Petrology, v. 36, n. 4, p. 1073–1109, https://doi.org/10.1093/petrology/36.4.1073

Peate, D. W., and Pearce, J. A., 1998, Causes of spatial compositional variations in Mariana Arc lavas: Trace element evidence: Island Arc, v. 7, n. 3, p. 479–495, https://doi.org/10.1111/j.1440-1738.1998.00205.x

Peate, D. W., Pearce, J. A., Hawkesworth, C. J., Colley, H., Edwards, C. M. H., and Hirose, K., 1997, Geochemical variations in Vanuatu Arc lavas: The role of subducted material and a variable mantle wedge composition: Journal of Petrology, v. 38, n. 10, p. 1331–1358, https://doi.org/10.1093/petroj/38.10.1331

Piercey, S. J., 2007, Volcanogenic massive sulphide (VMS) deposits of the Newfoundland Appalachians: An

overview of their setting, classification, grade-tonnage data and unresolved questions: Newfoundland and Labrador Department of Natural Resources, Geological Survey, Current Research, Report 07-1, p. 169–178.

——— 2010, An overview of petrochemistry in the regional exploration for volcanogenic massive sulphide (VMS) deposits: Geochemistry: Exploration, Environment, Analysis, v. 10, p. 119–136, https://doi.org/10.1144/1467-7873/09-221

——— 2011, The setting, style, and role of magmatism in the formation of volcanogenic massive sulfide deposits: Mineralium Deposita, v. 46, n. 4–5, p. 449–471, https://doi.org/10.1007/s00126-011-0341-z

——— 2014, Modern Analytical Facilities 2. A review of quality assurance and quality control (QA/QC) procedures for lithogeochemical data: Geoscience Canada, v. 41, n. 1, p. 75–88, https://doi.org/10.12789/geocanj.2014.41.035

Piercey, S. J., Jenner, G. A., and Wilton, D. H. C., 1997, The stratigraphy and geochemistry of the southern Pacquet Harbour Group, Baie Verte Peninsula, Newfoundland; implications for mineral exploration: Newfoundland and Labrador Department of Natural Resources, Geological Survey, Current Research, Report 97-1, p. 119–139.

Piercey, S. J., Murphy, D. C., Mortensen, J. K., and Paradis, S., 2001, Boninitic magmatism in a continental margin setting, Yukon-Tanana terrane, southeastern Yukon, Canada: Geology, v. 29, n. 8, p. 731–734, https://doi.org/10.1130/0091-7613(2001)029<0731:BMIACM>2.0.CO;2

Piercey, S. J., Peter, J. M., Mortensen, J. K., Paradis, S., Murphy, D. C., and Tucker, T. L., 2008, Petrology and U-Pb geochronology of footwall porphyritic rhyolites from the Wolverine volcanogenic massive sulfide deposit, Yukon, Canada: Implications for the genesis of massive sulfide deposits in continental margin environments: Economic Geology, v. 103, n. 1, p. 5–33, https://doi.org/10.2113/gsecongeo.103.1.5

Pilgrim, L., 2009, Mineral resource estimate for the Ming Mine, Newfoundland, Canada: Rambler Metals and Mining Canada Ltd., Technical Report NI43-101, 114 p.

Pilote, J.-L., and Piercey, S. J., 2013, Volcanostratigraphy of the 1807 zone of the Ming Cu-Au volcanogenic massive-sulphide deposit, Baie Verte Peninsula, northern Newfoundland: Geological Survey of Canada, Current Research, Report 2013-20, 13 p.

Pilote, J.-L., Piercey, S. J., and Mercier-Langevin, P., 2014, Stratigraphy and hydrothermal alteration of the Ming Cu-Au volcanogenic massive-sulphide deposit, Baie Verte Peninsula, Newfoundland: Geological Survey of Canada, Current Research, Report 2014-17, 18 p.

——— 2015, Volcanic architecture and alteration assemblages of the Ming Cu–Au–(Zn–Ag) VMS Deposit, Baie Verte, Newfoundland and Labrador: implications for Au-enrichment processes and exploration methods development, *in* Peter, J. M., and Mercier-Langevin, P., editors, Targeted Geoscience Initiative 4: Contributions to the Understanding of Volcanogenic Massive Sulfide Deposit Genesis and Exploration: Geological Survey Canada, Open File 7853, p. 1897–210.

Pilote, J.-L., Piercey, S. J., Brueckner, S. M., and Grant, D., 2016, Resolving the relative timing of Au enrichment in volcanogenic massive sulfide deposits using scanning electron microscopy-mineral liberation analyzer: Empirical evidence from the Ming Deposit, Newfoundland, Canada: Economic Geology, v. 111, n. 6, p. 1495–1508, https://doi.org/10.2113/econgeo.111.6.1495

Pilote, J.-L., Piercey, S. J., and Mercier-Langevin, P., 2017, Volcanic and structural reconstruction of the deformed and metamorphosed Ming volcanogenic massive sulfide deposit, Canada: Implications for ore zone geometry and metal distribution: Economic Geology, v. 112, n. 6, p. 1305–1332, https://doi.org/10.5382/econgeo.2017.4511

Polat, A., and Kerrich, R., 2001, Magnesian andesites, Nb-enriched basalt-andesites, and adakites from late Archean 2.7 Ga Wawa greenstone belts, Superior Province, Canada: Implications for late Archean subduction zone petrogenetic processes: Contributions to Mineralogy and Petrology, v. 141, n. 1, p. 36–52, https://doi.org/10.1007/s004100000223

——— 2004, Precambrian arc associations: Boninites, adakites, magnesian andesites, and Nb-enriched basalts: Developments in Precambrian Geology, v. 13, p. 567–597, https://doi.org/10.1016/S0166-2635(04)13017-X

Raczek, I., Jochum, P., and Hofmann, A. W., 2003, Neodymium and strontium isotope data for USGS reference materials BCR-1, BCR-2, BHVO-1, BHVO-2, AGV-1, AGV-2, GSP-1, GSP-2 and eight MPI-DING reference glasses: Geostandards and Geoanalytical Research, v. 27, n. 2, p. 173–179, https://doi.org/10.1111/j.1751-908X.2003.tb00644.x

Ramezani, J., Dunning, G. R., and Wilson, M. R., 2000, Geologic setting, geochemistry of alteration, and U-Pb age of hydrothermal zircon from the Silurian Stog'er Tight gold prospect, Newfoundland Appalachians, Canada: Exploration and Mining Geology, v. 9, n. 3–4, p. 171–188, https://doi.org/10.2113/0090171

Rapp, R. P., 1995, Amphibole-out phase boundary in partially melted metabasalt, its control over liquid fraction and composition, and source permeability: Journal of Geophysical Research-Solid Earth, v. 100, n. B8, p. 15601–15610, https://doi.org/10.1029/95JB00913

Reagan, M. K., Ishizuka, O., Stern, R. J., Kelley, K. A., Ohara, Y., Blichert-Toft, J., Bloomer, S. H., Cash, J., Fryer, P., Hanan, B. B., Hickey-Vargas, R., Ishii, T., Kimura, J.-I., Peate, D. W., Rowe, M. C., and Woods, M., 2010, Fore-arc basalts and subduction initiation in the Izu-Bonin-Mariana system: Geochemistry, Geophysics, Geosystems, v. 11, n. 3, 17 p., https://doi.org/10.1029/2009GC002871

Richards, J. P., 2011, High Sr/Y arc magmas and porphyry Cu ± Mo ± Au deposits: Just add water: Economic Geology, v. 106, n. 7, p. 1075–1081, https://doi.org/10.2113/econgeo.106.7.1075

Richards, J. P., and Kerrich, R., 2007, Adakite-like rocks: Their diverse origins and questionable role in metallogenesis: Economic Geology, v. 102, n. 4, p. 537–576, https://doi.org/10.2113/gsecongeo.102.4.537

Ross, P.-S., and Bédard, J. H., 2009, Magmatic affinity of modern and ancient subalkaline volcanic rocks

determined from trace-element discriminant diagrams: Canadian Journal of Earth Sciences, v. 46, n. 11, p. 823–839, https://doi.org/10.1139/E09-054
Ryerson, F. J., and Watson, E. B., 1987, Rutile saturation in magmas: Implications for Ti-Nb-Ta depletion in island-arc basalts: Earth and Planetary Science Letters, v. 86, n. 2–4, p. 225–239, https://doi.org/10.1016/0012-821X(87)90223-8
Sajona, F. G., and Maury, R. C., 1998, Association of adakites with gold and copper mineralization in the Philippines: Comptes Rendus de l'Académie des Sciences, Série II- Sciences de la Terre et des Planètes, v. 326, n. 1, p. 27–34, https://doi.org/10.1016/S1251-8050(97)83200-4
Sajona, F. G., Maury, R. C., Bellon, H., Cotten, J., and Defant, M. J., 1996, High field strength element enrichment of Pliocene-Pleistocene island arc basalts, Zamboanga Peninsula, western Mindanao (Philippines): Journal of Petrology, v. 37, n. 3, p. 693–726, https://doi.org/10.1093/petrology/37.3.693
Sajona, F. G., Maury, R. C., Prouteau, G., Cotten, J., Schiano, P., Bellon, H., and Fontaine, L., 2000, Slab melt as metasomatic agent in island arc magma mantle sources, Negros and Batan (Philippines): Island Arc, v. 9, n. 4, p. 472–486, https://doi.org/10.1111/j.1440-1738.2000.00295.x
Sangster, A. L., Douma, S. L., and Lavigne, J., 2007, Base metal and gold deposits of the Betts Cove Complex, Baie Verte Peninsula, Newfoundland, *in* Goodfellow, W. D., editor, Mineral deposits of Canada: A synthesis of major deposit-types, district metallogeny, the evolution of geological provinces, and exploration methods: St. John's, Newfoundland, Canada, Geological Association of Canada, Mineral Deposits Division, Special Publication n. 5, p. 703–722.
Saunders, A. D., Rogers, G., Marriner, G. F., Terrell, D. J., and Verma, S. P., 1987, Geochemistry of Cenozoic volcanic rocks, Baja California, Mexico: Implications for the petrogenesis of post-subduction magmas: Journal of Volcanology and Geothermal Research, v. 32, n. 1–3, p. 223–245, https://doi.org/10.1016/0377-0273(87)90046-1
Sen, C., and Dunn, T., 1994, Dehydration melting of a basaltic composition amphibolite at 1.5 and 2.0 GPa: Implications for the origin of adakites: Contributions to Mineralogy and Petrology, v. 117, n. 4, p. 394–409, https://doi.org/10.1007/BF00307273
Shaw, D. M., 1970, Trace element fractionation during anatexis: Geochimica et Cosmochimica Acta, v. 34, n. 2, p. 237–243, https://doi.org/10.1016/0016-7037(70)90009-8
Shervais, J. W., 1982, Ti-V plots and the petrogenesis of modern and ophiolitic lavas: Earth and Planetary Science Letters, v. 59, n. 1, p. 101–118, https://doi.org/10.1016/0012-821X(82)90120-0
Shukuno, H., Tamura, Y., Tani, K., Chang, Q., Suzuki, T., and Fiske, R. S., 2006, Origin of silicic magmas and the compositional gap at Sumisu submarine caldera, Izu-Bonin arc, Japan: Journal of Volcanology and Geothermal Research, v. 156, n. 3–4, p. 187–216, https://doi.org/10.1016/j.jvolgeores.2006.03.018
Sillitoe, R. H., Hannington, M. D., and Thompson, J. F. H., 1996, High sulfidation deposits in the volcanogenic massive sulfide environment: Economic Geology, v. 91, n. 1, p. 204–212, https://doi.org/10.2113/gsecongeo.91.1.204
Skulski, T., Castonguay, S., McNicoll, V., van Staal, C. R., Kidd, W. S. F., Rogers, N., Morris, W., Ugalde, H., Slavinski, H., Spicer, W., Moussallam, Y., and Kerr, I., 2010, Tectonostratigraphy of the Baie Verte oceanic tract and its ophiolite cover sequence on the Baie Verte Peninsula: Newfoundland and Labrador Department of Natural Resources, Geological Survey, Current Research, Report 10-1, p. 315–335.
Skulski, T., Castonguay, S., Kidd, W. S. F., McNicoll, V., van Staal, C. R., and Hibbard, J. P., 2015, Geology, Baie Verte and parts of Fleur de Lys, Newfoundland and Labrador, NTS 12-H/16 and part of NTS 12-I/1: Geological Survey of Canada, Canadian Geoscience Map 159, scale 1:50 000, https://doi.org/10.4095/295865
Skulski, T., Castonguay, S., Côté, N., McNicoll, V. J., Currie, M., Magee, A., Harris, B., and van Staal, C. R., 2017, Digital geoscience atlas of Baie Verte Peninsula, Newfoundland and Labrador: Geological Survey of Canada, Open File 7342, https://doi.org/10.4095/298754
Smithies, R. H., 2000, The Archaean tonalite-trondhjemite-granodiorite (TTG) series is not an analogue of Cenozoic adakite: Earth and Planetary Science Letters, v. 182, n. 1, p. 115–125, https://doi.org/10.1016/S0012-821X(00)00236-3
Solomon, M., and Zaw, K., 1997, Formation on the sea floor of the Hellyer volcanogenic massive sulfide deposit: Economic Geology, v. 92, n. 6, p. 686–695, https://doi.org/10.2113/gsecongeo.92.6.686
Spulber, S. D., and Rutherford, M. J., 1983, The origin of rhyolite and plagiogranite in oceanic crust: An experimental study: Journal of Petrology, v. 24, n. 1, p. 1–25, https://doi.org/10.1093/petrology/24.1.1
Stern, R. J., 2004, Subduction initiation: Spontaneous and induced: Earth and Planetary Science Letters, v. 226, n. 3–4, p. 275–292, https://doi.org/10.1016/S0012-821X(04)00498-4
Stern, R. J., and Bloomer, S. H., 1992, Subduction zone infancy: Examples from the Eocene Izu-Bonin-Mariana and Jurassic California arcs: Geological Society of America Bulletin, v. 104, n. 12, p. 1621–1636, https://doi.org/10.1130/0016-7606(1992)104<1621:SZIEFT>2.3.CO;2
Stratford, W. R., and Stern, T. A., 2004, Strong seismic reflections and melts in the mantle of a continental back-arc basin: Geophysical Research Letters, v. 31, n. 6, https://doi.org/10.1029/2003GL019232
Sun, S. S., and McDonough, W. F., 1989, Chemical and isotopic systematics of oceanic basalts: Implications for mantle composition and processes: Geological Society, London, Special Publications, v. 42, p. 313–345, https://doi.org/10.1144/GSL.SP.1989.042.01.19
Swinden, H. S., 1996, The application of volcanic geochemistry to the metallogeny of volcanic-hosted sulphide deposits in central Newfoundland: Geological Association of Canada, Short Course Notes 12, p. 329–358.
Swinden, H. S., Jenner, G. A., Kean, B. F., and Evans, D. T. W., 1989, Volcanic rock geochemistry as a guide for massive sulphide exploration in central Newfoundland: Newfoundland and Labrador Department of Natural Resources, Geological Survey, Report 89-1, p. 201–219.

Swinden, H. S., Jenner, G. A., Fryer, B. J., Hertogen, J., and Roddick, J. C., 1990, Petrogenesis and paleotectonic history of the Wild Bight Group, an Ordovician rifted island arc in central Newfoundland: Contributions to Mineralogy and Petrology, v. 105, n. 2, p. 219–241, https://doi.org/10.1007/BF00678987

Swinden, H. S., Jenner, G. A., and Szybinski, Z. A., 1997, Magmatic and tectonic evolution of the Cambrian-Ordovician Laurentian margin of Iapetus: Geochemical and isotopic constraints from the Notre Dame Subzone, Newfoundland: Geological Society of America, Memoirs, v. 191, p. 337–365, https://doi.org/10.1130/0-8137-1191-6.337

Szybinski, Z. A., ms, 1995, Paleotectonic and structural setting of the western Notre Dame Bay area, Newfoundland Appalachians: St. John's, Newfoundland, Canada, Memorial University of Newfoundland, Ph. D. thesis, 690 p.

Tanaka, T., Togashi, S., Kamioka, H., Amakawa, H., Kagami, H., Hamamoto, T., Yuhara, M., Orihashi, Y., Yoneda, S., Shimizu, H., Kunimaru, T., Takahashi, K., Yanagi, T., Nakano, T., Fujimaki, H., Shinjo, R., Asahara, Y., Tanimizu, M., and Dragusanu, C., 2000, JNdi-1: A neodymium isotopic reference in consistency with LaJolla neodymium: Chemical Geology, v. 168, n. 3–4, p. 279–281, https://doi.org/10.1016/S0009-2541(00)00198-4

Tatsumi, Y., 1989, Migration of fluid phases and genesis of basalt magmas in subduction zones: Journal of Geophysical Research-Solid Earth, v. 94, n. B4, p. 4697–4707, https://doi.org/10.1029/JB094iB04p04697

——— 2006, High-Mg andesites in the Setouchi volcanic belt, southwestern Japan: Analogy to Archean magmatism and continental crust formation?: Annual Review of Earth and Planetary Sciences, v. 34, p. 467–499, https://doi.org/10.1146/annurev.earth.34.031405.125014

Taylor, S. R., and McLennan, S. M., 1985, The continental crust: Its composition and evolution: Oxford, England, Blackwell Scientific Publications, 312 p.

Tremblay, A., Maisonneuve, S., and Lacroix, S., 1996, Contexte lithologique et structural des gîtes de Duvan et de DuReine, région de La Sarre, Abitibi, Québec: Géologie Québec Report MB 96-36, 66 p.

Tsuchiya, N., and Kanisawa, S., 1994, Early Cretaceous Sr-rich silicic magmatism by slab melting in the Kitakami Mountains, Northeast Japan: Journal of Geophysical Research-Solid Earth, v. 99, n. B11, p. 22205–22220, https://doi.org/10.1029/94JB00458

Tuach, J., and Kennedy, M. J., 1978, The geologic setting of the Ming and other sulfide deposits, consolidated Rambler mines, Northeast Newfoundland: Economic Geology, v. 73, n. 2, p. 192–206, https://doi.org/10.2113/gsecongeo.73.2.192

Urabe, T., 1987, The effect of pressure on the partitioning ratios of lead and zinc between vapor and rhyolite melts: Economic Geology, v. 82, n. 4, p. 1049–1052, https://doi.org/10.2113/gsecongeo.82.4.1049

Urabe, T., Scott, S. D., and Hattori, K., 1983, A comparison of footwall-rock alteration and geothermal systems beneath some Japanese and Canadian volcanogenic massive sulfide deposits: Economic Geology Monograph 5, p. 345–364, https://doi.org/10.5382/Mono.05.21

Urabe, T., Baker, E. T., Ishibashi, J., Feely, R. A., Marumo, K., Massoth, G. J., Maruyama, A., Shitashima, K., Okamura, K., Lupton, J. E., Sonoda, A., Yamazaki, T., Aoki, M., Gendron, J., Greene, R., Kaiho, Y., Kisimoto, K., Lebon, G., Matsumoto, T., Nakamura, K., Nishizawa, A., Okano, O., Paradis, G., Roe, K., Shibata, T., Tennant, D., Vance, T., Walker, S. L., Yabuki, T., and Ytow, N., 1995, The effect of magmatic activity on hydrothermal venting along the superfast-spreading East Pacific Rise: Science, v. 269, n. 5227, p. 1092–1095, https://doi.org/10.1126/science.269.5227.1092

van Staal, C. R., 2007, Pre-Carboniferous tectonic evolution and metallogeny of the Canadian Appalachians, *in* Goodfellow, W. D., editor, Mineral deposits of Canada: A synthesis of major deposit-types, district metallogeny, the evolution of geological provinces, and exploration methods: Geological Association of Canada, Mineral Deposits Division, Special Publication n. 5, p. 793–818.

van Staal, C. R., and Barr, S. M., 2012, Lithospheric architecture and tectonic evolution of the Canadian Appalachians, *in* Percival, J. A., Cook, F. A., and Clowes, R. M., editors, Tectonic Styles in Canada Revisited: The LITHOPROBE perspective: Geological Association of Canada Special Paper 49, p. 41–95.

van Staal, C. R., Dewey, J. F., Mac Niocaill, C., and McKerrow, W. S., 1998, The Cambrian-Silurian tectonic evolution of the Northern Appalachians and British Caledonides: History of a complex, west and southwest Pacific-type segment of Iapetus: Geological Society Special Publications, v. 143, p. 199–242, https://doi.org/10.1144/GSL.SP.1998.143.01.17

van Staal, C. R., Whalen, J. B., McNicoll, V. J., Pehrsson, S., Lissenberg, C. J., Zagorevski, A., van Breemen, O., and Jenner, G. A., 2007, The Notre Dame Arc and the Taconic Orogeny in Newfoundland: Geological Society of America Memoir 200, p. 511–552, https://doi.org/10.1130/2007.1200(26)

van Staal, C. R., Whalen, J. B., Valverde-Vaquero, P., Zagorevski, A., and Rogers, N., 2009, Pre-Carboniferous, episodic accretion-related, orogenesis along the Laurentian margin of the Northern Appalachians: Geological Society, London, Special Publications, v. 327, p. 271–316, https://doi.org/10.1144/SP327.13

van Staal, C. R., Chew, D. M., Zagorevski, A., McNicoll, V., Hibbard, J., Skulski, T., Escayola, M. P., Castonguay, S., and Sylvester, P. J., 2013, Evidence of Late Ediacaran hyperextension of the Laurentian Iapetan margin in the Birchy Complex, Baie Verte Peninsula, northwest Newfoundland: Implications for the opening of Iapetus, formation of peri-Laurentian microcontinents and Taconic-Grampian orogenesis: Geoscience Canada, v. 40, n. 2, p. 94–117, https://doi.org/10.12789/geocanj.2013.40.006

Waldron, J. W. F., and van Staal, C. R., 2001, Taconian Orogeny and the accretion of the Dashwoods Block: A peri-Laurentian microcontinent in the Iapetus Ocean: Geology, v. 29, n. 9, p. 811–814, https://doi.org/10.1130/0091-7613(2001)029<0811:TOATAO>2.0.CO;2

Watson, E. B., and Harrison, T. M., 1983, Zircon saturation revisited: Temperature and composition effects in a variety of crustal magma types: Earth and Planetary Science Letters, v. 64, n. 2, p. 295–304, https://doi.org/10.1016/0012-821X(83)90211-X

Weis, D., Kieffer, B., Maerschalk, C., Pretorius, W., and Barling, J., 2005, High-precision Pb-Sr-Nd-Hf isotopic

characterization of USGS BHVO-1 and BHVO-2 reference materials: Geochemistry, Geophysics, Geosystems, v. 6, n. 2, 10 p., https://doi.org/10.1029/2004GC000852

Wilson, M., 1989, Igenous petrogenesis: A global tectonic approach: Amsterdam, Springer, 466 p.

Winchester, J. A., and Floyd, P. A., 1977, Geochemical discrimination of different magma series and their differentiation products using immobile elements: Chemical Geology, v. 20, p. 325–343, https://doi.org/10.1016/0009-2541(77)90057-2

Wood, D. A., 1980, The application of a Th-Hf-Ta diagram to problems of tectonomagmatic classification and to establishing the nature of crustal contamination of basaltic lavas of the British Tertiary volcanic province: Earth and Planetary Science Letters, v. 50, n. 1, p. 11–30, https://doi.org/10.1016/0012-821X(80)90116-8

Wyllie, P. J., and Wolf, M. B., 1993, Amphibolite dehydration-melting: Sorting out the solidus: Geological Society, Longon, Special Publications, v. 76, p. 405–416, https://doi.org/10.1144/GSL.SP.1993.076.01.20

Yang, K., and Scott, S. D., 1996, Possible contribution of a metal-rich magmatic fluid to a sea-floor hydrothermal system: Nature, v. 383, p. 420–423, https://doi.org/10.1038/383420a0

——— 2002, Magmatic degassing of volatiles and ore metals into a hydrothermal system on the modern sea floor of the eastern Manus back-arc basin, western Pacific: Economic Geology, v. 97, n. 5, p. 1079–1100, https://doi.org/10.2113/gsecongeo.97.5.1079

——— 2003, Geochemical relationships of felsic magmas to ore metals in massive sulfide deposits of the Bathurst mining camp, Iberian pyrite belt, Hokuroku District, and the Abitibi Belt: Economic Geology Monograph 11, p. 457–478, https://doi.org/10.5382/Mono.11.20

Zagorevski, A., and van Staal, C. R., 2011, The record of Ordovician arc-arc and arc-continent collisions in the Canadian Appalachians during the closure of Iapetus, *in* Brown, D., and Ryan, P. D., editors, Arc-Continent Collision: Frontiers in Earth Sciences, p. 341–371, https://doi.org/10.1007/978-3-540-88558-0_12